

AD-A284 146

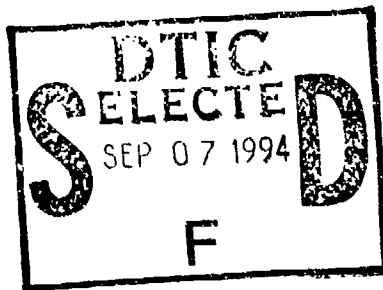


6469-EE-01

①

LIGHT SCATTERING FROM ROUGH SURFACES

Principal Investigator: J C Dainty
Contractor: Imperial College
Contract Number: DAJA45-90-C-0026



APPENDIX

of

FINAL REPORT

Draft Copy of PhD Thesis

Angular Correlation of Speckle Patterns

R W Syrratt

This document has been approved
for public release and sale; its
distribution is unlimited.

201/85
176350 94-29151

DTIC QUALITY INSPECTED 3

UNIVERSITY OF LONDON
Imperial College of Science, Technology and Medicine
Blackett Laboratory
Applied Optics

Angular Correlation of Speckle Patterns

Richard William Syrett
June 1994

Accession For	
PTIS	CRA&I <input checked="" type="checkbox"/>
DIC	TAB <input type="checkbox"/>
Unannounced <input type="checkbox"/>	
Justification	
By <i>form 50</i>	
Distribution	
Availability	
Dist	Availability
<i>A-1</i>	

Thesis submitted in partial fulfilment of the
requirements for the Degree
Doctor of Philosophy
and for the
Diploma of Imperial College

DISCUSSION PAPER 3

94 9 00 107

To Jacqueline

Acknowledgements

First of all I should like to thank my supervisor Prof. Chris Dainty for the support and encouragement he gave throughout my time in the Applied Optics group (when I could actually find him) and for having faith in my more adventurous beliefs.

I should also like to thank Richard Lane for letting me slowly into the realms of statistics. If it was not for his patience I would have had to resort to books at a much earlier stage.

For his demonstrations of the various experimental techniques, I owe thanks to Andrew Sant. Also, on behalf of all students writing (and written) up since then, thank you very much for setting such a high standard in the quality of diagrams expected from us.

nik Wooder is deserving of thanks for his efforts to keep the ever expanding Sun network under control — and for letting me take liberties with it. Also (for helping me take those liberties) thanks go to Mark, Colin, Neil, John, Tom, Ian and Liam. Liam, you won't get *any* work done once you see Empire... In a similar vein, I would like to thank Simon Gornall for all those e-conversations we had.

Thanks go to my parents for everything they have contributed through my student years. You won't be the only Dr. Syrratt for much longer Dad...

Finally, I would like to state my appreciation of everything done for me by my fiancée Jacquie, especially over the last few months; those cups of tea and the meals, not to mention the sundry other ways in which she makes life easier, all helped to keep me seated in front of this keyboard.

Abstract

This work examines the angular correlation of speckle patterns produced by the coherent illumination of random rough surfaces. Speckle patterns are produced when coherent light is scattered by a rough surface or other random medium. As the angle of illumination changes, the speckle pattern changes at a rate determined by geometry and by the details of the scattering process. It is this angular change that is studied in this thesis by means of the correlation coefficient.

Experimental studies are made of the angular change of speckle patterns from low and high sloped Gaussian random rough surfaces. They are illuminated with a linearly polarised laser beam, and the correlation coefficient of speckle patterns observed with a CCD camera then being determined by computational analysis.

The Kirchhoff approximation is applied to the Helmholtz-Kirchhoff integral to obtain a two-dimensional analytical solution for the correlation produced by a low slope, single scattering, Gaussian surface. The results are compared with the experimental measurements.

A simple statistical examination of Gaussian random rough surfaces is made; this shows that the Kirchhoff approximation is still valid even for surfaces which exhibit multiple scattering. The Kirchhoff approximation is used to derive an expression for the scattered light from a high sloped, multiply scattering, surface. This required computational implementation — an advantage being that surface shading can be accounted for. A very fast computational method for determining shaded areas on a surface is presented. Polarisation changes in the scattered light are catered for.

A conceptual model of the processes involved in multiple scattering is developed, successfully explaining various features of observed results.

Contents

1	Introduction	27
1.1	Introduction and Literature Review	27
1.1.1	Theoretical Models	28
1.1.2	Mean Scattered Intensity	32
1.1.3	Correlation Studies	36
1.2	Synopsis	38
1.3	Statement of Originality	40
1.4	Correlation Geometry	40
2	Mathematical Concepts	43
2.1	Statistics	43
2.1.1	Probability	43
2.1.2	Random Variables	45

2.1.3	Random Processes	50
2.1.4	Differentiation of a Random Process	53
2.2	Gaussian Random Rough Surfaces	53
2.3	Convolution	55
2.3.1	Convolution Theorem	56
2.3.2	Extension of the Convolution Theorem to Correlation Coefficients	56
2.4	Electromagnetism	57
2.4.1	The Helmholtz-Kirchhoff Integral	57
2.4.2	Polarisation	60
2.4.3	Reflection Coefficients	61
2.4.4	The Kirchhoff Approximation	62
3	Experimental Procedures	67
3.1	Random Rough Surfaces	67
3.1.1	Surface Manufacture	67
3.1.2	Gold Coating	74
3.1.3	Surface Characterisation	74

3.1.4	The Surfaces Studied	80
3.2	Obtaining the Angular Correlations	82
3.2.1	Experimental Equipment	82
3.2.2	The Speckle Patterns	86
3.2.3	Processing the Speckle Images	90
3.2.4	Enhancements	94
4	Single Scatter Analytical Study	99
4.1	The Single Scatter Approximation	99
4.1.1	Derivation	99
4.1.2	Validity of the Single Scatter Model	103
4.2	Correlation Coefficient of Two Speckle Patterns	106
4.2.1	Consequences of the Intensity Correlation	110
4.2.2	Comparison with Experimental Results	115
4.3	Results	122
5	Double Scatter Simulation	131
5.1	Theory	131

5.1.1	The Single Scatter Contribution	132
5.1.2	The Double Scatter Contribution	132
5.1.3	Including Polarisation	136
5.2	Implementation	140
5.2.1	Discretisation for Computer Modeling	141
5.2.2	Calculating Shaded Areas	148
5.2.3	Numerical Random Surfaces	155
5.3	Results	156
5.3.1	Single Scatter Component of Simulation	156
5.3.2	Experimental Results from a Multiply Scattering Surface . . .	159
5.3.3	Computational Results	166
6	Discussion and Conclusion	171
6.1	Single Scatter	171
6.2	Double Scatter	172
6.2.1	Scattered Intensity Envelope Considerations	172
6.2.2	Correlation Considerations	179

6.2.3	Further Analysis of the Simple Model	181
6.3	Concluding Remarks	188

List of Figures

1.1	The geometry to be used to obtain the experimental and theoretical results. Observation is always around the specular direction.	41
2.1	Integration over a surface for a function with a singularity at point P.	59
2.2	Polarisation state definitions.	60
2.3	The geometry used for defining the Fresnel reflection coefficients. . .	62
2.4	The tangent to a surface feature with (a) large and (b) small radius of curvature compared with the illuminating wavelength.	63
3.1	The probability density distribution of the intensity of the superposition of N uncorrelated speckle patterns, each with mean $\eta = 1$, for various N	71
3.2	Arrangement for exposure of photoresist coated plates during surface creation.	72
3.3	Fresnel reflection coefficients for gold at $\lambda = 0.633\mu m$ over a range of angles.	75

3.4	Histogram of the surface heights over a single scan of a surface (surface #80 — see later), a Gaussian curve with the same variance is also shown.	77
3.5	The correlation function of a surface scan, a fitted Gaussian correlation function has a correlation length of $19.54\mu m$	78
3.6	Finite stylus tip size prevents accurate tracing of surface features of a similar size. The scale has been exaggerated, generally the effect is much less noticeable.	79
3.7	Surfaces #80, #239 and #83 plotted on the Kirchhoff validity graph for a wavelength of $\lambda = 0.633\mu m$. The large black areas represent the errors in the measurements of the surfaces.	81
3.8	Schematic diagram of the rig used to control incidence and viewing angles.	83
3.9	The actual arrangement used to mount the camera. The camera is still looking in the specular direction of scattering from the surface. .	84
3.10	Histogram of the intensity values of a speckle pattern formed by surface #80 at ten degrees incidence and observation in the specular direction. Incident and detected light are both s-polarised. The same data plotted on a log scale is inset.	86

3.11	Histogram of the intensity values of a speckle pattern formed by surface #83 at fifty degrees incidence and observation in the specular direction. Incident light is p-polarised and the observed pattern is s-polarised. The same data plotted on a log scale is inset.	87
3.12	Histogram of the intensity values of a speckle pattern formed by surface #239 at thirty degrees incidence and observation in the specular direction. One data set has incident light s-polarised and observed p-polarised, the other has incident light p-polarised and observed s-polarised.	88
3.13	Obtaining the correlation coefficient of two speckle patterns. The cross-correlation of two normalised, zero mean speckle patterns giving the correlation map.	92
3.15	Graph showing the improvement in correlation values obtained at a given angle by masking a surface to reduce pattern shrinking. The solid line is the result from the surface masked, the dashed one unmasked. Note that the vertical distance between points shows a large enhancement.	96
4.1	Geometry for single scatter component of scattered field.	100
4.2	The general scattering geometry showing θ_1 , θ_2 and θ_3	102
4.3	The condition required before double scattering is evident.	104

4.4	Surface parameters for which the single scatter Kirchhoff approximation (Beckmann solution) is valid. Boundaries are placed at the three standard deviation threshold. The surfaces are plotted with the wavelength at $\lambda = 0.633\mu m$ and for normal incidence. Surface #80 (not shown) lies well within the region in which the Beckmann solution applies.	105
4.9	Diagram showing the relationship between a point on the CCD array and the angles θ_1, θ_2 and θ_3 . Note that the centre of the CCD array subtends an angle of θ_1 to the mean surface normal.	117
4.17	Averaged intensity plot for surface #80 with observation in the specular direction. The illuminating light has wavelength $0.633\mu m$ and it and the detected light are s-polarised.	124
4.20	Experimental intensity correlations for surface #239 with incident light s-polarised and detected light p-polarised. Curve labels represent the (incident) angle at which the reference was taken. Observation is in the specular direction and $\lambda = 0.633\mu m$	127
4.21	Experimental intensity correlations for surface #239 with incident light p-polarised and detected light s-polarised. Curve labels represent the (incident) angle at which the reference was taken. Observation is in the specular direction and $\lambda = 0.633\mu m$	128

4.22	Averaged intensity plot for surface #239 with observation in the specular direction. The illuminating light has wavelength $0.633\mu m$ and it and the detected light are s-polarised.	128
4.23	Averaged intensity plot for surface #239 with observation in the specular direction. The illuminating light has wavelength $0.633\mu m$ and is s-polarised. The detected light is p-polarised.	129
5.1	Geometry for the double scatter component of the scattered field. . .	133
5.2	Geometry for polarisation showing the orientation of the electric field coordinate systems within the world frame.	137
5.3	Relative orientation of the electric field coordinate systems with respect to the local scattering plane.	138
5.4	Detail of the relationship between the electric field coordinate system and the local scattering plane.	139
5.5	Numerical integration performed by taking the mid-point of two realisations of a function and multiplying it by their separation. . . .	142
5.6	The distribution of the phase differences between two points binned 50 times over the wavelength, on a 100×100 wavelength surface consisting of 2048 points, with parameters $\sigma = 1.42\lambda$ and $\tau = 4.31\lambda$, over an ensemble average of 100 surfaces. Point to point shading has been taken into account.	144
5.7	A discretised two-dimensional surface — each facet is a flat plane. .	145

5.8	Geometry for calculating the positions of surface facets.	146
5.9	Geometry for calculation of area between two vectors.	148
5.10	Shaded regions of a one-dimensional surface due to columnated incident light.	149
5.11	Shaded regions of a one-dimensional surface due to point to point scattering.	151
5.12	Creation of a template for determining point to point shadows on a two-dimensional surface.	152
5.13	Representations of a computationally generated surface profile showing the results of the shading techniques. The surface height at a point is given by the brightness (light is high). The black regions indicate shaded areas.	154
5.14	Convolution of Gaussian white noise with a Gaussian correlation function. The method is equally valid for two-dimensional surface creation.	156
5.15	Analytical and single scatter computational intensity correlations for observation in the specular direction with the reference at 8 degrees. $\sigma = 2.27\mu m$, $\tau = 20.7\mu m$ and $\lambda = 0.633\mu m$. Both curves have data points every half degree.	157

5.16	Single scatter intensity correlations with polarisation for observation in the specular direction with the reference at 8 degrees. The intensity of the p-polarised component was about 10^4 times smaller than the s-polarised one. $\sigma = 2.27\mu m$, $\tau = 20.7\mu m$ and $\lambda = 0.633\mu m$	158
5.17	Experimental intensity correlations for surface #83 with incident and detected light s-polarised. Curve labels represent the (incident) angle at which the reference was taken. Observation is in the specular direction and $\lambda = 0.633\mu m$	160
5.18	Experimental intensity correlations for surface #83 with incident and detected light p-polarised. Curve labels represent the (incident) angle at which the reference was taken. Observation is in the specular direction and $\lambda = 0.633\mu m$	160
5.20	Experimental intensity correlations for surface #83 with incident light s-polarised and detected light p-polarised. Curve labels represent the (incident) angle at which the reference was taken. Observation is in the specular direction and $\lambda = 0.633\mu m$	162
5.21	Experimental intensity correlations for surface #83 with incident light p-polarised and detected light s-polarised. Curve labels represent the (incident) angle at which the reference was taken. Observation is in the specular direction and $\lambda = 0.633\mu m$	163
5.22	Surface plot of correlation coefficients for surface #83 with incident light s-polarised and observed speckle patterns p-polarised.	164

5.23	Average intensity plot for surface #83 with observation in the specular direction and with s-polarised (squares) and p-polarised light (circles) detected. The illuminating wavelength is $0.633\mu m$ and s-polarised.	165
5.25	Computational correlation curves, for a surface with parameters identical to surface #83, with the reference image at 10 degrees and showing the different components. The incident field has a wavelength of $0.633\mu m$ and is s-polarised. The ensemble average was taken over 800 frames of a 2048 point surface with a side length of 60λ	167
5.27	Total (single + double) computational correlation curves for surface #83 for various reference images (at 10, 20, 30 and 40 degrees). The incident field has a wavelength of $0.633\mu m$ and is s-polarised. The correlations consider only the s-polarised scattered component. The ensemble average was taken over 600 frames of a 2048 point surface with a side length of 60λ	169
5.28	Total (single + double) computational correlation curves for surface #83 for various reference images (at 10, 20, 30 and 40 degrees). The incident field has a wavelength of $0.633\mu m$ and is s-polarised. The correlations consider only the p-polarised scattered component. The ensemble average was taken over 600 frames of a 2048 point surface with a side length of 60λ	170
6.1	A pair of the many possible interfering paths within a valley of a rough surface.	173

6.3	Intensity plots for s-polarised and p-polarised light detected from surface #83, showing the angles of the peaks observed for observation in the specular direction when s-polarised light is incident with wavelength $0.633\mu m$. Data points were taken every half degree.	177
6.4	Schematic diagram showing how a well in a surface doubly scatters polarised light to give both a co-polarised and cross-polarised component.	178
6.5	A pair of the many possible interfering paths within a valley of a rough surface shown at different angles of incidence.	180
6.6	Diagram showing how an increase in the angle of incidence leads to a decrease in the distance traversed across the well.	183

List of Tables

3.1 Rms height and correlation length for the surfaces to be studied. . .	81
---	----

Chapter 1

Introduction

1.1 Introduction and Literature Review

Interest in light scattering from random media has undergone a noticeable revival within the last decade. Although some of this renewed interest may be attributable to the more recent computer technology, enabling solutions to various scattering problems to be determined numerically, the subject has generated interest in the medical field. In this area the volume scattering and absorption properties of a patient may potentially give information about internal processes without the necessity of large and expensive equipment or the use of harmful radiation.

The driving forces behind the study of scattering from random rough surfaces are its potential as a non-destructive or remote probe for measuring the statistical properties of rough surfaces, and the inescapable effect that the inherent randomness in all surfaces has on everyday scattering applications. Radar falls into this last category, and may be regarded as a scaled up light scattering problem; similar results may be obtained using light in a laboratory as would be gathered from a more expensive,

less controllable, radar set up.

1.1.1 Theoretical Models

This section will present some of the theoretical models which exist for determining the problem of light scattering from random rough surfaces. It aims to give an introduction to some of the methods not used within this work.

Approximate theories exist for very small height deviations across the surface (such as perturbation theory) and for surfaces which have sufficiently low gradients such that they may be considered as single scattering (Beckmann theory or single scatter/first order Kirchhoff approximation). Other methods attempt to predict the effects of multiple scattering and include the effects of surface shadowing. Computational methods of solving the integral equations also exist which avoid the necessity of approximations. Most of the theories discussed below may be found in more depth in the book by Ogilvy^[1].

Perturbation Theory

Perturbation theory can be used for slightly rough surfaces which deviate from a flat plane by only a small amount.

The field on a surface $z = h(x, y)$ may be written as

$$E = E_i + E_s \quad (1.1)$$

where the subscripts i and s represent the incident and scattered fields respectively. E is a vector quantity of a particular polarisation.

The perturbation theory assumes that the scattered field may be written as a series:

$$E_s = E_{s0} + E_{s1} + E_{s2} + \cdots \quad (1.2)$$

where the numerals represent the different orders.

Assuming E_i and E_s to be functions of h , taking a Taylor expansion in terms of h , terms of the same order in h may be equated after applying the Dirichlet boundary condition, namely that the field at the surface is zero

$$E|_{z=h} = 0 \quad (1.3)$$

at the mean plane ($z = 0$). Applying the Dirichlet boundary condition when the surface heights are much smaller than a wavelength, the zeroth order term in the perturbation series (the field scattered from a flat plane) is found:

$$E_{s0}|_{z=0} = -E_i|_{z=0} \quad (1.4)$$

and the first order perturbation term (representing the effects of the deviations in the surface from a smooth plane) is

$$E_{s1}|_{z=0} = -h \left(\frac{\partial E_i}{\partial z} \Big|_{z=0} + \frac{\partial E_{s0}}{\partial z} \Big|_{z=0} \right) \quad (1.5)$$

The Helmholtz-Kirchhoff integral (discussed in chapter two):

$$E_s = - \int_S \frac{\partial E}{\partial n} \psi dS \quad (1.6)$$

may now be used, with equation (1.5) as a boundary condition, to give the scattered field:

$$E_{s1} = \int_S h \left(\frac{\partial E_i}{\partial z} + \frac{\partial E_{s0}}{\partial z} \right) \frac{\partial \psi}{\partial z} dS \quad (1.7)$$

where S is the mean surface plane and ψ is the half space Green's function; all other notation is as previously defined.

A similar method may be used to obtain the result for the Neumann boundary condition,

$$\frac{\partial E}{\partial \mathbf{n}}|_{z=0} = 0 \quad (1.8)$$

This may be used when the surface gradients are much less than one, and gives

$$E_{e1} = \int_S \left[\frac{\partial h}{\partial x} \left(\frac{\partial E_i}{\partial x} + \frac{\partial E_{s0}}{\partial x} \right) + \frac{\partial h}{\partial y} \left(\frac{\partial E_i}{\partial y} + \frac{\partial E_{s0}}{\partial y} \right) - h \left(\frac{\partial^2 E_i}{\partial z^2} + \frac{\partial^2 E_{s0}}{\partial z^2} \right) \right] \psi dS \quad (1.9)$$

It is possible, again with a similar method, to obtain the second order perturbation of the scattered field. The original Taylor expansion must be taken out to second order (terms in h^2) to obtain the new boundary condition to apply to the Helmholtz-Kirchhoff integral.

The accuracy of perturbation theory has been studied by many authors (cf. section 3.1.3 of reference [1] for a detailed review), the generally accepted range of validity being $k\sigma \ll 1$ where σ is the rms height of the surface, τ the correlation length and k the wavenumber $\frac{2\pi}{\lambda}$. One recent work compares perturbative calculations with "exact numerical results" (as used in references [2], [3] and [4]) and those obtained by using the Kirchhoff approximation^[5]. It finds that for $k\tau > 1$ (where τ is the correlation length of the surface), the fourth order perturbative expansion is better than the second order one, the latter being accurate when the total incoherently scattered energy is less than about 9% of the incident energy. For the fourth order expansion, the theory was found to be accurate when the total incoherently scattered energy is less than around 39% of the incident energy. If $k\tau < 1$, it was found that

the perturbative series is not convergent, and the second order expansion gives better results than the fourth.

Surfaces considered in this thesis have an rms roughness, $k\sigma \gg 1$, hence the perturbation approximation will be of little value.

Extinction Theorem

The extinction theorem derives its name from the use of the condition that the field within a scattering surface must cancel the incident field. For finite surfaces, this condition is approximated to include all space below the surface plane. It is also known as the null-field method and the extended boundary condition method.

Starting with the usual Helmholtz-Kirchhoff integral (equation (1.6)) for the scattered field, and writing the incident field such that the field below the surface is zero -- i.e. the incident field cancels out the scattered field ($E_i + E_s = 0$), then

$$E_i = \int_S \frac{\partial E}{\partial \mathbf{n}} \psi dS \quad (1.10)$$

Equation (1.10) may be solved for E , which may then be substituted into equation (1.6) to give the scattered field. In practice it is usually necessary to find an approximate solution to equation (1.10), by using an expansion similar to that used in perturbation techniques. Numerical simulation avoids this necessity by using an iterative technique to obtain an exact result^{[3][5][4]}.

Whilst the extinction theorem provides an exact solution in principle, the scattered intensity cannot be written as a single closed form expansion, and therefore it is of little value in providing support for a physical picture of light scattering.

Kirchhoff Theory

Kirchhoff theory is used extensively in later chapters of this thesis and will not be dealt with in this section. The single scattering Beckmann theory is discussed in chapter four, and the double scattering technique used by Bruce^{[6][7][8]} and others^{[9][10][11]} is explained in chapter five.

One technique increasingly used starts with the extinction theorem and, by iterating the surface field derived n times, gives increasing terms in a series of which the $n = 0$ term is the single scatter Kirchhoff solution, larger n giving terms representing double and higher order scattering terms^{[12][13]}. Computational techniques must be used to solve a large matrix equation.

1.1.2 Mean Scattered Intensity

Research into light scattering from random rough surfaces has remained fairly active since the reporting by Mendez and O'Donnell^{[14][15]} of 'enhanced backscatter'. This work was stimulated by the observation of a similar effect in volume scattering^[16]. The effect itself has been known of for years in the astronomical field, referred to as the 'opposition effect' [Montgomery^[17] and refs. therein]. The name came from the fact that it was noticed in scattering from visible bodies in the solar system when they and the sun were in opposition, i.e., on opposite sides of the earth. The significance of Mendez and O'Donnell's work was that well characterised random rough surfaces were used, following the method of Gray^[18] (see chapter three), enabling confident comparisons with computational results and the existing approximate analytical theories.

It was found that Beckmann theory^[19] agreed well with experimental results from a low slope surface for small angles of incidence. A study of two steeper slope surfaces was undertaken, showing the enhanced backscatter phenomenon, and a possible explanation for the backscattering process was outlined — the enhancement being due to constructive interference of equal and opposite multiply scattering paths.

Experiments have been conducted comparing low sloped surfaces to theory^[20] and various others examine the scattering characteristics of known steep slope surfaces which display the enhanced backscattering phenomenon. Included in these is a comparison of dielectric and perfectly conducting (gold) surfaces with identical profiles^[21] — epoxy resin copies of the originally fabricated gold coated surface were made via a silicone gel mould. A gold coated reproduction was compared experimentally with the master and the results confirm that the technique faithfully copies the original. Significant enhanced backscattering (noticed in the gold surface) was not observed experimentally in the dielectric case. Results of a numerical calculation were compared with the experimental dielectric scattering results showing broad agreement.

Results from various one- and two-dimensional surfaces have also been presented for different wavelengths of illumination^[22] and a comparison of results from statistically similar one- and two-dimensional surfaces has been made^[23] showing results which are similar in as far as they may be compared.

In reference [23] the Stokes' parameters of the average scattered light are utilised to present experimental data of the polarised and unpolarised components. The backscatter peak was found only in the unpolarised component, and is therefore believed to be a product of multiple scattering. Numerical calculation results were

compared favourably with experimental results from one-dimensional surfaces.

More extensive studies have since been made of the polarisations of scattered fields and the Stokes' parameters. Four unique elements were found in the Mueller matrix of a one-dimensional surface, all of which were shown to be significant in scattering from such a surface which produces enhanced backscattering [24]. The complete Mueller matrix for a one dimensional perfectly conducting random rough surface has been numerically and experimentally found^[13] for all observed angles and for a number of different angles of incidence — the results were generally similar to each other.

A complete Mueller matrix has been numerically and experimentally calculated for a gold and dielectric one dimensional surface^[8]. Agreement between numerical and experimental results was good for the dielectric case, but differed slightly in the case of the gold surface. The difference was shown to be in the m_{34} matrix term (mapping linearly polarised incident light to circularly polarised scattered light), and believed to be due to a difference in the reflection coefficients of the surface and those used in the calculation. The Stokes' parameters are examined and utilised as in reference [23] to show the polarised and unpolarised scattering components.

A presentation was given of numerical calculation results of the angular contribution in the intensity of the diffuse component of p-polarised light scattered from a random grating ruled on penetrable and impenetrable dielectric media^[4]. It is found that a metallic (silver) surface gives similar results to a perfectly conducting one. This result has a large impact on the numerical study of light scattering as it is much simpler to implement a perfectly conducting surface than a metallic one.

Multiple scattering and shadowing extensions to the simple Kirchhoff theory have been implemented^{[6][7][8]} (see chapter five) — numerical results for single and double scatter components of the Kirchhoff theory are presented, for gold and dielectric one dimensional surfaces, and compared favourably with experiment. Experimental results have also been compared to the double scatter Kirchhoff theory for a gold and a dielectric surface which have identical height profiles ^[25]. Various wavelengths were used. Generally, the double scatter Kirchhoff theory was found to be in good agreement with experimental results for angles of incidence of less than sixty degrees.

The 'exact' method of the iterative solution of the extinction theorem^[3] has been used in a Monte-Carlo numerical calculation^[2] in conjunction with the single scatter Kirchhoff theory for a range of surface statistics, to define the limits of the single scatter Kirchhoff approximation. The results presented do not define the limits of where the Kirchhoff approximation can be applied, but where the single scattering theory based upon the approximation can be expected to succeed.

Other work outside the scope of correlation measurements, but not so closely related to the work to be presented in the following chapters, includes joint experimental and theoretical studies of the backscattering from and transmission through dielectric and thin film random rough surfaces^{[26][27]}. Speckle techniques have also been developed^[28] — speckle contrast measurements^{[29][30]} are amongst the many different methods discussed.

1.1.3 Correlation Studies

Correlation studies were first carried out in the early to mid-seventies. However, at this time the interest in multiply scattering surfaces had not developed and all works dealt with low slope surfaces.

Pedersen^[31] discussed speckle correlation, giving a theoretical explanation of various results reported prior to his study. Most of his interest, however, lay with polychromatic speckle^[32] and his work is not relevant to this thesis.

The work by Léger and Perrin to determine surface roughness via a correlation technique is directly relevant to this work. By exposing a photographic plate to speckle produced by a rough surface at two angles of incidence, Young's fringes could be observed in the Fourier plane when the processed plate was placed in a converging beam^[33]. The contrast of the fringes was mathematically related to the surface roughness, starting with the general Beckmann solution for the scattered field, but then working in the Fourier domain.

In a later paper^[34] a more general derivation of the fringe contrast from angular correlations was reported. This was again based on the single scattering Beckmann theory, but took a real space approach to the problem. It is the basis of the derivation to follow in chapter four.

More recently, Ohlidal^[35] compared the equivalent of Léger and Perrin's method (which uses the Fraunhofer approximation) to results obtained using the Fresnel approximation. No comparison with experimental measurements was made, but an analysis of when each method should apply is presented.

The most recent studies in this area have been performed by Michel et al. and Knotts et al. Michel et al.^[36] present numerical results for the angular correlations of scattered amplitudes from a one dimensional surface and analyse the results into those attributable to single and double scattering. Knotts et al.^[37] offer experimental results for angular correlations obtained from a one-dimensional surface and compare with numerical results. A discussion as to the cause of various features observable in the results is given.

The Memory Effect

The memory effect was named by Feng et al.^[38] for situations of volume scattering (scattering from a media in which the light may travel, e.g., paint or milk). They show various elements contributing to the correlation function, and show that certain of these are large when the "momentum transfer of the incident beams equals the transmitted ones", i.e., the change in the wave vectors upon scattering is the same in both cases being correlated, $\Delta \mathbf{q}_1 = \Delta \mathbf{q}_2$. $\Delta \mathbf{q}$ is defined as $\mathbf{q}_a - \mathbf{q}_b$, the difference in the (transverse) wave vectors of the incident and scattered light.

Applying this to in plane surface scattering correlations, the memory effect condition holds (see chapter four) when

$$\sin \theta_i - \sin \theta_s = \sin \phi_i - \sin \phi_s \quad (1.11)$$

where the subscripts i and s represent the incident and scattered angles respectively, θ being used to obtain one speckle pattern and ϕ being used to obtain the second.

This condition was used by Léger and Perrin^[34] twelve years earlier in their work

described above, although it was expressed in a different form:

$$\cos \theta_i \delta \theta = \cos \phi_i \delta \phi \quad (1.12)$$

Equation (1.11) may be reconciled to equation (1.12) by noting that θ_s and ϕ_s have been replaced by $\theta_i + \delta \theta$ and $\phi_i + \delta \phi$ respectively and by applying a simple trigonometric transform. As they were only dealing with small changes in $\delta \theta$ and $\delta \phi$, terms of order $\delta \theta^2$ and $\delta \phi^2$ can be removed.

Pedersen^[31] also noted that it was desirable to have the condition satisfied, and equation (1.11) has been used in the work reported by Michel et al.^[36].

Nieto-Vesperinas and Sánchez-Gil^[39] have studied the memory effect in relation to surface scattering, but they also notice an “enhanced long range correlation” observable when

$$\sin \theta_i + \sin \theta_s = \pm (\sin \phi_i + \sin \phi_s) \quad (1.13)$$

The origin of this is believed to be the same as for the peak observed in enhanced backscattering.

1.2 Synopsis

The remaining sections of this chapter consist of a statement of the original work undertaken and a description of the scattering geometry to be used throughout the work.

The second chapter contains general theoretical notions, including statistical concepts such as random variables and processes. It also contains a derivation of

the Helmholtz-Kirchhoff integral and some other concepts from electromagnetism, namely descriptions of reflection coefficients and polarisation.

Chapter three contains all of the experimental methods used; these include manufacturing and classifying random rough surfaces and the procedure used to calculate the correlation coefficient from digitised images of speckle patterns.

An analytical expression for the correlations expected from a low-sloped, single scattering surface is derived from the Helmholtz-Kirchhoff integral, in chapter four, by applying the Kirchhoff approximation to it. Experimental results for such a surface are compared with the theoretical result and discussed.

The fifth chapter extends the Kirchhoff result to include the double scatter term. The equation is no longer analytically soluble and is implemented computationally. Polarisation changes are considered, and an algorithm for rapidly determining 'lines of sight' on a surface is presented. It was necessary to develop this algorithm in order to calculate point-to-point shading in the fastest possible time; without it a two-dimensional computational problem of this nature would not be practical. Results for a high-sloped, multiple scattering surface are compared with the computational results.

The last chapter considers, and attempts to explain, the results obtained. A possible mechanism to describe the observed single and double components of multiply scattering surfaces is presented.

1.3 Statement of Originality

There is not a great deal of original content within chapters one, two and three — these are mainly concerned with introducing some background information and the concepts and techniques available for use within this thesis.

Chapters four and five contain new experimental results for the intensity correlation of speckle patterns produced by a method described in chapter three. In chapter four an existing analytical expression is extended to deal with two-dimensional intensity correlations and then numerically averaged to enable a comparison with the experimental results. In chapter five, a double scatter numerical simulation based on the Kirchhoff approximation is extended to cope with two dimensional surfaces. A new fast technique for calculating the shadows cast on the surface by its own fluctuations is presented.

Chapter six promotes a simple conceptual model which can successfully explain the existence of and to some extent predict the positions of, various features noted in the double scatter correlation results and in double scatter average intensity results.

1.4 Correlation Geometry

Consider a plane mirror which can rotate about an axis which lies in the plane of the mirror. If an observer looks in the direction of the mirror, he will see an image of what is around the specular direction of observation. Now if the mirror is rotated about the axis, and the observer moves around the same axis until he can see the same scene as before, then he will have rotated twice as much as the mirror.

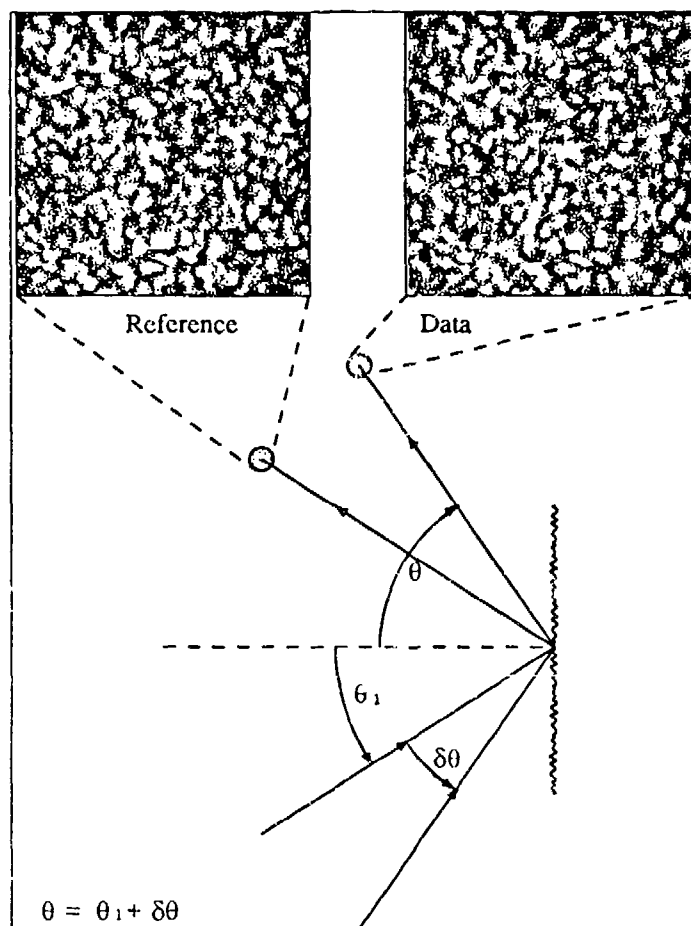


Figure 1.1: The geometry to be used to obtain the experimental and theoretical results. Observation is always around the specular direction.

Extending this arrangement to the correlation of speckle patterns formed by scattering from a random rough surface: if the scattering surface is considered as random fluctuations on top of a plane mirror, the phase variations introduced to the scattered light should be most identical at different incident angles if always observing in the specular direction and illuminating on the rotation axis (such that the same random fluctuations are illuminated). If these conditions are met, only the change in the phase variations due to the different angles at which light is incident on the surface should be observed.

The geometrical arrangement to be used for investigating the angular correlation of speckle patterns will be conducted by always viewing speckle patterns in the specular direction to the incident illumination (see figure 1.1). The argument presented above will be examined mathematically, for the case of a Gaussian random rough surface, later in chapter four.

Chapter 2

Mathematical Concepts

2.1 Statistics

In this section, various statistical notions and formulae, which will be required later, will be presented. Unless otherwise stated, all variables will be real and continuous. The bulk of the material below can be found in textbooks (e.g., Papoulis^[40] or Goodman^[41]).

2.1.1 Probability

Probability may be defined in three ways, but generally all of the definitions are required to form a complete picture, each definition considered in isolation lacking something which would enable it to stand on its own. In fact, the most mathematically rigorous definition of probability (the axiomatic approach) is incapable of assigning a numerical probability to any event other than the certain one, so it, and the reams of theory based upon it, would be useless in the real world without the other, 'dirtier', relative frequency and classical (a priori) approaches.

The definitions of probability are:

- the *axiomatic* definition, which assigns a number to an event, the number restricted to be positive, the probability of the certain event being one, and the probability of two mutually exclusive events being defined as the sum of the two individual probabilities;
- the *relative frequency* definition, which defines probability of an event as the fraction of the number of times the event occurs over the number of experiments performed as the number of experiments performed tends to infinity; and
- the *classical (a priori) definition*, which counts the possible outcomes and defines the probability as the fraction of the number of outcomes in which the event is expected to occur in a single experiment over the total number of possible outcomes.

The most useful single definition of probability is a modified form of the axiomatic approach. The probability is a number associated with an outcome of a random experiment (an experiment where the outcome is not previously determined), this number being a linear representation of the likelihood that the associated outcome will be observed, or might be expected to be observed. The probability is 1 for an outcome which will definitely happen, 0 for an outcome which could never happen.

This approach combines the individual definitions and incorporates everything necessary to develop and use probability theory. It can be easily shown that since the probability is linear, the probability of occurrence of any one of some mutually ex-

clusive outcomes is the sum of their individual probabilities, thus fulfilling the last axiomatic condition. Moreover, the relative frequency and classical approaches have both been incorporated, such that something which happens or might be expected to happen, half of the time will have a probability of 0.5; hence, it is possible to assign a number to an outcome which was not previously possible under the axiomatic definition.

This definition is presented as an aid to the understanding of probability theory.

2.1.2 Random Variables

Definition

The definition of a random variable is based on the underlying random experiment and the "events" or possible (numerical) outcomes of this experiment. A random variable is all possible outcomes of a random experiment associated with their probabilities. A discrete example may clarify this: if the experiment is throwing two six sided dice and finding their sum, then the possible outcomes are integers between 2 and 12 each having differing probabilities of occurring — the value 2 has a probability of occurrence of $1/36$ (the dice showing $1 + 1$), whereas the value 7 has a probability of occurrence of $1/6$ (the dice showing $1 + 6, 2 + 5, 3 + 4, 4 + 3, 5 + 2$ or $6 + 1$). The values of this discrete random variable will occur with the same frequency as the outcomes of the experiment.

Probability Distribution and Density Functions

A probability distribution function, $F_X(x)$, is a function associated with a random variable, X , and which gives the probability that an outcome will happen by x ; i.e., the probability that an outcome will be smaller than x_1 is $F_X(x_1)$. Note that $F_X(-\infty) = 0$ and $F_X(\infty) = 1$.

A probability density function, $P_X(x)$, also associated with a random variable, X , assigns a probability to every possible outcome x ; i.e., the probability of the outcome x_1 occurring is $P_X(x_1)$. Strictly speaking, the probability density function gives the probability $P_X(x_1)dx$ that an outcome is between x_1 and $x_1 + dx$. A discrete random variable may be considered as having a probability density function consisting of a series of delta functions.

The probability density function is derived from the probability distribution function, where possible, by

$$P_X(x) = \frac{dF_X(x)}{dx} \quad (2.1)$$

The inverse relation

$$F_X(x) = \int_{-\infty}^x P_X(\eta) d\eta \quad (2.2)$$

also exists.

Expected Value

The expected value (or mean or statistical average) of the random variable X is defined as the sum of all the possible outcomes multiplied by their individual prob-

abilities:

$$\eta = E\{X\} = \int_{-\infty}^{\infty} x P_X(x) dx \quad (2.3)$$

where P_X is the probability density function. When x is a possible value of the random variable X , then $P_X(x)$ is its probability. The mean is a first order moment of a random variable, as will be seen below, but has been dealt with first as it is a concept with which most people are familiar and serves to introduce the notation.

Moments of a Random Variable

The moments of a random variable are defined as

$$m_k = E\{X^k\} = \int_{-\infty}^{\infty} x^k P_X(x) dx \quad (2.4)$$

Here, $m_0 = 1$ and m_1 is the mean, η . Generally of more interest are the central moments, i.e., the moments of a random variable after it has been shifted to the centre of its range so that the expected value is zero:

$$\mu_k = E\{(X - \eta)^k\} = \int_{-\infty}^{\infty} (x - \eta)^k P_X(x) dx \quad (2.5)$$

Here, $\mu_0 = 1$, $\mu_1 = 0$ and μ_2 is the variance, σ^2 , σ being the standard deviation.

The more familiar form of the variance of a (discrete) list of N numbers

$$\sigma^2 = \left(\frac{1}{N} \sum_{i=1}^N x_i^2 - \left(\frac{1}{N} \sum_{i=1}^N x_i \right)^2 \right) \quad (2.6)$$

can be obtained from a relationship between the moments and central moments (found by a binomial expansion of the $(x - \eta)^k$ term in equation (2.5)),

$$\mu_2 = m_2 - \eta^2 \quad (2.7)$$

and by realising that in this case of equally weighted values,

$$m_k = \frac{1}{N} \sum_{i=1}^N x_i^k \quad (2.8)$$

Joint Moments of Two Random Variables

The joint moments of two random variables X and Y are given by

$$m_{kl} = E\{X^k Y^l\} = \int_{-\infty}^{\infty} \int_{-\infty}^{\infty} x^k y^l P_{XY}(x, y) dx dy \quad (2.9)$$

The expected value of a function of two random variables is given, more generally, by

$$E\{f(X, Y)\} = \int_{-\infty}^{\infty} \int_{-\infty}^{\infty} f(x, y) P_{XY}(x, y) dx dy \quad (2.10)$$

The order of the moments is defined as $k + l$ (cf. equation (2.9)), so, for example, the first order joint moments of two random variables X and Y , are $m_{10} = \eta_x$ and $m_{01} = \eta_y$.

$P_{XY}(x, y)$ is the joint probability density function of X and Y . Generally, this must be determined by finding the joint distribution function $F_{XY}(x, y)$ (the probability that X is smaller than x and Y is smaller than y) and differentiating with respect to both x and y . Special cases of interest are:

1. Two independent random variables

$$P_{XY}(x, y) = P_X(x)P_Y(y) \quad (2.11)$$

and

2. Two Gaussianly distributed random variables, X and Y , with means of η_x and η_y , variances of σ_x^2 and σ_y^2 and a correlation coefficient, C_{XY} :

$$P_{XY}(x, y) = \frac{1}{2\pi\sigma_x\sigma_y\sqrt{1-C_{XY}^2}} \times \exp\left(-\frac{1}{2(1-C_{XY}^2)}\left[\frac{(x-\eta_x)^2}{\sigma_x^2} - \frac{2C_{XY}(x-\eta_x)(y-\eta_y)}{\sigma_x\sigma_y} + \frac{(y-\eta_y)^2}{\sigma_y^2}\right]\right) \quad (2.12)$$

It can be seen from the above that two uncorrelated Gaussian variables are also independent, i.e., if $C_{XY} = 0$ then equation (2.12) takes on the form of equation (2.11).

The joint central moments of two random variables are defined by

$$\mu_{kl} = E\{(X - \eta_x)^k(Y - \eta_y)^l\} = \int_{-\infty}^{\infty} \int_{-\infty}^{\infty} (x - \eta_x)^k (y - \eta_y)^l P_{XY}(x, y) dx dy \quad (2.13)$$

The second order central moments are of interest here. These are $\mu_{20} = \sigma_x^2$, $\mu_{02} = \sigma_y^2$ and μ_{11} , which is the covariance of X and Y , given by

$$\mu_{11} = E\{(X - \eta_x)(Y - \eta_y)\} = E\{XY\} - E\{X\}E\{Y\} \quad (2.14)$$

Finally, the correlation coefficient of X and Y is defined as

$$C_{XY} = \frac{E\{(X - \eta_x)(Y - \eta_y)\}}{\sqrt{E\{(X - \eta_x)^2\}E\{(Y - \eta_y)^2\}}} = \frac{\mu_{11}}{\sqrt{\mu_{20}\mu_{02}}} = \frac{\mu_{11}}{\sigma_x\sigma_y} \quad (2.15)$$

The correlation coefficient gives a measure of the similarity of the two random variables. It will have a value of 1 when the random variables are identical (when $X = Y$); a value of 0 when there are no similarities between one random variable and the other; and a value of -1 if one random variable is the opposite of the other (when $X = -Y$).

Central Limit Theorem

Another principle to be applied later is the central limit theorem; this states that the joint probability density function of a sum of independent random variables tends towards a Gaussian distribution as the number of random variables tends to infinity.

Following Goodman^[41]: if $U_i = U_1, U_2 \dots U_N$ are N independent random variables with means of η_i and standard deviations of σ_i , then the random variable Z , defined as

$$Z = \frac{1}{\sqrt{N}} \sum_{i=1}^N \frac{U_i - \eta_i}{\sigma_i} \quad (2.16)$$

will have a probability density function of the form

$$P_Z(z) = \frac{1}{\sqrt{2\pi}} e^{-z^2/2} \quad (2.17)$$

as N tends to infinity. Note that this does not depend on the individual probability density functions of U_i .

The central limit theorem is still applicable with varying degrees of validity for finite N .

2.1.3 Random Processes

Definition

The definition of a random process is similar to that of a random variable, the difference being that where a random variable represents *values* with certain probabilities, a random process represents *functions* with certain probabilities. The definition is again based on an underlying random experiment and the possible outcomes of this

experiment, but here the outcomes are functions. A random process is all possible output functions of a random experiment associated with their probabilities of occurring.

The functions need not be previously defined; an observation of a random process (e.g., noise in a system with respect to time), will in general yield one sample function, $x(t)$. That sample function is now known, but it may not be possible to find it again — another experimental observation will generally give a different sample function.

It should be noted that a random process $X(t)$, as well as being a function $x(t)$ associated with each event, is also a random variable X for each possible (fixed) t .

The probability density function of a random process is now also a function of the same parameters as the random process; for example, if the random process is $X(p, q)$ then the (first order) probability density function is $P_X(x; p, q)$. The moments and central moments can be calculated using this quantity, and will also be functions of p and q .

Stationarity and Ergodicity

A random process is said to be stationary in the strict sense if its statistics are independent of origin; i.e., if $X(t)$ and $X(t + s)$ have the same statistics for any s . This implies that first order statistics are constant, and second order statistics only depend on the difference, s . Reference to stationary quantities later in this work will mean strictly stationary ones.

A random process is ergodic if an average over one sample function (a temporal or spatial average in physical systems) is identical to the expected value of the process for fixed parameters (its ensemble average). This means that the statistics of a random process $X(t)$ can be determined by either one function $x(t)$ or by one of the random variables X at fixed t . Any ergodic process is also stationary.

Moments of a Random Process

The mean of a random process $X(t)$ for fixed t is the expected value of one instance of that random process,

$$\eta(t) = E\{X(t)\} \quad (2.18)$$

Notice that it is a function of t .

Other quantities of interest are the second order moment $E\{X(t)^2\}$, and the second order central moment or variance

$$\sigma(t)^2 = E\{(X(t) - \eta(t))^2\} \quad (2.19)$$

The joint moments of two instances of a random process $X(t_1)$ and $X(t_2)$, are from equation (2.9),

$$m_{kl}(t_1, t_2) = E\{X(t_1)^k X(t_2)^l\} \quad (2.20)$$

$m_{11}(t_1, t_2)$ is the autocorrelation function, $R_{XX}(t_1, t_2)$, of $X(t)$.

The joint central moments of two instances of a random process $X(t_1)$ and $X(t_2)$, are from equation (2.13),

$$\mu_{kl}(t_1, t_2) = E\{(X(t_1) - \eta(t_1))^k (X(t_2) - \eta(t_2))^l\} \quad (2.21)$$

$\mu_{11}(t_1, t_2)$ is the autocovariance of $X(t)$,

Equation (2.21) leads, following equation (2.15), to the correlation coefficient between two instances of a random process $X(t_1)$ and $X(t_2)$:

$$C_{XX}(t_1, t_2) = \frac{E\{(X(t_1) - \eta(t_1))(X(t_2) - \eta(t_2))\}}{\sqrt{E\{(X(t_1) - \eta(t_1))^2\}E\{(X(t_2) - \eta(t_2))^2\}}} = \frac{\mu_{11}(t_1, t_2)}{\sigma(t_1)\sigma(t_2)} \quad (2.22)$$

2.1.4 Differentiation of a Random Process

Papoulis^[40], derives a few important relations for differentiating random processes. First the expected value of the derivative $X'(t)$ of a random process $X(t)$ is equal to the derivative of the expected value of that process:

$$E\{X'(t)\} = \frac{d}{dt} E\{X(t)\} \quad (2.23)$$

The autocorrelation, $R_{XX} = m_{11}$, of the derivative of the process is

$$R_{X'X'}(t_1, t_2) = \frac{\partial^2 R_{XX}}{\partial t_1 \partial t_2} \quad (2.24)$$

If $X(t)$ is stationary, then

$$R_{X'X'}(t) = -\frac{d^2 R_{XX}(t)}{dt^2} = -R''_{XX}(t) \quad (2.25)$$

Finally, note that when $t = 0$, the two random variables are the same and R_{XX} is the second moment of X ; i.e.,

$$E\{[X'(t)]^2\}|_{t=0} = R_{X'X'}(0) = -R''_{XX}(0) \quad (2.26)$$

2.2 Gaussian Random Rough Surfaces

Gaussian surfaces will be considered here since an assumption of Gaussian statistics (as will be seen later) eases analytical calculations, and the surfaces can be

manufactured physically and also created computationally. Here, a mathematical description of a Gaussian surface is given and some of its properties analysed.

The Gaussian random rough surface shall be represented by a stationary random process $S(x, y)$ with a zero mean, $E\{S(x, y)\} = 0$. The probability density function of the process (i.e., the height distribution of the surface) is Gaussian in form with standard deviation σ_S :

$$P_S(s) = \frac{1}{\sqrt{2\pi}\sigma_S} e^{-\frac{s^2}{2\sigma_S^2}} \quad (2.27)$$

Also, a Gaussian correlation function shall be imposed on the surface:

$$C_{SS}(t) = e^{-\frac{t^2}{\tau^2}} \quad (2.28)$$

i.e., the surface has a correlation length τ .

Since the process has a zero mean its autocorrelation is, from equation (2.22),

$$R_{SS}(t) = \mu_{11}(t) = \sigma_S^2 C_{SS}(t) \quad (2.29)$$

Later, the curvature distribution of the surface will be required. This is not difficult to obtain, the distribution of the derivative of a Gaussian process being Gaussian itself (this follows from the fact that any linear combination of Gaussian random variables -- such as differentiation -- is itself Gaussian). All that is required is to find the standard deviation of this new Gaussian distribution and the correlation function of the derivative.

Equation (2.25) gives the correlation function of the derivative distribution (from equation (2.29)) and, again since the mean is zero, equation (2.26), gives the variance of the derivative of the surface.

The autocorrelation, therefore, of the first derivative of the surface height (the gradient), is

$$R_{S'S'}(t) = \left(1 - \frac{2t^2}{\tau^2}\right) \frac{2\sigma_S^2}{\tau^2} e^{-\frac{t^2}{\tau^2}} \quad (2.30)$$

The surface gradient has a Gaussian probability density function (cf. equation (2.27) with zero mean (by equation 2.23)) and standard deviation

$$\sigma_{S'} = \sqrt{R_{S'S'}(0)} = \frac{\sqrt{2}\sigma_S}{\tau} \quad (2.31)$$

Applying this again, the autocorrelation of the second derivative of the surface height (the curvature), is

$$R_{S''S''}(t) = - \left(1 - \frac{4t^2}{\tau^2} + \frac{4t^4}{3\tau^4}\right) \frac{12\sigma_S^2}{\tau^4} e^{-\frac{t^2}{\tau^2}} \quad (2.32)$$

So, the curvature of a Gaussian random rough surface has a zero mean Gaussian distribution with a standard deviation of

$$\sigma_{S''} = \sqrt{R_{S''S''}(0)} = \frac{2\sqrt{3}\sigma_S}{\tau^2} \quad (2.33)$$

2.3 Convolution

Of interest later will be the convolution of two functions $g(x)$ and $f(x)$, generally expressed as $h(x) = f(x) \odot g(x)$ and written

$$h(x) = \int_{-\infty}^{\infty} f(u)g(x-u)du = \int_{-\infty}^{\infty} f(x-u)g(u)du \quad (2.34)$$

The convolution determines the area of the product of the overlapping region of the two functions for the various displacements x of one with respect to the other.

2.3.1 Convolution Theorem

The convolution theorem states that if $F(u)$ and $G(u)$ are the Fourier transforms of two functions $f(x)$ and $g(x)$, then the product of these two transforms is the Fourier transform of the convolution:

$$h(x) = f(x) \otimes g(x) \quad (2.35)$$

$$H(u) = F(u)G(u) \quad (2.36)$$

The proof of this follows simply by taking a Fourier transform of both sides of equation (2.34).

2.3.2 Extension of the Convolution Theorem to Correlation Coefficients

With reference to equation (2.22), if $X(t)$ has a zero mean ($\eta(t) = 0$ for all t), then the correlation coefficient may be written:

$$C_{XX}(t_1, t_2) = \frac{E\{X(t_1)X(t_2)\}}{\sqrt{E\{X(t_1)^2\}E\{X(t_2)^2\}}} \quad (2.37)$$

Now, if $X(t)$ is stationary, i.e., $t_1 = t$ and $t_2 = t + s$, and moreover ergodic — such that the expected value may be rewritten as a time average over a sample function, the two being identical — then:

$$C_{XX}(s) = \lim_{T \rightarrow \infty} \left(\frac{\frac{1}{2T} \int_{-T}^T x(t)x(t+s)dt}{\frac{1}{2T} \int_{-T}^T [x(t)]^2 dt} \right) \quad (2.38)$$

The $1/2T$ term divides through, and the limit may be realised,

$$C_{XX}(s) = \frac{\int_{-\infty}^{\infty} x(t)x(t+s)dt}{\int_{-\infty}^{\infty} [x(t)]^2 dt}$$

Finally, if $x(t)$ is normalised such that the integral

$$\int_{-\infty}^{\infty} [x(t)]^2 dt \quad (2.39)$$

(sometimes referred to as the total energy of $x(t)$) is equal to 1, then the correlation coefficient becomes

$$C_{XX}(s) = \int_{-\infty}^{\infty} x(t)x(t+s)dt \quad (2.40)$$

Notice that this is very similar to the convolution, equation (2.34). If, as with equation (2.34), Fourier transforms are taken of both sides of the equation, a relation similar to the convolution theorem should be expected. In fact, for two member functions $f(x)$ and $g(x)$ of a zero mean ergodic random process (normalised as required above), with Fourier transforms $F(u)$ and $G(u)$, the transform of the correlation coefficient $C(u)$ is

$$C(u) = F^*(u)G(u) \quad (2.41)$$

Where $F^*(u)$ is the complex conjugate of $F(u)$.

Equation 2.41 will be used to calculate the correlation coefficient between two experimental speckle pattern images (see chapter three).

2.4 Electromagnetism

2.4.1 The Helmholtz-Kirchhoff Integral

The derivation below follows that by Born and Wolf^[42] and Beckmann^[19]. The time dependence of various quantities has been suppressed as this work deals only with monochromatic light and does not consider speckle patterns which change with respect to time.

The starting point will be Green's second theorem,

$$\iiint_V E \nabla^2 \psi - \psi \nabla^2 E dV = \iint_S E \frac{\partial \psi}{\partial \mathbf{n}} - \psi \frac{\partial E}{\partial \mathbf{n}} dS \quad (2.42)$$

where the operator

$$\frac{\partial}{\partial \mathbf{n}} = \mathbf{n} \cdot \nabla \quad (2.43)$$

and E and ψ are solutions U to the wave equation

$$(\nabla^2 + k^2)U = 0 \quad (2.44)$$

which exist in the volume V surrounded by the surface S which has an inward pointing normal \mathbf{n} . These solutions mean that the volume integral in equation (2.42) will be zero, so

$$\iint_S E \frac{\partial \psi}{\partial \mathbf{n}} - \psi \frac{\partial E}{\partial \mathbf{n}} dS = 0 \quad (2.45)$$

One of the solutions to equation (2.44), E , is a component of the electric field, and the other, ψ , satisfies some conditions for the geometrical propagation — in the case to be considered this is the spherical, or free space, Green's function:

$$\psi = \frac{e^{ikr}}{r} \quad (2.46)$$

The standard technique for integrating over a function with a singularity is used, namely that of surrounding the singularity by a small sphere with a radius tending to zero, the surface of this sphere connecting with that of the main bulk by an infinitesimally thin 'corridor'. This means that the singularity (here for $\mathbf{r} = 0$), is excluded from the volume contained *within* the surface. Figure 2.1 shows this process, integration of equation (2.45) should now be performed over S and S_1 (and along the corridor joining them, both on the way to S_1 and from it, but the integrals

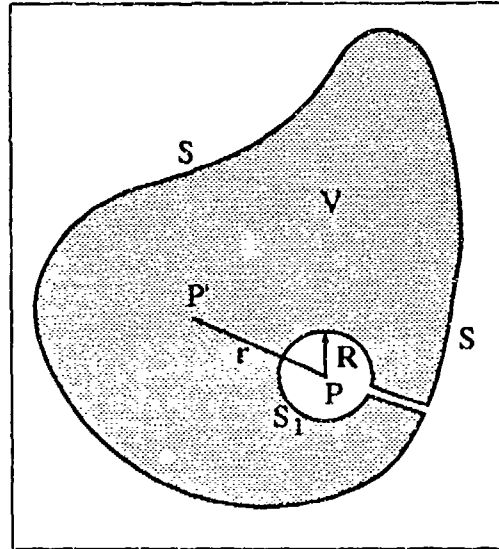


Figure 2.1: Integration over a surface for a function with a singularity at point P .

along this corridor cancel each other and so can be omitted). The integration now becomes

$$\iint_S E \frac{\partial \psi}{\partial \mathbf{n}} - \psi \frac{\partial E}{\partial \mathbf{n}} dS + \iint_{S_1} E \frac{\partial \psi}{\partial \mathbf{n}} - \psi \frac{\partial E}{\partial \mathbf{n}} dS_1 = 0 \quad (2.47)$$

The second term of equation (2.47) can be shown, substituting in equation (2.46) with $r = R$ and since S_1 is spherical, to be $-4\pi E(P)$, in the limit as R tends to zero. $E(P)$ denotes the electric field at the point P . Finally equation (2.47) gives

$$E(P) = \frac{1}{4\pi} \iint_S E \frac{\partial \psi}{\partial \mathbf{n}} - \psi \frac{\partial E}{\partial \mathbf{n}} dS \quad (2.48)$$

This is the Helmholtz-Kirchhoff integral. It gives the electric field at a point P given that it, and its derivative, are known along the surface S . It will be the starting point for calculations later on.

If S is not a closed surface, equation (2.48) will still apply, as a closed surface S' , which incorporates S and encloses all sources, may be considered. The reflectivity of the portion of S' which does not coincide with S will be zero, and hence no

contribution could possibly be made by it to the field at a point P within it.

2.4.2 Polarisation

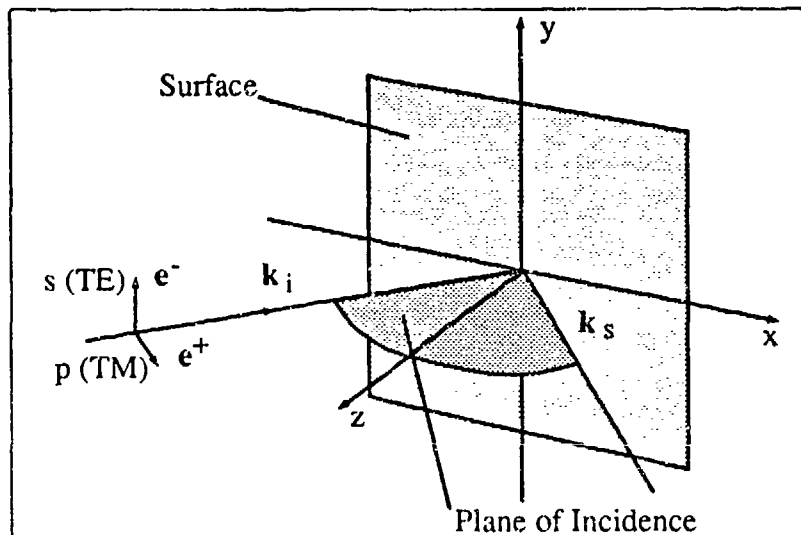


Figure 2.2: Polarisation state definitions.

The polarisation state of radiation is defined by the behaviour of the electric vector as the field propagates through space. In the case where the electric vector is fixed with respect to position/time (i.e., it does not rotate about its direction of propagation), the field is said to be linearly polarised.

Figure 2.2 shows a ray of linearly polarised light, wave vector k_i , striking a surface. The electric vector of the ray is defined within the e^- , e^+ plane; this plane is normal to the wave vector. The plane of incidence in the figure is defined by k_i and the normal to the scattering plane, in this case the z -axis. If the electric vector is lying along the e^- direction, perpendicular to the plane of incidence, the light is s-polarised; if it is lying along the e^+ , parallel to the plane of incidence, it is p-polarised. Any other linear polarisation state may be expressed as a superposition

of these two orthogonal states. The superscripts $-$ and $+$ are used to represent a quantity applicable to the s- and p-polarisation states respectively.

2.4.3 Reflection Coefficients

The Fresnel reflection coefficients, \mathcal{R} , are defined here as a multiplicative factor on an incident wave, upon reflection from a flat plane, to obtain the reflected wave. These reflection coefficients are polarisation dependent such that

$$E_2^+ = \mathcal{R}^+ E_1^+$$

$$E_2^- = \mathcal{R}^- E_1^-$$

and may be complex.

They are expressed as^[42]:

$$\begin{aligned}\mathcal{R}^+ &= \frac{\cos \theta_i \sin \theta_i - \cos \phi \sin \phi}{\cos \theta_i \sin \theta_i + \cos \phi \sin \phi} \\ \mathcal{R}^- &= \frac{\cos \theta_i \sin \phi - \sin \theta_i \cos \phi}{\cos \theta_i \sin \phi + \sin \theta_i \cos \phi}\end{aligned}\quad (2.49)$$

where θ_i and ϕ are the angle of incidence and transmission respectively, as shown in figure 2.3. They are directly applicable at a dielectric interface.

For a metal surface, equations (2.49) can still be applied if the “transmission angle” ϕ is redefined. In general, for a metal surface with complex refractive index $n(1+i\kappa)$ and light incident at an angle of θ_i , the values of $\sin \phi$ and $\cos \phi$ in equation (2.49) are given by^[42]:

$$\begin{aligned}\sin \phi &= \frac{1-i\kappa}{n(1+\kappa^2)} \sin \theta_i \\ \cos \phi &= q e^{i\gamma} = q(\cos \gamma + i \sin \gamma)\end{aligned}$$

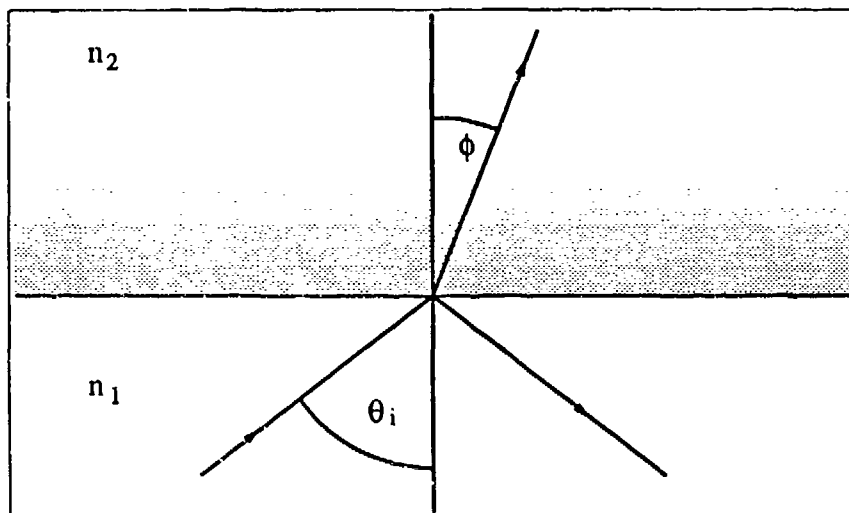


Figure 2.3: The geometry used for defining the Fresnel reflection coefficients.

with q and γ being given by

$$q^4 = \left(1 - \frac{(1 - \kappa^2)}{n^2(1 + \kappa^2)^2} \sin^2 \theta_i\right)^2 + \left(\frac{2\kappa}{n^2(1 + \kappa^2)^2} \sin^2 \theta_i\right)^2$$

$$\tan 2\gamma = \frac{2\kappa \sin^2 \theta_i}{n^2(1 + \kappa^2)^2 - (1 - \kappa^2) \sin^2 \theta_i} \quad (2.50)$$

For a perfect conductor, the reflection coefficients reduce to a very simple form:

$$\mathcal{R}^+ = 1$$

$$\mathcal{R}^- = -1 \quad (2.51)$$

2.4.4 The Kirchhoff Approximation

The Kirchhoff (or Physical Optics) method is a technique for solving equation (2.48), the Helmholtz-Kirchhoff integral. It consists of approximating the surface field (the sum of both the incident and scattered fields at the surface) and its normal derivative at a point on the rough surface to those given by the tangent plane at that point.

This means that the scattered field is simply the incident field multiplied by the reflection coefficient. The approximation may be written as

$$\begin{aligned} E_{is} &= (1 + \mathcal{R})E_i \\ \frac{\partial E_{is}}{\partial \mathbf{n}} &= (1 - \mathcal{R})\frac{\partial E_i}{\partial \mathbf{n}} \end{aligned}$$

where E_i is the incident field, and E_{is} is the field at the surface.

Throughout this work, reference to the Kirchhoff approximation strictly relates to the definition above, *not* a single scatter approximation (to be discussed in chapter four) which usually goes hand in hand with it.

Validity of the Kirchhoff Approximation

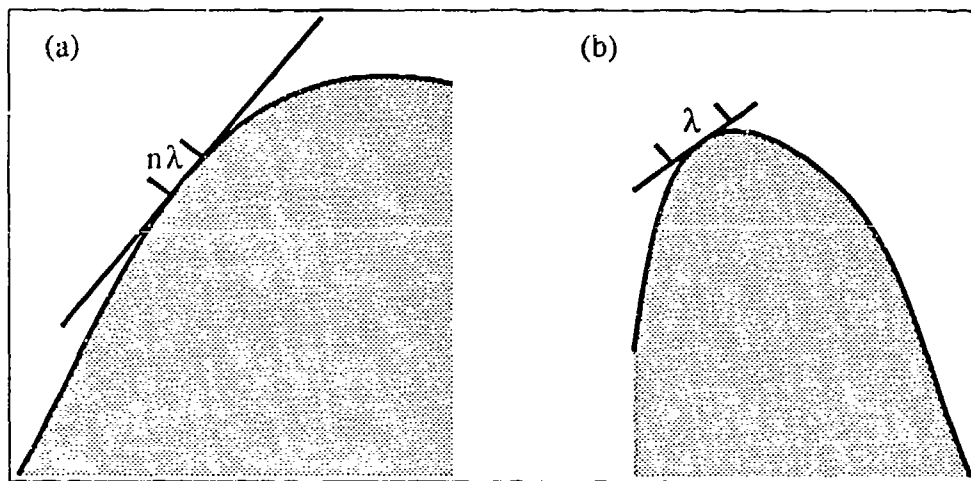


Figure 2.4: The tangent to a surface feature with (a) large and (b) small radius of curvature compared with the illuminating wavelength.

Obviously, the Kirchhoff approximation will be good when the radius of curvature of a surface feature is large compared with the illuminating wavelength (see figure 2.4), or identically, the curvature, \mathcal{C} , is small in comparison with the reciprocal of

the wavelength:

$$C \left(= \frac{1}{r} \right) \ll \frac{1}{\lambda} \quad (2.52)$$

Beckmann^[19] and Ogilvy^[1] state two criteria which are slight variations upon equation (2.52). Both are derived from geometrical considerations; the first is

$$C \ll \frac{4\pi \cos \phi}{\lambda} \quad (2.53)$$

where ϕ is the local angle of incidence on a tangent plane. Unless ϕ is greater than 85 degrees, this inequality will support greater curvatures than will equation (2.52). The second variation,

$$C \ll \frac{\pi}{\lambda} \cos^3 \theta \quad (2.54)$$

again weights the inequality in favour of larger curvatures until the angle of incidence, θ , is greater than 47 degrees.

For an understanding of where these inequalities come from, the reader is referred to section 4.2.2 in reference [1]. The purpose of presenting them here is to show that equation (2.52), to be used below, is sufficient as limitation on the applicability of the Kirchhoff approximation.

The reason for expressing the inequalities in terms of C is that the curvature distribution of a Gaussian random rough surface has already been determined; it is Gaussian, has a zero mean and a standard deviation of

$$\frac{2\sqrt{3}\sigma}{r^2} \quad (2.55)$$

The standard deviation will determine the proportion of the surface curvatures which are large enough to invalidate equation (2.52).

In what follows, an attempt is made to gain some idea of the surface parameters (standard deviation and correlation length) which are allowed within the Kirchhoff approximation. It is important to note that it is the approximation of a surface point to its tangent plane which is being examined here, *not* the validity of the application of the single scattering model (which will be examined in more detail in chapter four). The dependence of the inequalities on the angle of incidence will be ignored, as this only has a noticeable effect when large.

The percentage of curvatures which lie within equation (2.52) is easily determined. Equation (2.33) is substituted in to the limit of equation (2.52); the number of standard deviations available within the Kirchhoff approximation for a particular surface is then

$$N = \frac{\tau^2}{2\sqrt{3}\sigma\lambda} \quad (2.56)$$

which is easily converted into the percentage of curvatures lying within equation (2.52) by noting that the probability distribution for a Gaussian probability density function is the error function. The fraction of curvatures, f , within the limit of equation (2.52) is therefore

$$f = 2 \operatorname{erf}(N) \quad (2.57)$$

Figure 2.5 shows the limits of equation (2.52) for boundaries of $N = 3, 2.5, 2, 1.5$ and 1 (99.7%, 98.8%, 95.5%, 86.8% and 68.3% of curvatures respectively within the limit).

As can be seen from the figure, within the light region (to all intents and purposes), the whole distribution of surface curvatures obeys inequality (2.52); in fact, the majority of these curvatures will be close to zero (the mean) and well within the limit.

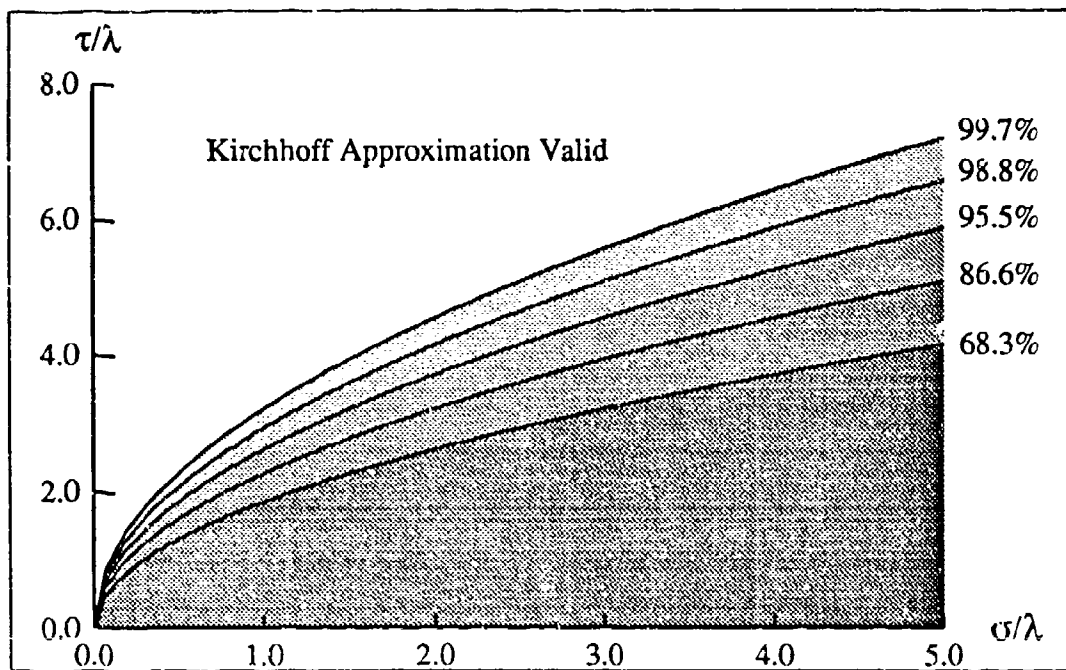


Figure 2.5: Regions of validity of the Kirchhoff approximation for Gaussian surface parameters. The percentages represent the proportion of surface curvatures which lie within the bounds of the limit to the approximation as given by equation (2.52)

Although there is no clear line at which a boundary between applicability and non-applicability may be defined, the Kirchhoff approximation can be applied with confidence to any Gaussian surface within the light region. It is likely to meet less success with surfaces closer to the darker region, fairing worst near to the σ axis.

The dependence of applicability on the angle of incidence will only manifest itself with those surfaces which lie close to the boundary of the 'good' region of the figure, and then only when the angle of incidence is large.

Chapter 3

Experimental Procedures

3.1 Random Rough Surfaces

All of the surfaces to be studied here will be two-dimensional, i.e., the roughness of the surface will not depend upon direction — it will vary as a function of both x and y . They will also have Gaussian height distributions and correlation functions. — the reasons for this are that it is possible to create a surface with known Gaussian statistics; it is easy to work theoretically with such surfaces and that there already exists a selection of Gaussian surfaces whose parameters are known and whose scattering properties have been investigated^[12]. One-dimensional surfaces are not considered in this work as they do not produce the required two-dimensional speckle patterns.

3.1.1 Surface Manufacture

In order to gain a measure of control over the statistical properties of the surfaces, a method developed by Gray^[15] was used. This method involves coating a glass substrate with a layer of a photoresist which has an approximately linear height re-

sponse to exposure time. The coated substrate is then exposed to speckle patterns created by illuminating ground glass. The surfaces used for experimental measurements presented in this work were not manufactured by the author, but were chosen to enable comparisons with existing published work.

Preparing the Substrate

The aim here is to deposit a flat layer of photoresist onto the glass substrate (approximate dimensions of $50 \times 50 \times 3\text{mm}$), with sufficient thickness to allow a surface with an rms height of at least $2\mu\text{m}$ to remain after the necessary etching. This turns out to be an initial coating around $11\mu\text{m}$ thick.

The first stage to be considered will be cleaning the glass substrate; this is important, not only for improving the adhesion of the photoresist, but also to remove any traces of dirt or chemical impurities which may affect the final coating. Initially, the glass plates are washed in hot water with a detergent to remove grease and dirt. Next, the plate is cleaned with acetone to remove any chemical deposits on the surface — some of which will be left by the detergent. Finally, the plate is wiped with isopropanol. This last stage is necessary since it was found that acetone leaves deposits which adversely affect the photoresist, producing striations.

The photoresist used, which was found to have a good linear response to the exposure time, is Shipley S1400-37. This photoresist is also sufficiently viscous to produce a thick coat on the substrate. The method of spin coating is used to deposit the photoresist onto the substrate; the figures given below were found empirically, and produce a uniform coat of photoresist of between 10 and $12\mu\text{m}$ thickness.

A cleaned substrate is fastened to the centre of a turntable set up to spin at 300 revolutions per minute. While the turntable is stationary, photoresist is applied to the centre of the substrate with a syringe, until the natural spread of the liquid reaches the edges of the glass, about 3ml. The turntable is now set spinning for four minutes. Again with the substrate stationary, a similar dose of photoresist is applied. Finally the turntable is spun for a further four minutes.

After allowing twenty four hours to dry at room temperature, the coated substrates are baked, at ninety degrees celcius (this is below the temperature at which the photoresist melts) for thirty minutes, to drive off any remaining solvent in the photoresist layer. It is now ready to have a surface profile imposed upon it.

A few factors need to be considered during the manufacture of the coated plates. In order to produce a perfectly flat layer of photoresist, air bubbles must not be allowed in the photoresist; as long as care is taken with the syringe then the process outlined above will ensure this. Dust must not be allowed onto the plates at any stage during manufacture; one speck of dust can produce a relatively large area which will not react properly to exposure — this is especially a problem during the twenty four hour drying period, any dust settling on the surface during this time will stick, and after exposure, a spike can remain sticking up above the surface. It is possible for dust to settle on the photoresist near the edges of the plate without invalidating its use as a surface. Finally, care must be taken not to scratch the photoresist, compressed air should be used to remove any dust which settles after drying.

Etching the Surface Profile

The required surface profile, as mentioned previously, is Gaussianly distributed. Fortunately, a profile of this approximate nature can be achieved by simply exposing the photoresist to eight uncorrelated speckle patterns, the number being found as follows.

It can be shown that the probability density of the intensities in a speckle pattern with mean intensity η obeys negative exponential statistics^[40],

$$P_I(I) = \frac{1}{\eta} \exp\left(-\frac{I}{\eta}\right) \quad (3.1)$$

and that the (unnormalised) probability density function of a superposition of N uncorrelated speckle patterns, each with mean intensity η , is

$$P_I(I) = \frac{I^{N-1} N^N}{(N-1)! \eta^N} \exp\left(-\frac{IN}{\eta}\right) \quad (3.2)$$

The variance for this intensity distribution is

$$\sigma^2 = \frac{\eta^2}{N} \quad (3.3)$$

Repeated integration by parts is necessary to find this.

Figure 3.1 shows the form of this distribution for various N . Eight speckle patterns are taken as the optimum number to achieve a Gaussian profile with the maximum possible variance — the number at which a Gaussian curve, with a variance equal to that given by equation (3.3), is most similar in shape to the probability density function, equation (3.2). Note that as N increases, the profile becomes more Gaussian (cf. central limit theorem), but the variance of the distribution reduces, thus

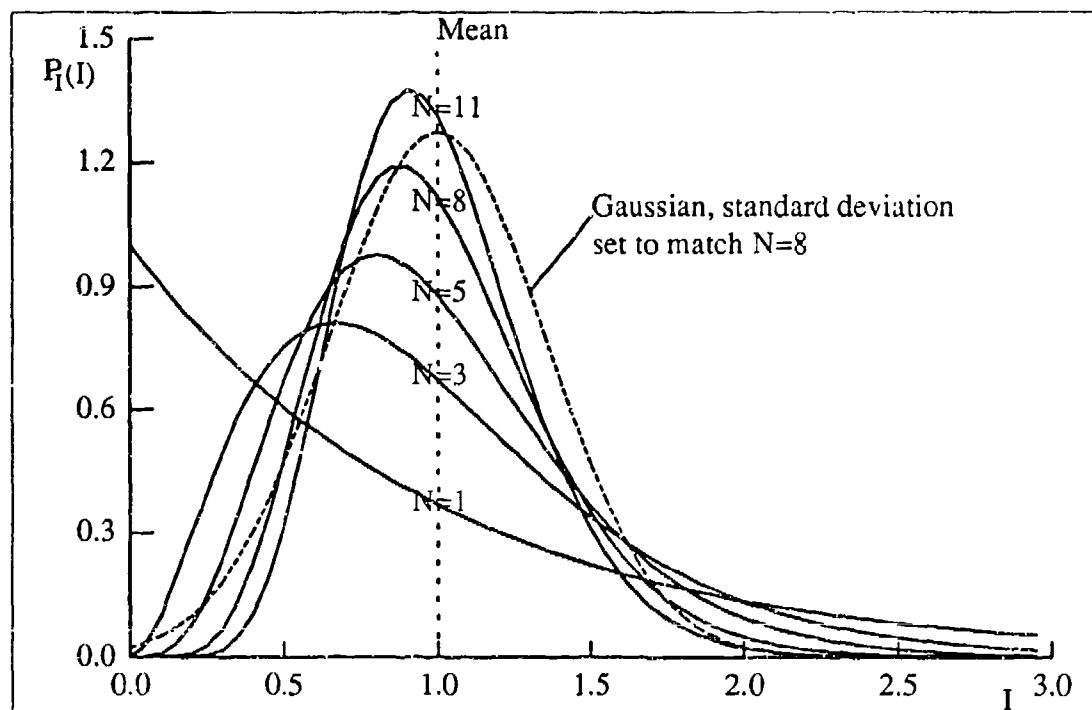


Figure 3.1: The probability density distribution of the intensity of the superposition of N uncorrelated speckle patterns, each with mean $\eta = 1$, for various N .

reducing the rms surface height — a quantity potentially required to be as large as possible.

These eight uncorrelated speckle patterns are created by illuminating, in turn, separate plates of ground glass with the 457.9nm wavelength of light from an argon ion laser. The photoresist used is particularly responsive to wavelengths approaching the ultraviolet region of the spectrum.

The geometrical arrangement for the exposure of the coated substrates is given in figure 3.2. Collimated light is incident on the ground glass diffuser in an attempt to produce a uniform field at the surface — important to give a uniform statistical variation to the surface height. The size of the illuminated area of the diffuser, and

the distance of the substrate from it, determine the speckle size on the photoresist — this determines the correlation length (the $1/e$ point of the autocorrelation function) of the surface.

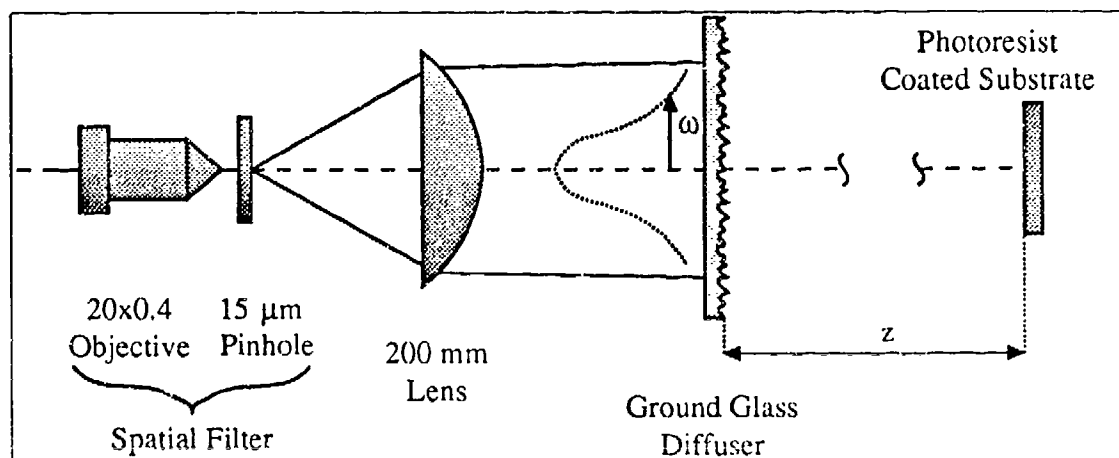


Figure 3.2: Arrangement for exposure of photoresist coated plates during surface creation.

For a more precise idea of how the arrangement will affect the correlation length of the surface, a simple statistical study is necessary. Given that the beam incident on the ground glass plate has a Gaussian cross-section, then the correlation between two points of the speckle pattern is^[4]

$$C_I(\Delta r) = \exp \left(- \left[\frac{\sqrt{2}\pi\omega\Delta r}{\lambda z} \right]^2 \right) \quad (3.4)$$

where it has been assumed that the speckle pattern is statistically stationary. Δr is the distance between two points of the speckle pattern, and ω is the $1/e$ half width of the Gaussian beam profile at the ground glass plate. λ is the wavelength of the light, and z is the distance of the surface from the diffuser.

From equation (3.4) it can be seen that the correlation length of a speckle at the

surface, and hence the correlation length of the surface, will be

$$\tau = \frac{\lambda z}{\sqrt{2\pi}\omega} \quad (3.5)$$

The parameters z and ω in the arrangement can be adjusted until τ is of the required size. Generally z will be set such that it is just large enough for the speckle field to appear uniform over the substrate (about 400mm), anything larger would just reduce the amount of power incident on the photoresist and hence increases exposure time. This leaves ω as the main handle on τ , but because it is not possible to measure the $1/e$ half width of a Gaussian beam quickly and precisely, especially for large τ when ω is small (if the required τ is 150 μ m then ω is approximately 0.3mm — for the wavelength and distance specified above), τ can only be roughly controlled. Fine tuning is readily achieved by adjusting z slightly.

The rms height of the surface can be controlled by exposure time; the maximum time, before the photoresist is removed down to the glass substrate, has been determined experimentally for substrates prepared using the procedure described above, and is given in minutes by

$$t = \frac{275}{I} \quad (3.6)$$

where I is the average light intensity in the plane of the substrate *in the arbitrary units given by the "Berry meter"*. The number 275 was found experimentally, and converts the intensity readings given by the meter into minutes of exposure time. The finally calculated exposure time should be divided by eight and each speckle pattern should be projected onto the photoresist for this time. This maximum exposure will give the surface an rms height of approximately 2 μ m.

After all exposures are complete, the surface is developed in a mixture of one part by

volume of Shipley AZ-303 to five parts water for thirty seconds. Finally, the surface is rinsed under running water for about three minutes, and dried with compressed air. A quick check should be made to ensure that the glass substrate has not been exposed through the photoresist at any point.

3.1.2 Gold Coating

The last stage in the fabrication of a surface is to deposit a thin layer of gold, using vacuum deposition equipment, onto the photoresist. This layer provides a highly conductive front to the surface, enabling its scattering properties to be compared with theoretical studies which assume the surface is a perfect conductor.

The complex Fresnel reflection coefficients for gold are given by the sequence of equations in chapter two, starting with equations (2.49). The square magnitudes of the coefficients, \mathcal{R}^+ and \mathcal{R}^- , the reflectivities, are shown with respect to angle in figure 3.3, the refractive index of the gold taken at a wavelength of $0.633\mu\text{m}$ as $0.167 + 3.149i$ ^[42]. It can be seen that the curves are close to unity and approximately flat, indicating that the reflection coefficients are only loosely dependent on the angle of incidence; a favourable comparison with a perfect conductor where $|\mathcal{R}|^2$ is 1 for both polarisation states.

3.1.3 Surface Characterisation

Since only rough control over the statistical parameters of the surface is attainable, a method is required to gauge more accurately what these parameters are. For all of the surfaces mentioned in this work, a Rank Taylor-Hobson Talystep mechanical

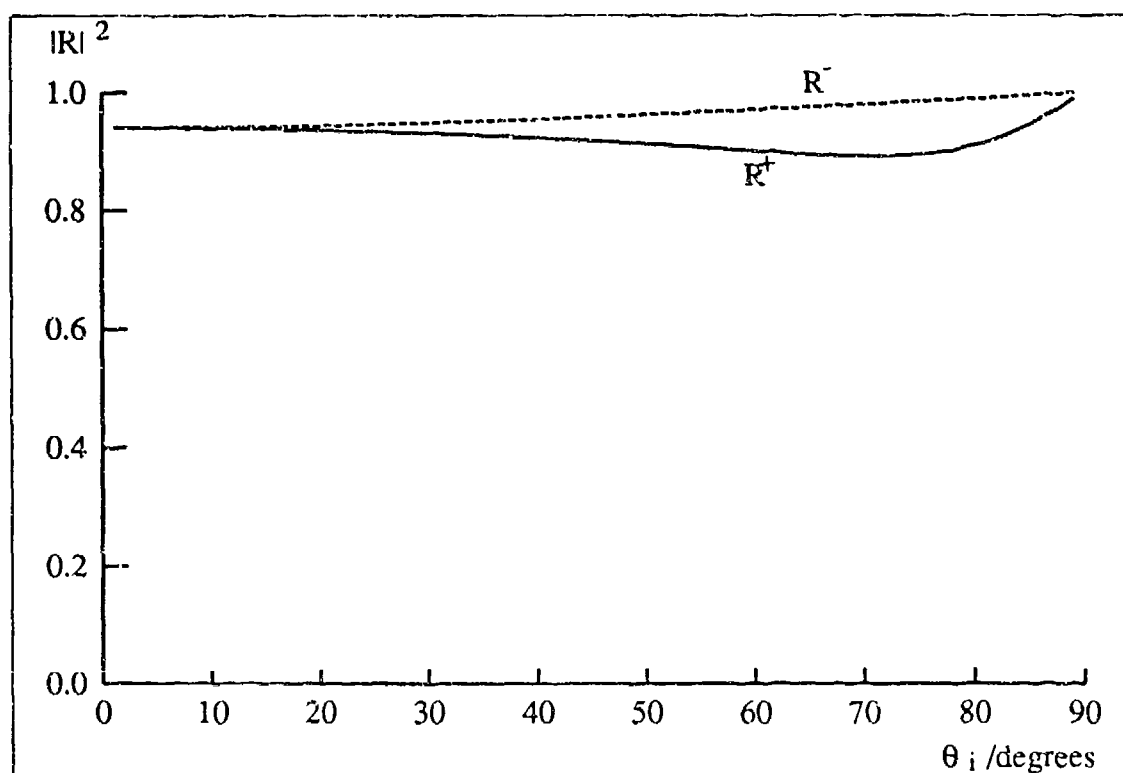


Figure 3.3: Fresnel reflection coefficients for gold at $\lambda = 0.633\mu m$ over a range of angles.

surface profilometer was used. It has been shown that this instrument does not significantly damage the surface^[43]; nevertheless, measurements were made away from the region on which light was to be incident, and the assumption that the statistics are uniform over the whole surface was made.

The profilometer operates by dragging a stylus across the surface; the stylus available was a diamond wedge of dimensions $1.8 \times 0.5\mu m$. A force is applied to the stylus to maintain its position in contact with the surface, and this force varies as the height of the surface changes. Generally the load applied to the stylus should be around $6mg$ at the middle of its displacement range, this will mean that for a typical surface, the force should vary between about $2mg$ and $10mg$ at the extremes of the

range. The force is not constant as this is the quantity which is measured by the instrument and converted into an electrical signal. This electrical signal is amplified and filtered to remove high frequency vibrations, finally passing to an analogue-to-digital converter. The end result of this process is a digital representation of a 2mm line on the surface; computational processing can now be performed to find the various statistical quantities.

Processing the Profilometer Data

As it is not likely that the surface could be positioned, by hand, exactly level under the stylus, the trace must have any overall trend in its gradient removed before either of the surface parameters can be obtained it. To achieve this, a straight line is fitted to the data by the least squares method, where the surface height at any position along that line is the distance to the trace along a perpendicular to the line. In other words, the trace is shifted to the origin and rotated such that the mean height and the mean gradient are both zero. The gradients removed by this method can be smaller than 0.001.

The standard deviation of the trace is now easily calculated. This will be the standard deviation (rms height) of the surface over the length of the scan. Figure 3.4 shows a histogram of the distribution of heights over one scan, a Gaussian curve is also shown with the same standard deviation. It can be seen that the data has a form which is roughly Gaussian, the departure being due to the long correlation length of the surface presented. The actual value of the standard deviation attributed to the surface will be the average of many such individual trace values; the error associated

with it will then be the standard deviation of the spread of values.

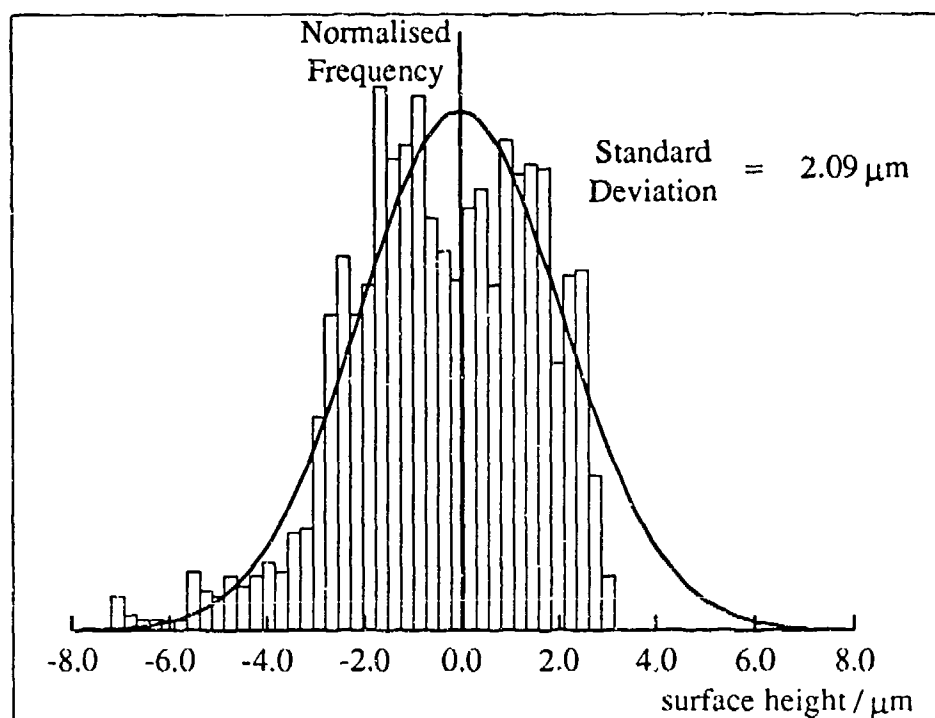


Figure 3.4: Histogram of the surface heights over a single scan of a surface (surface #80 — see later), a Gaussian curve with the same variance is also shown.

The correlation length of the surface is obtained by performing an autocorrelation on the trace. The result, after dividing by the variance, is the autocorrelation function. This will be approximately Gaussian in form (since the beam profile used to create the surfaces was approximately Gaussian), at least for very low lag (Δr) values:

$$C_{SS}(\Delta r) = \exp\left(-\frac{\Delta r^2}{\tau^2}\right) \quad (3.7)$$

A least squares fit of this will give the correlation length:

$$\tau = \sqrt{-\frac{\sum_{i=1}^n x_i^2 \ln y_i}{\sum_{i=1}^n (\ln y_i)^2}} \quad (3.8)$$

Figure 3.5 shows the correlation function calculated for a surface trace. Equation (3.7) is also plotted for a correlation length calculated by equation (3.8) for the

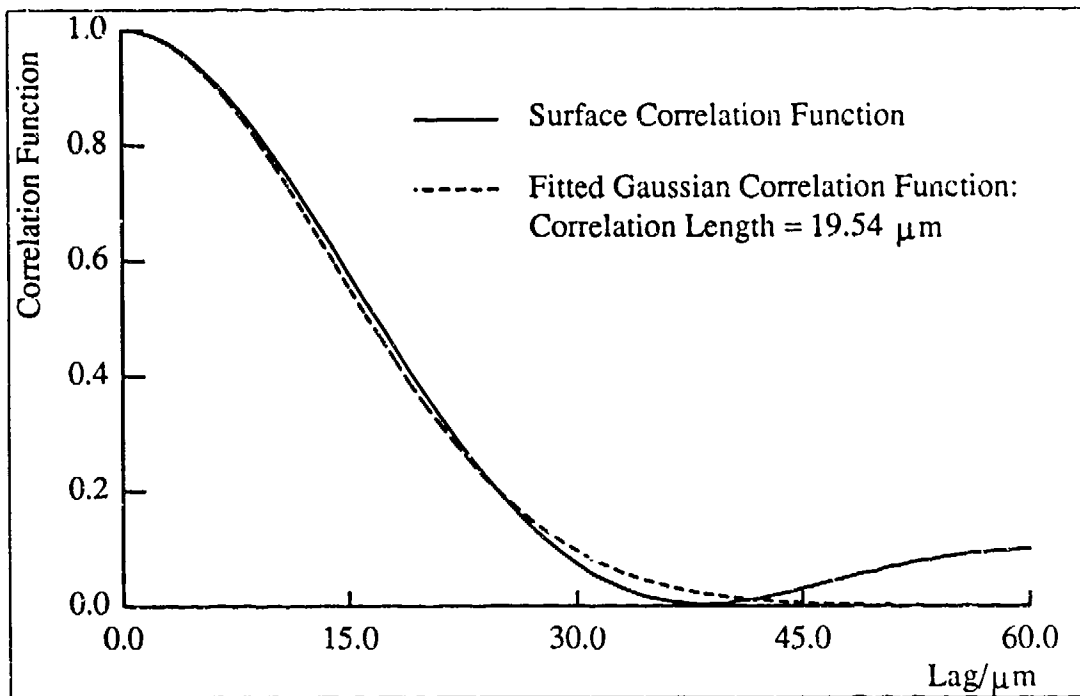


Figure 3.5: The correlation function of a surface scan, a fitted Gaussian correlation function has a correlation length of $19.54\mu m$.

portion of the function which has a value greater than 0.1; i.e., n in equation (3.8) is determined by the point at which the data first drops below 0.1 with increasing lag. This is necessary because as at higher lags, the correlation function will only go to zero for an infinite trace length. Again the parameter for the surface and its error are obtained by averaging many such correlation lengths.

Stylus Size Considerations

For a surface where the radius of curvature of the features is greater than the width of the stylus tip, it can be assumed that the size of the tip will not greatly influence the measurements obtained. However, once the surface features are of a similar size to the stylus used to trace them, the tip dimensions will affect the measured

surface heights. The $1.8\mu\text{m} \times 0.5\mu\text{m}$ stylus used here is suited to the analysis of one-dimensional surfaces, and does not introduce significant error in these cases^[43]; but with a two-dimensional surface, the extra width along one side will prevent the stylus from properly tracing the surface portion underneath its centre. The stylus will in fact trace the *highest* points under the whole of its width, as can be seen in figure 3.6.

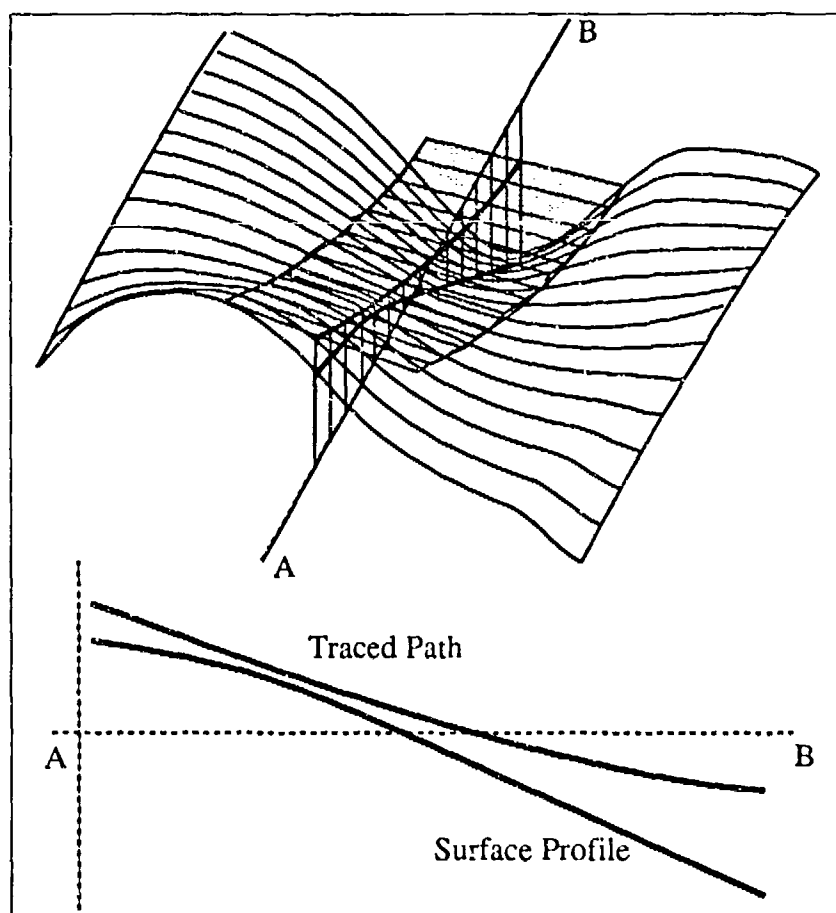


Figure 3.6: Finite stylus tip size prevents accurate tracing of surface features of a similar size. The scale has been exaggerated, generally the effect is much less noticeable.

The errors introduced to the surface parameters have been examined^[43], based on an assumption of a circular tip^[44]. Relations derived between the measured surface

parameters and the actual values, for Gaussian surfaces with a Gaussian correlation function, such as those studied here, are:

$$\sigma_m^2 \approx \sigma^2 \left[1 - \frac{\gamma^2 R^2}{6} \left(1 - \frac{6\sigma^2}{\tau^2} - \frac{12\sigma^4}{\tau^4} \right) \right] \quad (3.9)$$

$$\tau_m^2 \approx \tau^2 \left[1 - 15\gamma^2 R^2 \left(\frac{\sigma}{\tau} \right)^4 \right] \quad (3.10)$$

where the subscript m represents the value as measured by a stylus tip with radius R and γ is the rms curvature of the surface:

$$\gamma = \frac{2\sqrt{3}\sigma}{\tau^2} \quad (3.11)$$

as derived in chapter two.

The actual effect of this finite tip size ($1.8\mu m$ across the width) will introduce an error of less than two percent to the measured parameters; although much larger than for one-dimensional surfaces, it is still swamped by the statistical uncertainty, even for the roughest of surfaces studied here (see below).

3.1.4 The Surfaces Studied

Three surfaces will be used in the experimental investigation, all of which are approximately Gaussian in both height distribution and correlation function. The parameters of these surfaces are given in table 3.1. Surface #80 has previously been reported to be a Beckman surface, i.e., it exhibits only single scattering^[12]. Surface #83 is one which shows strong enhanced back-scatter, a multiple scattering phenomenon^[12]. Both of these surfaces were manufactured by Mendez and O'Donnell. Surface #239 was chosen as an 'in between', it is expected to border on the realm of multiple scattering — this was manufactured by Kim^[41].

Surface	$\sigma / \mu m$	$\tau / \mu m$
#80	2.27 ± 0.2	20.7 ± 2.0
#239	1.34 ± 0.1	7.0 ± 0.5
#83	0.9 ± 0.1	2.73 ± 0.08

Table 3.1: Rms height and correlation length for the surfaces to be studied.

The surfaces have been plotted on a graph showing the validity region of the Kirchhoff approximation (up to 99.7% of curvatures valid) in figure 3.7. It can be seen that all three surfaces have gradients varying sufficiently slowly for the Kirchhoff approximation to be expected to apply.

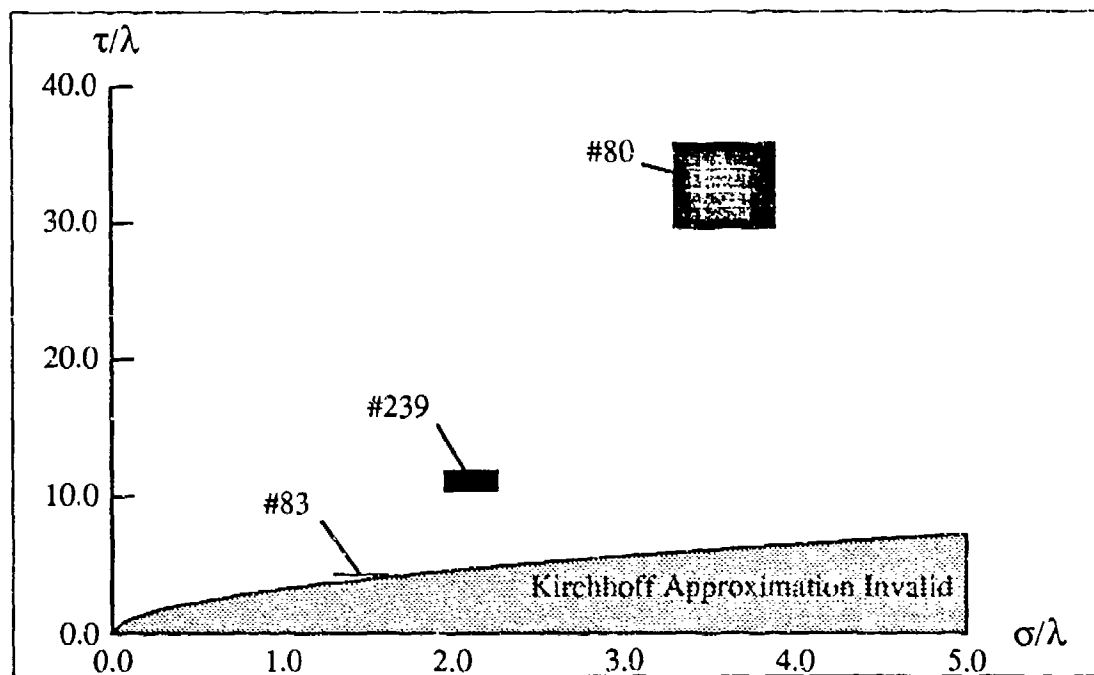


Figure 3.7: Surfaces #80, #239 and #83 plotted on the Kirchhoff validity graph for a wavelength of $\lambda = 0.633 \mu m$. The large black areas represent the errors in the measurements of the surfaces.

3.2 Obtaining the Angular Correlations

3.2.1 Experimental Equipment

The equipment used is shown in figure 3.8. The illumination source is a Uniphase 10mW Helium-Neon laser emitting linearly polarised light at a wavelength of 633nm. The orientation of the laser controls the polarisation of the light incident on the surface. The speckle patterns are digitised with a Princeton Instruments 512 × 512, 27 μ m pixel, sixteen bit peltier cooled CCD camera (accurate to one bit — the readout noise is about 10 photoelectrons), and transferred to an magneto-optical disk for later off line processing. A polariser is positioned in front of the camera to enable control over which component of the scattered light is detected. No imaging optics are used, a speckle pattern being formed at the CCD element purely by the free space propagation of light from the surface.

The camera was not actually mounted on the end of the arm as shown in figure 3.8 since its weight would have put an unnecessary stress on the rig's bearings. Instead, a counter weight was removed from the arm, and the camera was mounted in its place — much closer to the bearings — as shown in figure 3.9.

As the camera is now mounted behind the surface, a mirror must be positioned at some length along the arm, angled such that the light scattered around the specular direction is sent towards the camera. The camera's position and the angles the camera and mirror were tilted at were chosen to give a path length from the surface to the camera of around 900mm. The camera was also high enough above the surface that its view was not obstructed by the surface mountings. Fine control of

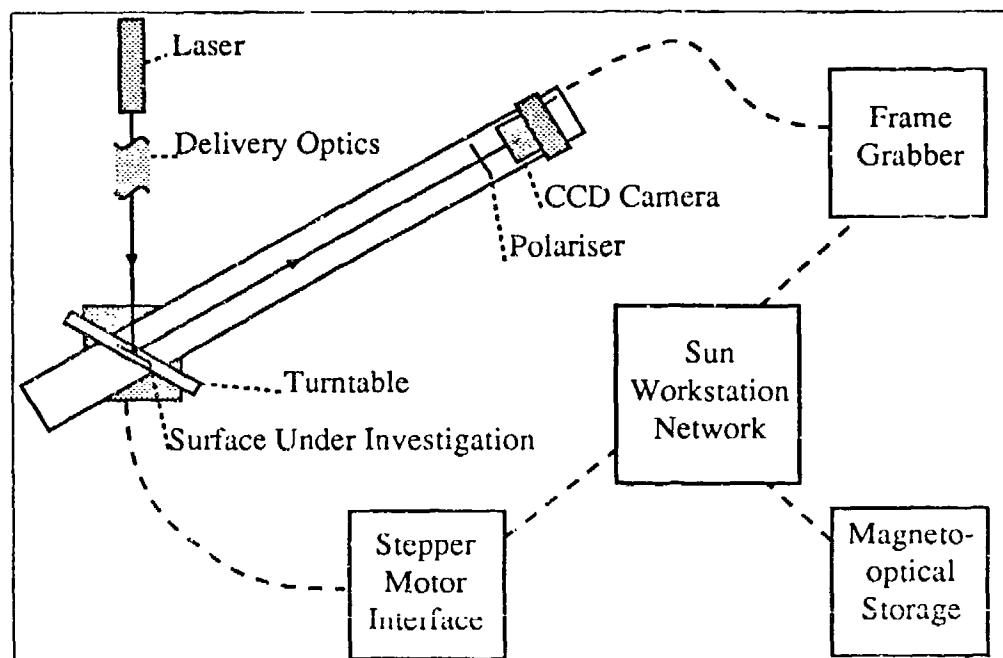


Figure 3.8: Schematic diagram of the rig used to control incidence and viewing angles.

the path length was obtained by moving the mirror along the arm and illuminating the surface at a height which would mean the centre of the camera was looking exactly at the laser spot.

The angles of the mirror and camera mounts were cut to a tolerance of less than 0.1 degrees. A measurement of the path length after construction gave a distance of $900 \pm 5\text{mm}$.

The size and number of speckles formed at the CCD element is an important consideration. Obviously, a large number of speckles in an image mean that the statistical properties of that image, such as the mean and variance, can be well defined. However, this desirable criterion must be traded against the need for each individual speckle to be well defined, a limitation imposed by the pixel size of the CCD array.

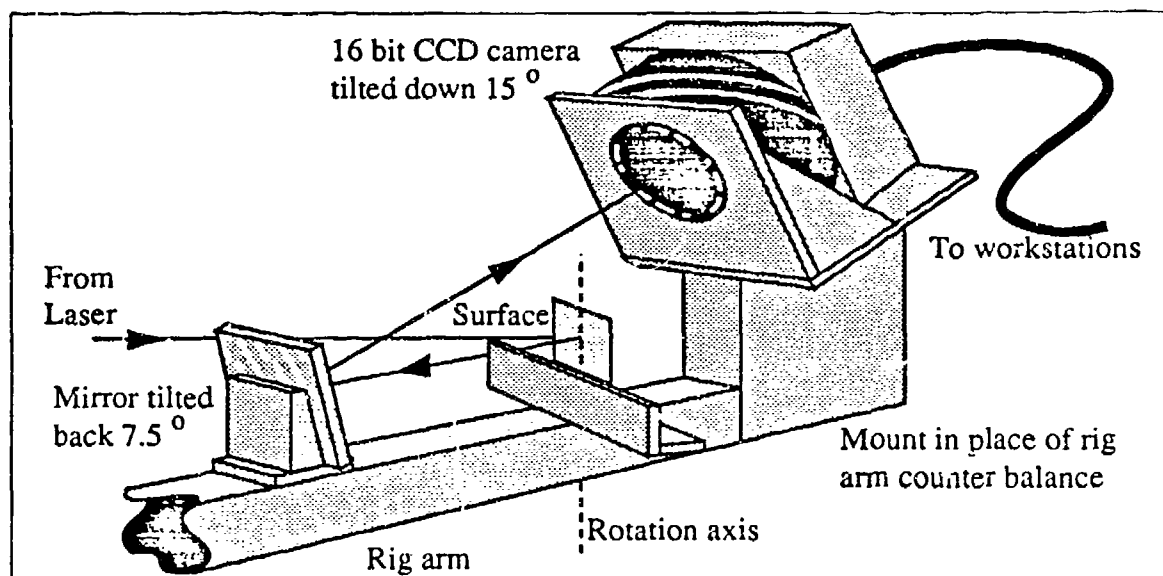


Figure 3.9: The actual arrangement used to mount the camera. The camera is still looking in the specular direction of scattering from the surface.

The speckles in the image must each have sufficient intensity information in order for a correlation to be meaningful. Speckles with a ten pixel diameter provide this information, while still allowing around 400 speckles over the whole image.

The number of speckles on the CCD element is controlled by the size of the illuminating spot on the surface. Since the detector is in the far field, the speckle size, ω , will be set by the diffraction limit of the system, roughly given by:

$$\omega = \frac{1.22\lambda f}{D} \quad (3.12)$$

the aperture diameter, D , being the beam size at the surface and the focal length, f , being the distance of the detector from the surface (in this case, 900mm assuming the beam comes to a focus at the CCD element). If radius of a speckle is ω , the area of a speckle, $\pi\omega^2$, is the $14 \times 14\text{mm}^2$ CCD element area divided by 400 (the number of speckles required), about 0.5mm^2 . The required beam diameter, on the surface from the above equation is therefore roughly 3mm.

Note that the CCD element subtends an angular of around 0.9 degrees in both directions to the surface (solid angle, 0.0002 steradians); an individual speckle has a width of about 2.5 arc minutes subtended from the surface.

Control of the angle at which the incident beam strikes the surface (the orientation of the surface), and the angle at which the camera is positioned (the orientation of the rig arm), is by means of two stepper motors. These provide an angular resolution of 2' (two arc minutes) per step. Currently, the geometical situations attainable with the rig are limited to those of 'in-plane' scattering — the surface normal, incident beam and direction of observation all lying in a plane. This, however, is not a problem here as observation is confined to the specular direction.

A PC, which performs many duties in the laboratory, provides the interface to the stepper motors. The Sun workstation controlling the experiment communicates with the PC via a serial line.

Due to the nature of the measurements sought, special care must be taken to ensure that the centre of the laser beam is targeted exactly on the axis of rotation of the surface. Failure to achieve this will mean that at different angles of incidence, separate portions of the surface will be illuminated.

In order to gain the maximum advantage offered by the camera, the integration time is raised or lowered such that the maximum pixel value in any one image is between 50000 and 65000 (the maximum value attainable being 65535). This means that as the intensity changes over the range of speckle patterns, the camera will adjust to utilise most of its intensity resolution. The maximum intensity the camera can view is limited by the fastest shutter speed (about 10ms). As the correlation process

described below removes any dependence on the overall intensity of the speckle pattern, upsetting the relative intensities between the patterns will not affect the correlation results.

3.2.2 The Speckle Patterns

Figures 3.10, 3.12 and 3.11 show histograms, taken from a single frame of the raw camera data of speckle patterns, obtained from surfaces #80, #239 and #83 at various angles of incidence, and for different polarisation arrangements.

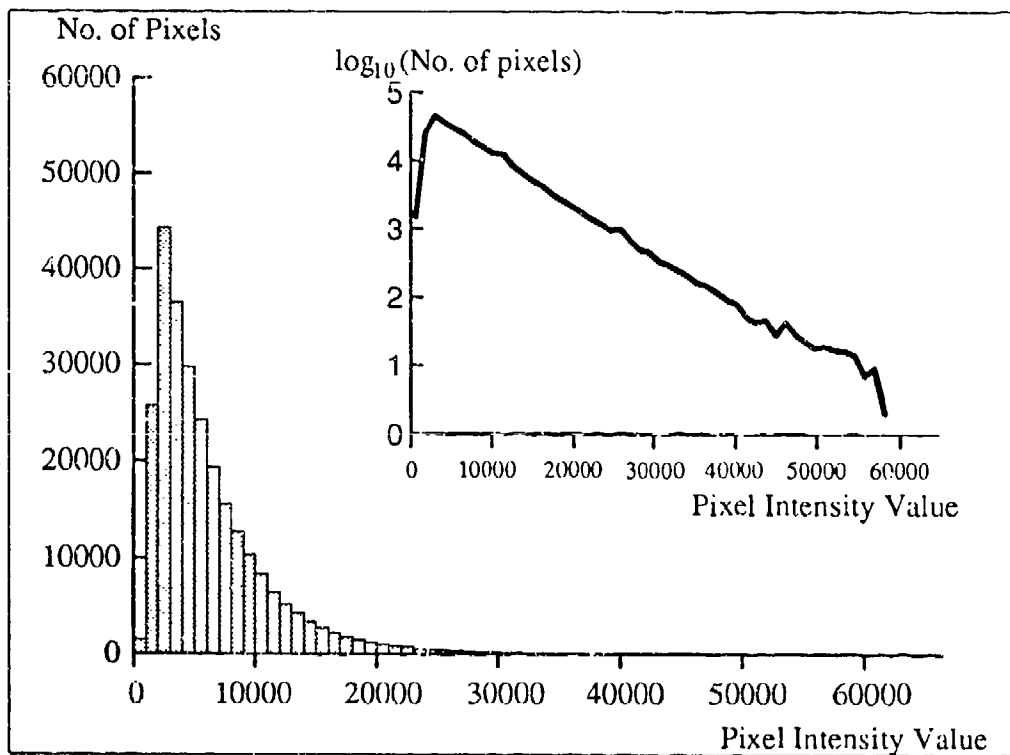


Figure 3.10: Histogram of the intensity values of a speckle pattern formed by surface #80 at ten degrees incidence and observation in the specular direction. Incident and detected light are both s-polarised. The same data plotted on a log scale is inset.

As can be seen, surface #80 and surface #83 produce speckle patterns that have

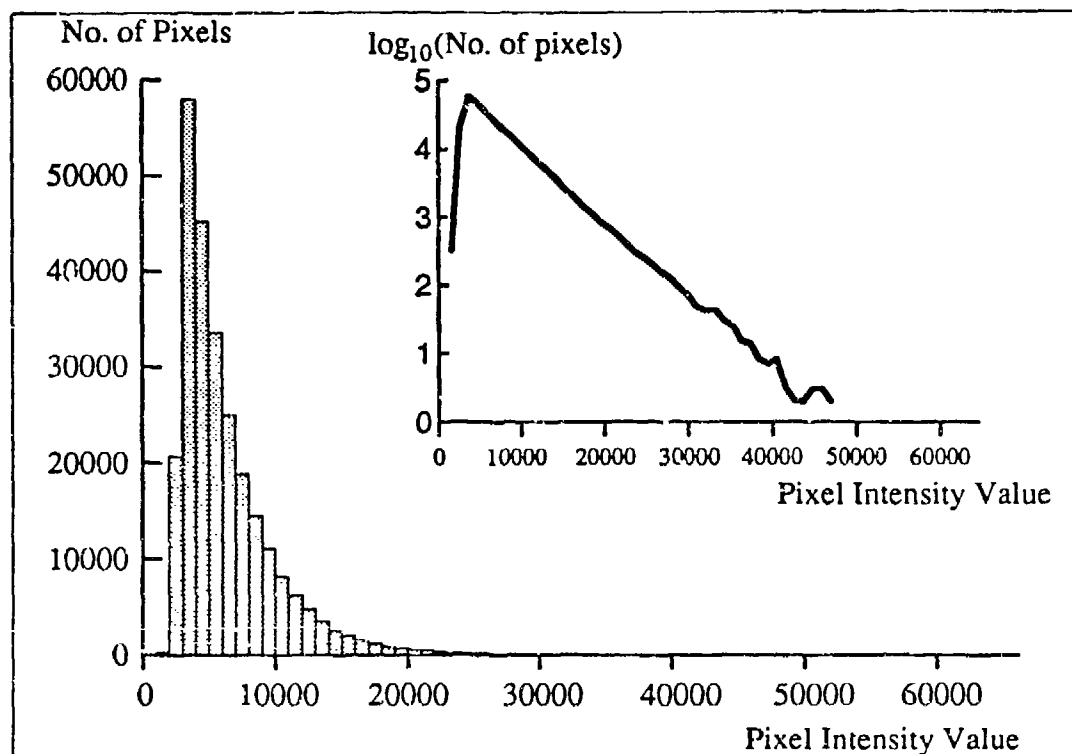


Figure 3.11: Histogram of the intensity values of a speckle pattern formed by surface #83 at fifty degrees incidence and observation in the specular direction. Incident light is p-polarised and the observed pattern is s-polarised. The same data plotted on a log scale is inset.

roughly the negative exponential histogram expected^[45], but that the first few bins are considerably less than they should be. This may be explained by noting that a large amount of light is scattered around the laboratory by the rough surfaces, and that this will be registered by the camera as an ambient light level, adding to every pixel and shifting the histogram to the right; i.e., zero is no longer the most probable intensity.

The quantity $\sigma_I/\langle I \rangle$, which should be 1 for a true negative exponential, for the speckle pattern in figure 3.10 is 0.72. This increases to 0.91 if the first two bins of the histogram are removed from the calculation, giving evidence that ambient light

is the distorting factor. This may be shown further by supposing that the lowest bin of the negative exponential should contain all the light which has appeared in the two lower bins — adding this in gives a $\sigma_I/\langle I \rangle = 0.98$. The errors on these figures may be considered as $\pm 5\%$, being the statistical error on a sample of 400 speckles.

For figure 3.11, $\sigma_I/\langle I \rangle$ is 0.54, but increases to 0.88 after subtraction of the first three bins. If the subtracted amount is added into what was the fourth bin then the value increases to 0.93. As above, these figures have an error of $\pm 5\%$.

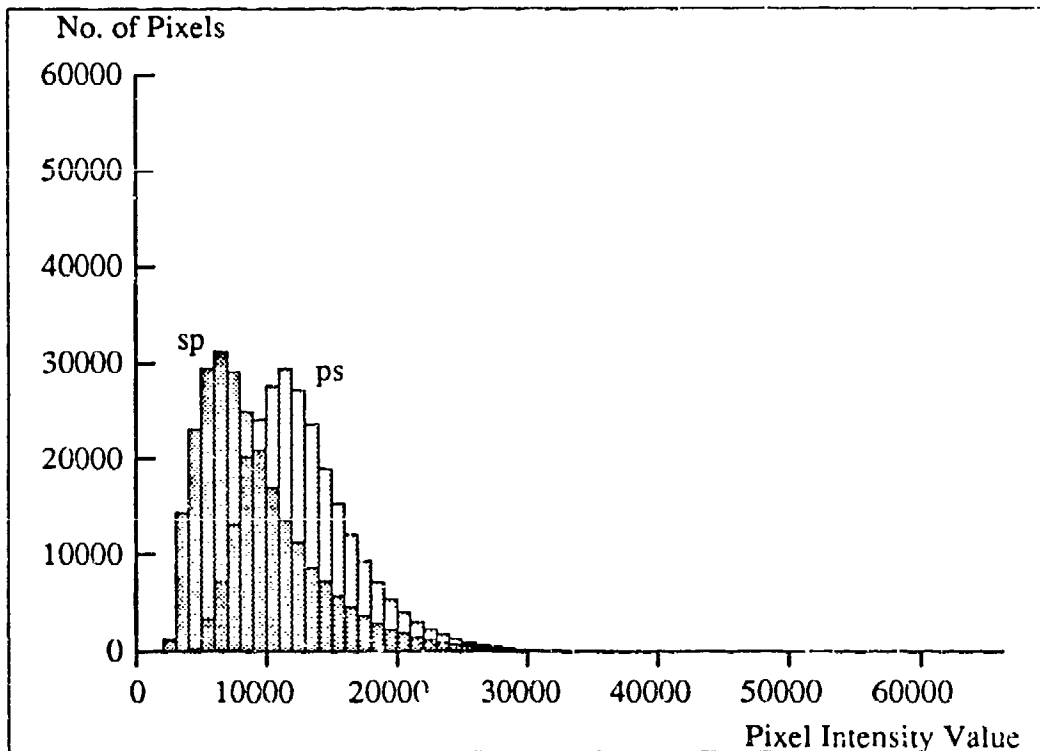


Figure 3.12: Histogram of the intensity values of a speckle pattern formed by surface #239 at thirty degrees incidence and observation in the specular direction. One data set has incident light s polarised and observed p-polarised, the other has incident light p-polarised and observed s-polarised.

As the mean light level is subtracted from each speckle image before any further processing, this ambient light is not expected to greatly affect the correlation values

to be obtained (in terms of invalidating any comparisons to theoretical results).

The large shift to higher values for surface #239, in the cross polarised case, may again be attributed to the ambient light level. The shift will be enhanced by the low intensity detected compared with the ambient light level. When considering the integration time of over 30 seconds and the large amount of light scattered around the laboratory which was not initially depolarised, it is surprising that the shift is not greater.

The departure from the general negative exponential shape of the histograms in figure 3.12 is not so easily explained. It is possible that it is due to a large amount of co-polarised light reflecting off of the polariser placed before the camera, and striking the surface again, producing (albeit with less magnitude) another cross polarised speckle pattern. The observed histogram would therefore be a combination of the two patterns, which would give, as seen earlier, a more Gaussian shape. The specular geometry of the experiments would support this hypothesis.

However, it must be borne in mind that the cross polarised results for surface #239 were taken near the practical limits of the equipment used: previous work with this surface (studying the average intensity in a given direction) reported no observed depolarisation^[41]. The experimental rig was not designed with a view to studying very low amounts of depolarisation. In future, the rig could be modified to cope with the above problem, allowing thorough scattering studies from surfaces such as surface #239 which only evidence slight multiply scattering.

3.2.3 Processing the Speckle Images

After having recorded and stored a range of speckle pattern images (the range could be images at incident angles separated by one degree — one image representing one particular alignment of incidence and observation), the data must be processed to obtain values for the correlations.

Correlation

The numerical method employed to obtain the correlation coefficient uses the convolution theorem. This method was chosen over a simple summation procedure as it gives the location of the best correlation, without presuming it is an exact overlay of the two images. An outline of the computational steps involved is given below:

1. Zero the mean and normalise one image (the reference image).
2. Perform a fast Fourier transform (FFT) on the reference image.
3. Find the complex conjugate of the transform.
4. Zero the mean and normalise another image (a data image).
5. FFT the data image.
6. Perform a pixel by pixel multiplication of this transform with the conjugated reference transform.
7. Find the inverse FFT of the above product.
8. Search for the peak in the correlation map just produced.

Normalisation is achieved by setting the sum of the value of all pixels squared to one ($\sum(x^2) = 1$).

This whole procedure results in just one number, the correlation coefficient between two speckle patterns at different angles. This number is in the range 0 to 1, 1 occurring when the reference is correlated with itself (identical) and 0 occurring when the two images have no similarities whatsoever. To obtain the curves presented later, a range of 'data' images must be correlated with a single 'reference' image; i.e., the above procedure must be repeated from step 4 until sufficient values at different angles have been procured. One set of speckle pattern images is enough to produce correlation curves for any reference angle within that set; only one experimental run is necessary.

Figure 3.13 shows two speckle patterns and their correlation map. Figure 3.14 is a trace through the centre of the correlation map, the height of the peak is the correlation coefficient (note that the width of the peak gives the speckle size in the autocorrelation case, i.e. when the speckle patterns are identical). The peak will not appear at the centre of the graph if the two speckle patterns have a relative shift.

The small fluctuations near the x -axis in this graph, indicating that small correlations exist at relatively large displacements of one speckle image with respect to the other, are an artifact of the finite size of the patterns correlated. If the correlated fields were infinitely large, these fluctuations would vanish leaving a smooth line along the axis. Notice that the height of the fluctuations reaches a maximum of about 0.05; this is the level of uncertainty expected from images, such as these,

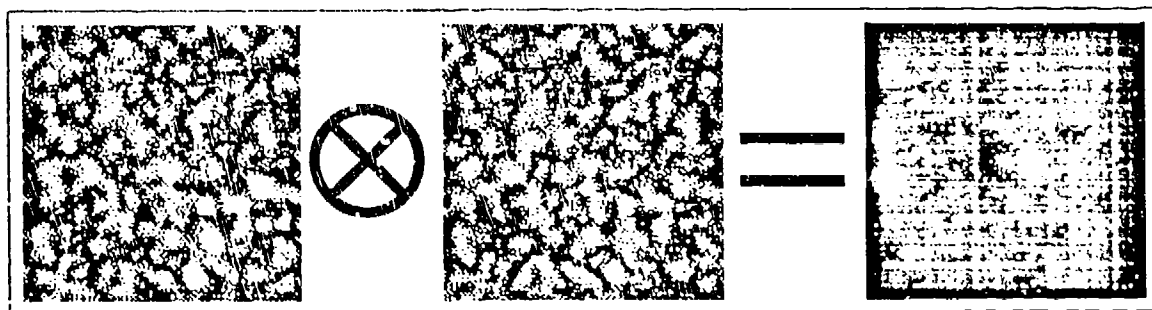


Figure 3.13: Obtaining the correlation coefficient of two speckle patterns. The cross-correlation of two normalised, zero mean speckle patterns giving the correlation map.

containing 400 speckles.

This minimum level of confidence will affect the correlation coefficient once it is reduced to that extent. It will mean that in later correlation curves, the minimum of the correlation coefficient will approach this level and not drop to zero as may be expected. Various methods have been employed to extract the correlation coefficient

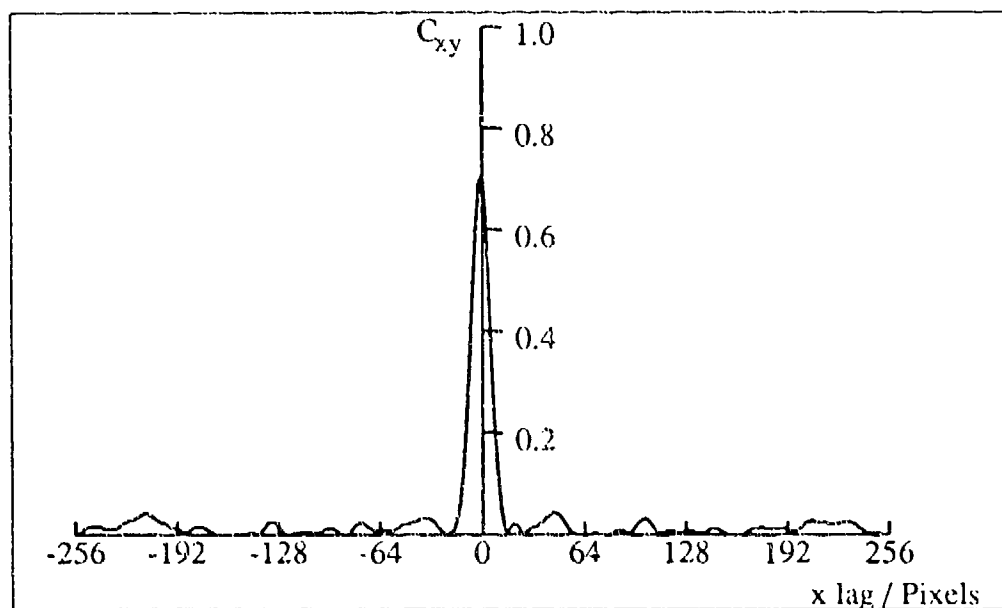


Figure 3.14: A slice along a horizontal line through the centre of the correlation map in figure 3.13. The peak of the curve is the correlation coefficient.

from the correlation maps created (see below), but the level at which the correlation is no longer meaningful is the same for all methods, the differences between them being purely cosmetic — i.e. some give more information below this level than others, but information in this region is unreliable.

Mean Intensity

As the relative intensities of the speckle patterns have been disturbed, it is not possible to derive an intensity plot by simply averaging the pixel values of each image. As any explanation of the correlations observed must also apply to the intensities, it was considered necessary to perform experiments to obtain the results under similar circumstances.

Unfortunately, previous intensity results obtained with (essentially) the equipment described below, on the same surfaces as studied in this work, were not considered with observation in the specular direction^{[11][41]}.

The illumination of the surface is by means identical to that used to obtain the correlation results. However, now a photomultiplier tube (PMT) is used to take the results instead of a CCD camera, this has a lens placed in front of it to collect the scattered light. The PMT is connected to a high tension power supply and its output is fed into a phase lock-in amplifier. The amplifier is connected to the ubiquitous PC which communicates with it via an IEEE interface. A beam chopper placed about half way along the beam is connected to the amplifier. The Sun workstation is no longer necessary in the chain.

3.2.4 Enhancements

Some experimental limitations on the accuracy of the correlations can be removed during processing, these will be discussed now.

Image Alignment

A problem noticed while sequentially displaying speckle images at high speed — always a good idea, to ensure that the data looks valid — was that as well as ‘evolving’ as expected, the whole pattern was slowly oscillating from side to side; this was possibly a problem with the stepper motors. The oscillation meant that any two speckle images would not overlap exactly. For the purposes of the correlation this is generally not a worry; however, if any processing is to be performed on the speckle images, misaligned patterns could pose a great problem.

The speckle patterns are aligned by performing a correlation, but instead of finding the value of the peak in the correlation map, the position of the peak within the map is determined. This gives the offset which must be applied to one image before it overlays the other — the whole image set is aligned in this way with the reference image, and a zero border is set around each image which absorbs the areas which do not overlap.

After having employed this technique it was found that correlation values increased slightly for the same set of data. Obviously some non-trivial degree of correlation must exist before this technique could work.

Pattern Shrinkage

If equation (3.5 in section 3.1.1) is expanded to depend on cartesian coordinates, such that there exists a τ_x and an orthogonal τ_y , then it can be seen that any increase in the beam width along the x direction, ω_x , would decrease τ_x whilst leaving τ_y unchanged. This situation occurs for increasing angles of incidence in the experimental work. As the surface is tilted to higher angles, so the laser beam spot elongates across the surface along the horizontal direction; this means that the speckle pattern will shrink horizontally (and also change to some extent) at increasing angles of incidence.

As the shrinkage is not accounted for in any theoretical studies later, two techniques were employed in an attempt to minimize its effect. The first involved placing a mask on the surface allowing only a certain area to be illuminated, regardless of the angle at which the light is incident. The second used 'tall, thin' images in the correlation procedure described above.

Figure 3.15 shows a comparison of experimental correlations taken from the same surface (#80), with and without a mask over it. As expected, the correlations at low angles are unaffected, but as the angle increases the correlation values from the surface with the mask over it are greatly increased. The improvement is lost at even higher angles as the mask introduces errors of its own as its finite thickness casts shadows onto the surface.

Since the mask increases the correlations in some circumstances (hence removes a source of error) and never reduces them, a mask will be placed on all surfaces to be experimentally studied.

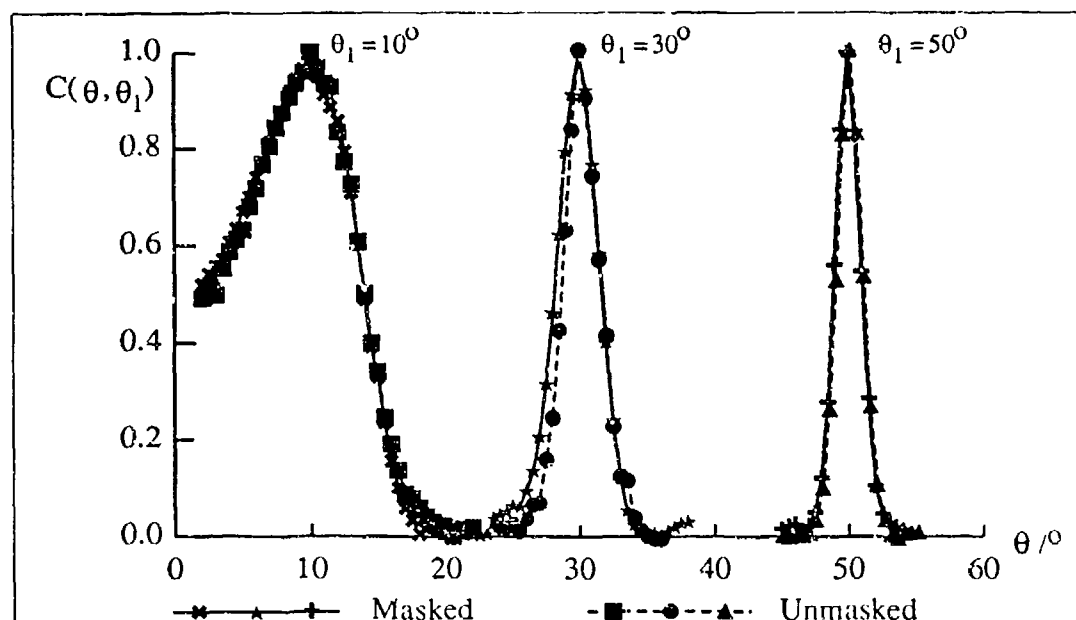


Figure 3.15: Graph showing the improvement in correlation values obtained at a given angle by masking a surface to reduce pattern shrinking. The solid line is the result from the surface masked, the dashed one unmasked. Note that the vertical distance between points shows a large enhancement.

For the other method, tall, thin images were obtained by truncating them in the x direction. The reasoning behind doing this is that the shrinking effect will displace speckles further away from the centre of the image by greater amounts: removing the speckles with large displacements will reduce a source of error in the correlations. One drawback with this method is that the number of speckles being processed is reduced, and hence the reliability of the results compromised.

Improving the Reliability of the Lower Value Correlations

As mentioned above, and seen in figure 3.13, there exists a limit below which, the 'true' correlation coefficient cannot be easily distinguished from small correlation fluctuations due to the finite size of the speckle images. The level of this limit,

however, can be reduced simply by knowing that the true correlation is near the centre. So, if the area of the correlation map, over which a maximum is searched for, is reduced to a small section around the centre, the maximum found is more likely to be the true correlation coefficient. It no longer needs to be the largest peak in the map.

A further improvement would be to have an aligned set of images, by a method such as that described above, and look only at the value at the center of the correlation map. However, in order to align the images some degree of correlation must exist, so it is not possible to know how to position those images, which, when correlated, produce a value below the limit. One possible way to overcome such a handicap is to keep a running total of the shift needed, and correlate each image with the previous one in its set; i.e. the shift needed to be imposed on the third image to align it with the first is the sum of the shifts needed to align the second to the first and the third to the second. This method, however, produced shifts which are inconsistent with those produced by a direct correlation. The most likely explanation being that by tracking the shift using a cumulative process, any errors will be cumulative, so within just a few images, the shift produced will be wrong. Since the shifts involved are only a few pixels and must be integer numbers of pixels, a fairly large rounding error will obviously exist.

Chapter 4

Single Scatter Analytical Study

4.1 The Single Scatter Approximation

In this section, the Kirchhoff approximation is applied to the Helmholtz-Kirchhoff integral to obtain a single scatter approximation of the far field amplitude of the scattered light. An analysis of the range of surface statistics that give a single scattering surface is also undertaken.

4.1.1 Derivation

The Kirchhoff approximation will be used to obtain an expressions for the single scatter component of the scattered amplitude in the far field by applying it to the Helmholtz-Kirchhoff integral (equation (2.48) from chapter two).

Following Beckmann^[16], an expression for the single scatter component of the scattered light in the far field is derived. The scattering geometry is shown (one dimensionally) in figure 4.1. Light is incident on a point \mathbf{r} with wave vector \mathbf{k}_i and

where \mathcal{R} is the Fresnel reflection coefficient at the point of scattering.

Combining equations (4.1 and 4.3) gives

$$E_s = \frac{1}{4\pi} \iint_S (1 + \mathcal{R}) E_i \frac{\partial \psi}{\partial \mathbf{n}} + (1 - \mathcal{R}) \psi \frac{\partial E_i}{\partial \mathbf{n}} dS \quad (4.4)$$

and by taking the incident field as a plane wave of amplitude E_0 ,

$$E_i = E_0 e^{i\mathbf{k}_i \cdot \mathbf{r}} \quad (4.5)$$

the normal derivative at the surface becomes

$$\frac{\partial E_i}{\partial \mathbf{n}} = i E_0 \mathbf{n} \cdot \mathbf{k}_i e^{i\mathbf{k}_i \cdot \mathbf{r}} \quad (4.6)$$

Now by taking the single scattered component of light out to the far field, \mathbf{R}_s can be written in terms of the absolute position of the observer in the far field, \mathbf{R}_0 ,

$$\mathbf{R}_s = \mathbf{R}_0 - \mathbf{r} \quad (4.7)$$

where now \mathbf{k}_0 and \mathbf{k}_s are identical. From equation (4.2),

$$\psi = \left(\frac{e^{ik_0 R_0}}{R_0} \right) e^{-i\mathbf{k}_s \cdot \mathbf{r}} \quad (4.8)$$

and

$$\frac{\partial \psi}{\partial \mathbf{n}} = -i \mathbf{n} \cdot \mathbf{k}_s \left(\frac{e^{ik_0 R_0}}{R_0} \right) e^{-i\mathbf{k}_s \cdot \mathbf{r}} \quad (4.9)$$

Finally, substituting these into equation (4.4), it becomes

$$E_s = \frac{E_0}{4\pi} \left(\frac{e^{ik_0 R_0}}{R_0} \right) \iint_S i \mathbf{n} \cdot [\mathcal{R}(\mathbf{k}_i - \mathbf{k}_s) - (\mathbf{k}_i + \mathbf{k}_s)] e^{i(\mathbf{k}_i - \mathbf{k}_s) \cdot \mathbf{r}} dS \quad (4.10)$$

representing the single scatter contribution to the scattered electric field, expressed in terms of the quantities in figure 4.1.

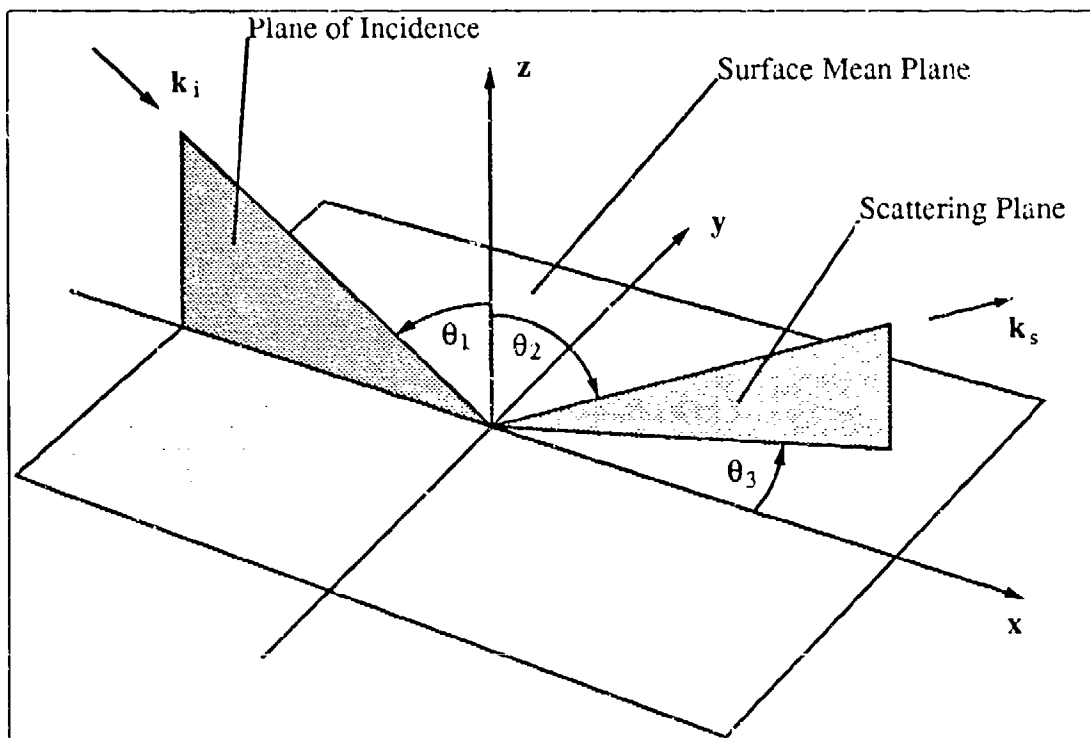


Figure 4.2: The general scattering geometry showing θ_1 , θ_2 and θ_3 .

Beckmann^[16] proceeds to develop a more approximate form of equation (4.10) for a random rough surface $\zeta(x, y)$ with sides of length $2L$ ($L \gg \lambda$) which removes the explicit reference to the surface normal. To distinguish this from the original form (equation (4.10)), the electric field E_s will be represented by the variable A . The single scattered amplitude in the far field may then be written, ignoring the small "edge" term, as:

$$A = \left(\frac{A_0 F_3}{(2L)^2} \right) \iint_{-L}^L e^{i\mathbf{V} \cdot \mathbf{r}} dx dy \quad (4.11)$$

where $\mathbf{V} = \mathbf{k}_i - \mathbf{k}_s$, F_3 is a geometrical factor and A_0 is the field which would be reflected in the specular direction by p-polarised incident light if the surface were a perfectly conducting smooth plane.

Expanding \mathbf{r} and \mathbf{V} into cartesian components, and applying the geometry shown

in figure 4.2,

$$A(\theta_1, \theta_2, \theta_3) = \left(\frac{A_0 F_3}{(2L)^2} \right) \iint_{-L}^L e^{i(V_x x + V_y y + V_z z)} dx dy \quad (4.12)$$

where

$$\begin{aligned} V_x &= \frac{2\pi}{\lambda} (\sin \theta_1 - \sin \theta_2 \cos \theta_3) \\ V_y &= \frac{2\pi}{\lambda} (\sin \theta_2 \sin \theta_3) \\ V_z &= \frac{2\pi}{\lambda} (\cos \theta_1 + \cos \theta_2) \end{aligned} \quad (4.13)$$

Both F_3 and A_0 are also functions of θ_1, θ_2 and θ_3 .

4.1.2 Validity of the Single Scatter Model

A similar method to that employed to estimate the Kirchhoff validity will be used here to obtain an estimate of which Gaussian surfaces are smooth enough to be considered as single scatterers.

An intuitive assumption will be made, that double scattering first comes into play (with changing angle) when the path of the light between two scattering points is in a plane parallel to the mean surface plane. This condition can be seen in figure 4.3. The reasoning behind this assumption being that a surface which is not rough enough to have any gradients complying with this condition, will not only scatter the light away from itself, but will have a comparatively large distance between any two sides of a 'valley'. This will make it almost impossible for light which is propagating with a gradient greater than zero to strike the surface again. The technique does not cater for any diffraction effect which will occur as the distance between the sides of a valley approaches a wavelength.

Following the assumption, the surface gradient at the point of scattering must be

$$m = \tan(\pi/4 - |\theta|/2) \quad (4.14)$$

where θ is the angle of incidence of the light.

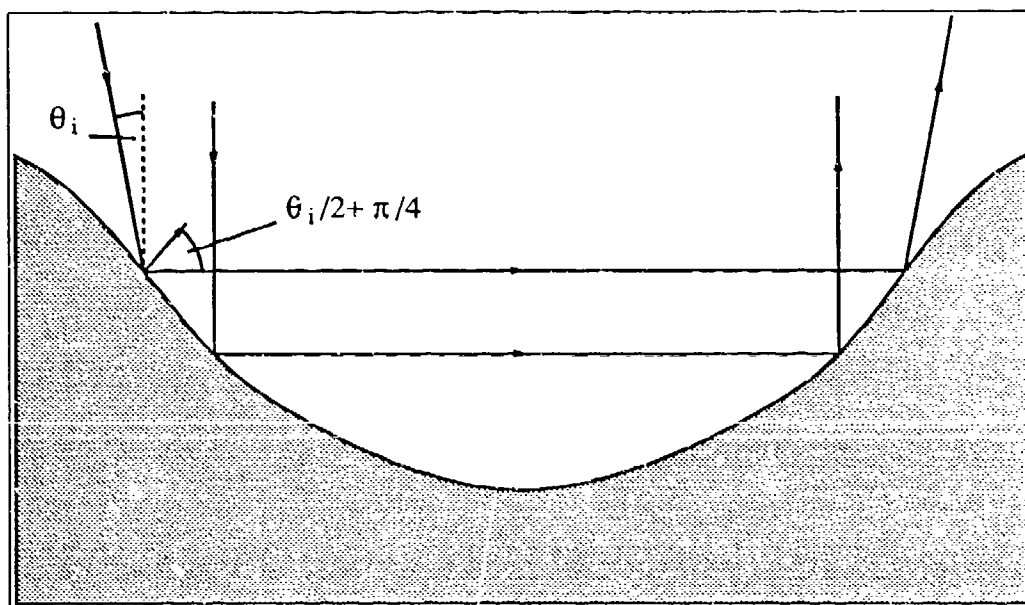


Figure 4.3: The condition required before double scattering is evident.

As this is a limit, it is possible to say that the surface will be a single scattering one if the vast majority of its surface gradients are less than m in magnitude. Since the surfaces studied here are Gaussian, the surface gradients themselves have a Gaussian distribution with zero mean and standard deviation

$$\sigma_{S'} = \frac{\sqrt{2}\sigma}{\tau} \quad (4.15)$$

(cf. chapter two). As previously determined, 99.7% of a Gaussian quantity lies within three standard deviations of the mean. The condition may, therefore, be written

$$\frac{3\sqrt{2}\sigma}{\tau} < \tan(\pi/4 - |\theta|/2) \quad (4.16)$$

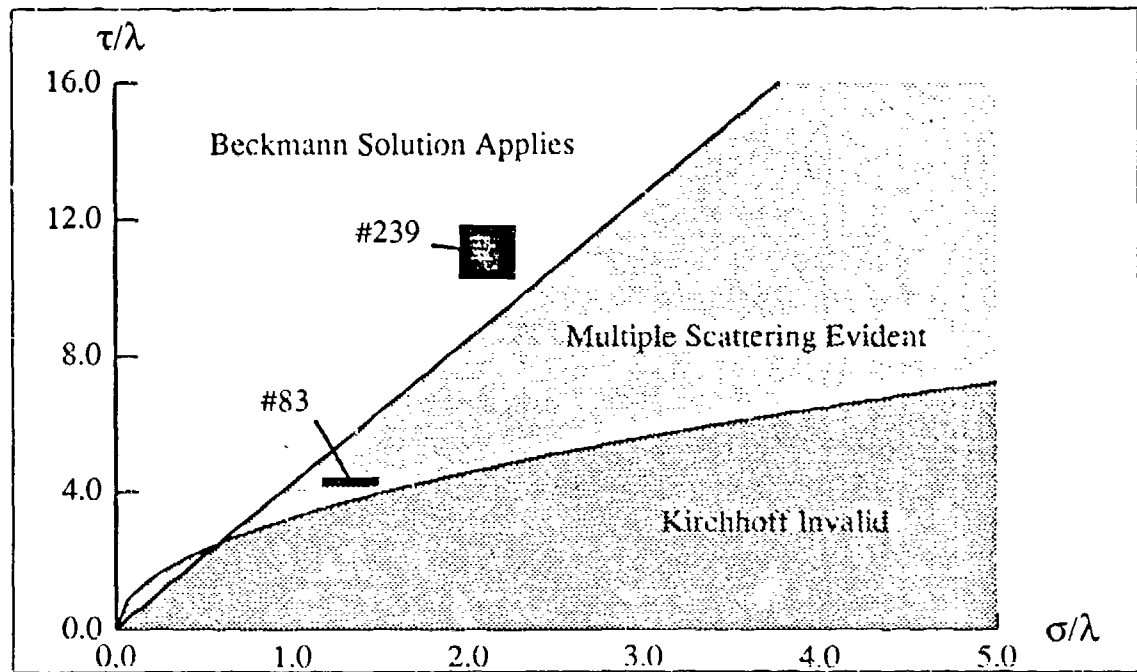


Figure 4.4: Surface parameters for which the single scatter Kirchhoff approximation (Beckmann solution) is valid. Boundaries are placed at the three standard deviation threshold. The surfaces are plotted with the wavelength at $\lambda = 0.633\mu m$ and for normal incidence. Surface #80 (not shown) lies well within the region in which the Beckmann solution applies.

where 99.7% of the surface gradients are within the limit.

Figure 4.4 is a graph of equation (4.16), for normal incidence, with the Kirchhoff approximation validity graph overlayed. The limit of the joint region of applicability (the white area) is roughly the same shape as and within the one percent unitarity error limit found for the region of validity of the single scatter Kirchhoff theory by numerical simulation^[3] (for all angles of incidence). The close agreement between the results derived from the statistical propositions about when the limits of the Kirchhoff approximation and single scattering will occur and the numerical results lends a great deal of weight to the simple mechanism. An explanation of the double scatter results shown in later chapters will be developed on the basis of this

argument.

The graph also shows that the Kirchhoff approximation is more widely applicable than the single scatter approximation; this fact will be exploited in chapter five. Under an illuminating wavelength of $0.633\mu m$, surface #83 is in the region of Kirchhoff applicability, but not single scattering, whereas surface #239 lies just inside the single scatter limit. Bearing in mind that the single scatter boundary line was plotted for normal incidence, at more oblique angles a surface might cross the boundary and become multiply scattering — in fact, the limit of equation (4.16) is achieved, for surface #239, at an angle of incidence of 6.0 ± 4.0 degrees from normal (the large uncertainty due to the errors in σ and τ).

4.2 Correlation Coefficient of Two Speckle Patterns

This next derivation follows, to some extent, the work performed by Legér and Perrin^[31], the starting point being the single scattered field, equation (4.12).

The amplitude correlation coefficient of two such fields $A_1(\theta_1, \theta_2, \theta_3)$ and $A_2(\phi_1, \phi_2, \phi_3)$ is

$$C_A = \frac{\langle A_1 A_2^* \rangle}{\sqrt{\langle A_1 A_1^* \rangle \langle A_2 A_2^* \rangle}} \quad (4.17)$$

First the general correlation of the fields $\langle A_1 A_2^* \rangle$ must be found:

$$\begin{aligned} \langle A_1 A_2^* \rangle &= \left\langle \frac{A_{01} F_{31} A_{02} F_{32}}{(2L)^4} \iiint \int_{-L}^L e^{i(V_{x1}x_1 - V_{x2}x_2 + V_{y1}y_1 - V_{y2}y_2 + V_{z1}\zeta_1 - V_{z2}\zeta_2)} dx_1 dx_2 dy_1 dy_2 \right\rangle \end{aligned} \quad (4.18)$$

$$= \frac{A_{01}F_{31}A_{02}F_{32}}{(2L)^4} \iiint_{-L}^L e^{i(V_{x1}x_1 - V_{x2}x_2)} e^{i(V_{y1}y_1 - V_{y2}y_2)} \langle e^{i(V_{z1}\zeta_1 - V_{z2}\zeta_2)} \rangle dx_1 dx_2 dy_1 dy_2$$

where V_x , V_y and V_z are as in equations (4.13) and where subscript 1 indicates dependence on angles θ_1 , θ_2 and θ_3 , one of the required arrangements, and subscript 2 on angles ϕ_1 , ϕ_2 and ϕ_3 , the other arrangement necessary.

As mentioned in chapter two, the surfaces to be examined here may be represented as a zero mean Gaussian process and a Gaussian correlation function. Using the result for any zero mean Gaussian process η ,

$$\langle e^{i\alpha\eta} \rangle = e^{-\frac{1}{2}\alpha^2\langle\eta^2\rangle} \quad (4.19)$$

then

$$\langle e^{i(V_{z1}\zeta_1 - V_{z2}\zeta_2)} \rangle = e^{-\frac{1}{2}\sigma^2[V_{z1}^2 + V_{z2}^2 - 2V_{z1}V_{z2}C_\zeta(x_1, x_2, y_1, y_2)]} \quad (4.20)$$

where $\sigma^2 = \langle\zeta^2\rangle$ is the mean square surface height (the variance of ζ), and

$$C_\zeta(x_1, x_2, y_1, y_2) = \exp\left(-\frac{(x_1 - x_2)^2 + (y_1 - y_2)^2}{\tau^2}\right) \quad (4.21)$$

is the Gaussian autocorrelation function for the surface, correlation length τ .

For large τ ,

$$C_\zeta(x_1, x_2, y_1, y_2) \approx 1 - \frac{(x_1 - x_2)^2 + (y_1 - y_2)^2}{\tau^2} \quad (4.22)$$

a parabolic approximation which is more generally applicable than the case presented here — implying that this theory may also apply to surfaces which have correlation functions that are not Gaussian.

Putting equations (4.20 and 4.22 into equation 4.18) gives

$$\langle A_1 A_2^* \rangle = \frac{A_{01}F_{31}A_{02}F_{32}}{(2L)^4} e^{-\frac{1}{2}\sigma^2(V_{z1} - V_{z2})^2} \quad (4.23)$$

$$\begin{aligned}
& \times \int_{-L}^L \int_{-L}^L e^{i(V_{x_1}x_1 - V_{x_2}x_2)} e^{-\frac{\sigma^2 V_{x_1} V_{x_2}}{\tau^2} (x_1 - x_2)^2} dx_1 dx_2 \\
& \times \int_{-L}^L \int_{-L}^L e^{i(V_{y_1}y_1 - V_{y_2}y_2)} e^{-\frac{\sigma^2 V_{y_1} V_{y_2}}{\tau^2} (y_1 - y_2)^2} dy_1 dy_2
\end{aligned}$$

By applying the variable changes $t_x = x_1 - x_2$, $t_y = y_1 - y_2$, $s_x = x_1 + x_2$ and $s_y = y_1 + y_2$ then $dx_1 dx_2$ becomes $\frac{1}{2} ds_x dt_x$ and $dy_1 dy_2 = \frac{1}{2} ds_y dt_y$, so,

$$\begin{aligned}
\langle A_1 A_2^* \rangle &= \frac{A_{0_1} F_{3_1} A_{0_2} F_{3_2}}{4(2L)^4} e^{-\frac{1}{2}\sigma^2(V_{x_1} - V_{x_2})^2} \quad (4.24) \\
&\times \int_{-\sqrt{2}L}^{\sqrt{2}L} e^{i(V_{x_1} - V_{x_2})\frac{s_x}{2}} \left(\int_{-\sqrt{2}L}^{\sqrt{2}L} \exp \left[\frac{-\sigma^2 V_{x_1} V_{x_2}}{\tau^2} t_x^2 + i(V_{x_1} + V_{x_2})\frac{t_x}{2} \right] dt_x \right) ds_x \\
&\times \int_{-\sqrt{2}L}^{\sqrt{2}L} e^{i(V_{y_1} - V_{y_2})\frac{s_y}{2}} \left(\int_{-\sqrt{2}L}^{\sqrt{2}L} \exp \left[\frac{-\sigma^2 V_{y_1} V_{y_2}}{\tau^2} t_y^2 + i(V_{y_1} + V_{y_2})\frac{t_y}{2} \right] dt_y \right) ds_y
\end{aligned}$$

Notice that if x_1 and x_2 are independent, as is the case above, they will form an orthogonal coordinate system. Within this system, any lines of constant t_x will be seen to be orthogonal to lines of constant s_x , implying that s_x and t_x are independent. The same argument may be used to show t_y and s_y are independent. Note that the variable transformation used at this stage in reference[31] was not orthogonal.

For large a , as is the case in equation (4.24),

$$\int_{-X}^X e^{-av^2} e^{ibv} dv \approx \int_{-\infty}^{\infty} e^{-av^2} e^{ibv} dv \quad (4.25)$$

Using the result for $a > 0$,

$$\int_{-\infty}^{\infty} e^{-av^2} e^{ibv} dv = \sqrt{\frac{\pi}{a}} \exp \left[\frac{-b^2}{4a} \right] \quad (4.26)$$

gives

$$\begin{aligned}
\langle A_1 A_2^* \rangle &= \frac{A_{0_1} F_{3_1} A_{0_2} F_{3_2}}{4(2L)^4} e^{-\frac{1}{2}\sigma^2(V_{x_1} - V_{x_2})^2} \\
&\times \int_{-\sqrt{2}L}^{\sqrt{2}L} e^{i(V_{x_1} - V_{x_2})\frac{s_x}{2}} ds_x \sqrt{\frac{\pi \tau^2}{\sigma^2 V_{x_1} V_{x_2}}} \exp \left[-\frac{(V_{x_1} + V_{x_2})^2 \tau^2}{16 \sigma^2 V_{x_1} V_{x_2}} \right] \\
&\times \int_{-\sqrt{2}L}^{\sqrt{2}L} e^{i(V_{y_1} - V_{y_2})\frac{s_y}{2}} ds_y \sqrt{\frac{\pi \tau^2}{\sigma^2 V_{y_1} V_{y_2}}} \exp \left[-\frac{(V_{y_1} + V_{y_2})^2 \tau^2}{16 \sigma^2 V_{y_1} V_{y_2}} \right] \quad (4.27)
\end{aligned}$$

Now substituting the simple result for the remaining integrals

$$\int_{-X}^X e^{iau} du = 2X \operatorname{sinc}(aX) \quad (4.28)$$

into equation (4.27) yields

$$\begin{aligned} \langle A_1 A_2^* \rangle &= \frac{A_{01} F_{31} A_{02} F_{32}}{8L^2} e^{-\frac{1}{2}\sigma^2(V_{z1}-V_{z2})^2} \operatorname{sinc} \left[\frac{\sqrt{2}}{2}(V_{x1}-V_{x2})L \right] \\ &\times \operatorname{sinc} \left[\frac{\sqrt{2}}{2}(V_{y1}-V_{y2})L \right] \frac{\pi \tau^2}{\sigma^2 V_{z1} V_{z2}} \exp \left[-\frac{((V_{x1}+V_{x2})^2 + (V_{y1}+V_{y2})^2) \tau^2}{16\sigma^2 V_{z1} V_{z2}} \right] \end{aligned} \quad (4.29)$$

Normalising as in equation (4.17), the amplitude correlation coefficient of two speckle patterns is

$$\begin{aligned} C_A &= e^{-\frac{1}{2}\sigma^2(V_{z1}-V_{z2})^2} \operatorname{sinc} \left[\frac{\sqrt{2}}{2}(V_{x1}-V_{x2})L \right] \operatorname{sinc} \left[\frac{\sqrt{2}}{2}(V_{y1}-V_{y2})L \right] \\ &\times \exp \left[\frac{\tau^2}{16\sigma^2} \left(2 \frac{V_{x1}^2 + V_{y1}^2}{V_{z1}^2} + 2 \frac{V_{x2}^2 + V_{y2}^2}{V_{z2}^2} - \frac{(V_{x1}+V_{x2})^2 + (V_{y1}+V_{y2})^2}{V_{z1} V_{z2}} \right) \right] \end{aligned} \quad (4.30)$$

Equation (4.30) is a general result for the two-dimensional amplitude correlation coefficient; however, the quantity sought here is an intensity correlation, the amplitude correlation is not relevant to this work. Assuming that the speckle amplitude is a complex Gaussian process, the following relation holds^[45]:

$$\langle \Delta I_1 \Delta I_2 \rangle = |\langle A_1 A_2^* \rangle|^2 \quad (4.31)$$

This leads to a simple relationship between the correlation coefficient of the intensity fluctuations and the amplitude correlation coefficient^[38]

$$C_I = |C_A|^2 \quad (4.32)$$

Finally, the two-dimensional intensity correlation coefficient is

$$C_I(\theta_1, \theta_2, \theta_3, \phi_1, \phi_2, \phi_3) = e^{-\sigma^2(V_{z1}-V_{z2})^2} \quad (4.33)$$

$$\times \text{sinc}^2 \left[\frac{\sqrt{2}}{2} (V_{x_1} - V_{x_2}) L \right] \text{sinc}^2 \left[\frac{\sqrt{2}}{2} (V_{y_1} - V_{y_2}) L \right] \\ \times \exp \left[\frac{\tau^2}{8\sigma^2} \left(2 \frac{V_{x_1}^2 + V_{y_1}^2}{V_{z_1}^2} + 2 \frac{V_{x_2}^2 + V_{y_2}^2}{V_{z_2}^2} - \frac{(V_{x_1} + V_{x_2})^2 + (V_{y_1} + V_{y_2})^2}{V_{z_1} V_{z_2}} \right) \right]$$

4.2.1 Consequences of the Intensity Correlation

It can be seen from equation (4.33), that the correlation coefficient will have its maximum when $V_{x_1} = V_{x_2}$, $V_{y_1} = V_{y_2}$ and $V_{z_1} = V_{z_2}$, i.e., when the two arrangements of observation and illumination are identical. It may also be seen that there are various factors which vary with only one of V_x , V_y or V_z , and that some of these factors may be removed purely by geometric considerations.

The most obvious limitation to impose upon equation (4.33) is to only allow 'in plane' scattering in both arrangements, i.e., set $\theta_3 = \phi_3 = 0$, which from equations (4.13) means that $V_{y_1} = V_{y_2} = 0$. The intensity correlation becomes:

$$C_I(\theta_1, \theta_2, \phi_1, \phi_2) = \exp \left[-\sigma^2 (V_{z_1} - V_{z_2})^2 \right] \text{sinc}^2 \left[\frac{\sqrt{2}}{2} (V_{x_1} - V_{x_2}) L \right] \\ \times \exp \left[\frac{\tau^2}{8\sigma^2} \left(2 \frac{V_{x_1}^2}{V_{z_1}^2} + 2 \frac{V_{x_2}^2}{V_{z_2}^2} - \frac{(V_{x_1} + V_{x_2})^2}{V_{z_1} V_{z_2}} \right) \right] \quad (4.34)$$

It now makes sense to force the same step for the V_x 's and set $V_{x_1} = V_{x_2} = 0$. From equations (4.13) it can be seen that this is easily achieved, namely by setting $\theta_1 = \theta_2$ and $\phi_1 = \phi_2$. This corresponds to observation always in the specular direction. If $\phi_1 = \phi_2 = \theta_1 + \delta\theta$, the intensity correlation coefficient between two speckle patterns observed in the specular direction with illumination angles θ_1 and $\theta_1 + \delta\theta$ is

$$C_I(\theta_1, \delta\theta) = \exp \left[- \left(\frac{4\pi\sigma}{\lambda} \right)^2 (\cos \theta_1 - \cos(\theta_1 + \delta\theta))^2 \right] \quad (4.35)$$

Note that the correlation no longer depends on the correlation length of the surface, τ .

A similar result might be expected if $V_{x_1} = V_{x_2} = c$, where c is non-zero. From equations (4.13), this means that there will be a maximum in the correlation, (although it is not possible to separate out the V_z dependence) when

$$\sin \theta_1 - \sin \theta_2 = \sin \phi_1 - \sin \phi_2 \quad (4.36)$$

This condition has been reported by Michel^[33] for rough surfaces, although it was presented earlier in another form by Legér and Perrin^[31] (cf. "memory effect" in chapter one). It is always true for the specular case.

Figures 4.5 to 4.7 examine a few of the possibilities equation (4.36) offers; each figure consists of a correlation graph produced with equation (4.34), and an associated graph showing the angles θ_1 , θ_2 , ϕ_1 and ϕ_2 . In all cases θ_1 and θ_2 are fixed and ϕ_1 is the controlled parameter; knowing these three angles, ϕ_2 is determined with equation (4.36).

The first of the figures, figure 4.5, shows the specular case, $\theta_2 = \theta_1$ and $\phi_2 = \phi_1$, the reference being at $\theta_1 = 10$ degrees; the shape of the curve is that given by equation (4.35).

Figure 4.6 shows the case where θ_1 and θ_2 are fixed at 10 degrees and 0 degrees respectively, ϕ_2 is determined, for a particular ϕ_1 , by equation (4.36). As may be expected from consideration of the $V_{z_1} - V_{z_2}$ term,

$$(\cos \theta_1 + \cos \theta_2) - (\cos \phi_1 + \cos \phi_2) \quad (4.37)$$

the correlation drops off at a slower rate than in the specular case shown in figure 4.5.

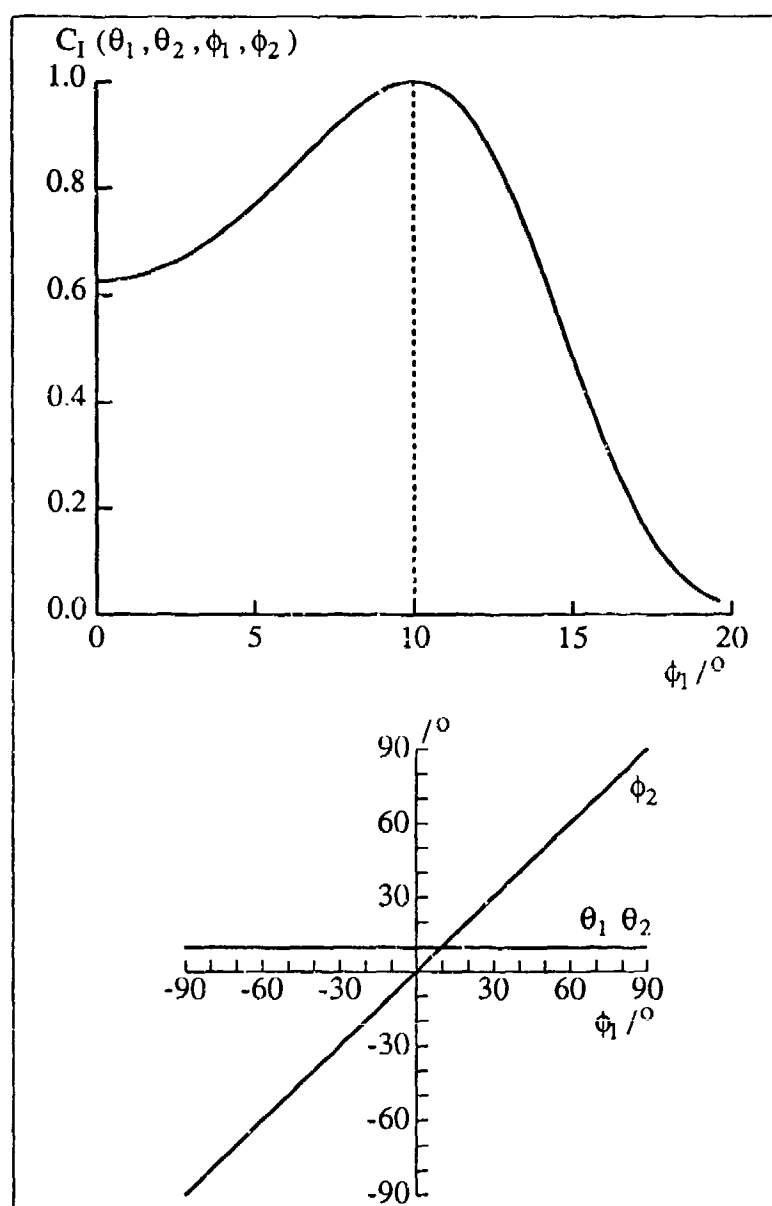


Figure 4.5: Top: $C_I(\theta_1, \theta_2, \phi_1, \phi_2)$ plotted for the specular case with the reference at 10 degrees ($\theta_2 = \theta_1 = 10$).

Bottom: ϕ_2 is determined by equation (4.36), in this case $\phi_2 = \phi_1$.

The last figure, figure 4.7, shows the case where the reference image is in back-scatter, i.e., $\theta_2 = -\theta_1$; ϕ_2 is given, for a particular ϕ_1 , by equation (4.36). For

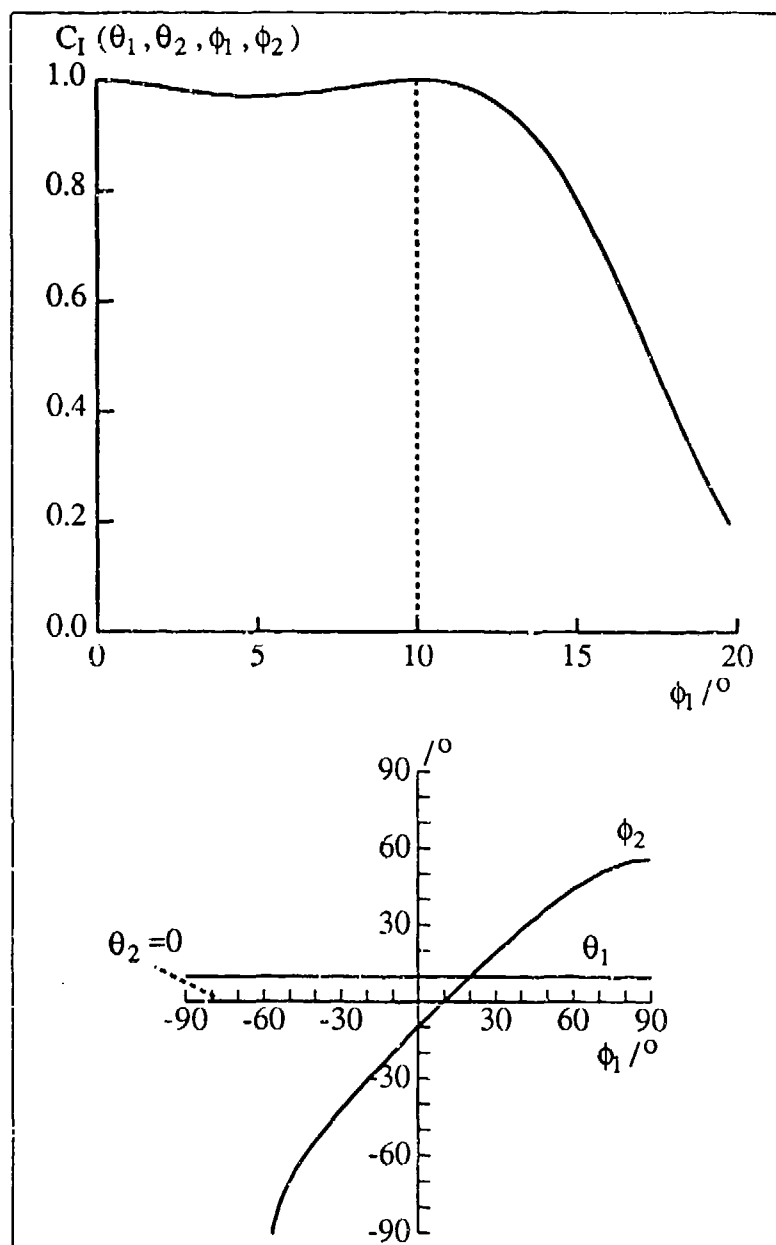


Figure 4.6: Top: $C_I(\theta_1, \theta_2, \phi_1, \phi_2)$ plotted with the reference at $\theta_1 = 10$ degrees, and $\theta_2 = 0$.

Bottom: ϕ_2 is determined by satisfying equation (4.36).

$\theta_1 = 10$ degrees, V_{z_1} ,

$$\cos \theta_1 + \cos \theta_2 \quad (4.38)$$

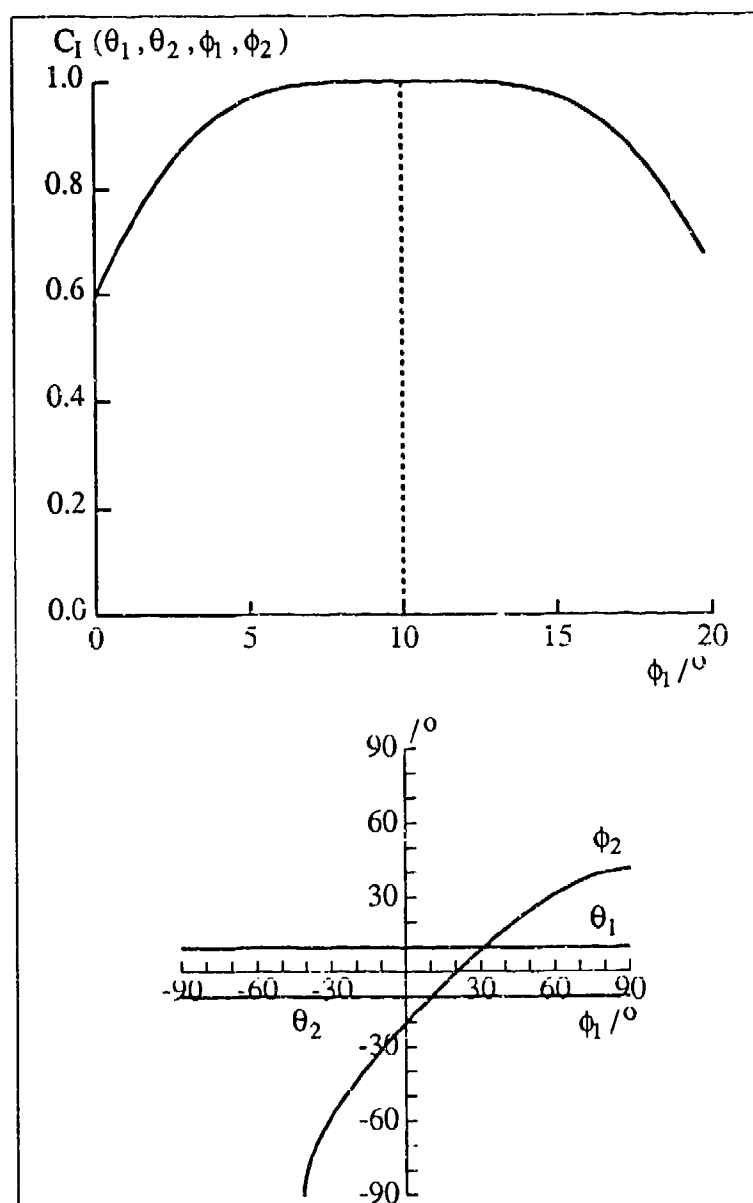


Figure 4.7: Top: $C_I(\theta_1, \theta_2, \phi_1, \phi_2)$ plotted for the reference in back-scatter ($\theta_1 = 10$ degrees and $\theta_2 = -10$ degrees).

Bottom: ϕ_2 is determined by satisfying equation (4.36).

is identical to the that for the specular case, but now the variation in V_{z_2} ,

$$\cos \phi_1 + \cos \phi_2 \quad (4.39)$$

is even slower.

These results are extremely counter intuitive. As discussed in chapter one, the highest degree of correlation might be expected in the specular arrangement. However, the slower decorrelations, arising because of the slower variations in the V_z terms, may be understood by considering the paths the light travels in each case. For the last case presented, where the reference is in the back-scatter direction, the angles between the various paths are small and, since it is the angular difference which counts, will therefore introduce less of an angular decorrelation than in the other cases, where the angles between the paths are greater (being largest in the specular case).

In plainer terms, the directions of incidence and observation are all very similar in the back-scatter case. Changing these will obviously affect the degree of similarity, but not to a major extent. Compare that to where observation is in the specular direction — the directions are not even similar in the first place, and any change makes a large difference.

4.2.2 Comparison with Experimental Results

Figure 4.8 is a plot of equation (4.35) with $\theta_1 = 10$ degrees, which applies to correlations taken at points, compared with experimental results, which necessarily involve spatial averaging with the equipment used. It shows that the experimental correlations are a lot lower than the theory predicts. The error on each point is predicted to be around $\pm 5\%$, being the statistical uncertainty on a sample of 400 speckles, $1/\sqrt{(400)}$.

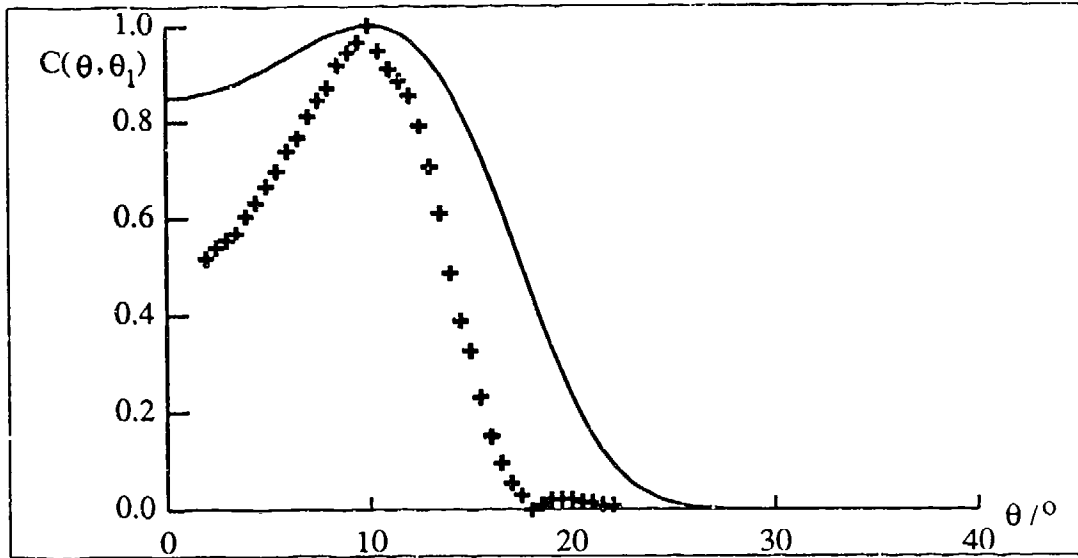


Figure 4.8: Equation (4.35) (solid line) plotted with experimental correlations (+'s) taken from surface #80 with incident light at 10 degrees and s-polarised and observed speckle patterns in the specular direction — also s-polarised. The wavelength, $\lambda = 0.633\mu\text{m}$. The error on each point is $\pm 5\%$.

One major difference between the theoretical analysis and the experimental approach is that equation (4.35) produces the correlation coefficient at a point, whereas the experimental situation necessarily deals with the correlation of an area the size of the camera's CCD array.

To cope with this, it is necessary to abandon equation (4.35) and turn back to equation (4.33). As this equation provides for scattering away from the specular direction and out of plane scattering, it is possible to find the correlation coefficient at any point in space, not just at the point in the specular direction. By averaging equation (4.33) over the area of the CCD array, a result similar to the experimental observations should be obtained.

No attempt has been made to average equation (4.33) analytically. For the results to be shown later, the equation was evaluated for each pixel in the CCD array

contributing to the portion of the speckle pattern used to obtain an experimental result. An average of all evaluations gives the correlation coefficient to be compared to experiment.

Figure 4.9 shows the relationship between the coordinates of a point on the CCD array, (p, q) , and the angles used in equation (4.33). This relationship is explicitly stated as equations (4.40).

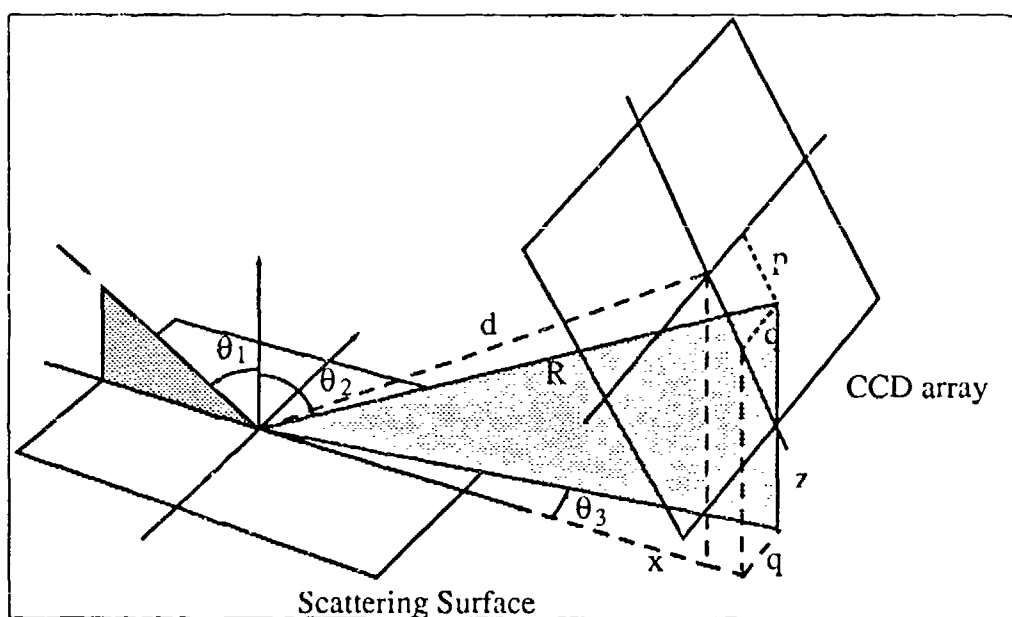


Figure 4.9: Diagram showing the relationship between a point on the CCD array and the angles θ_1, θ_2 and θ_3 . Note that the centre of the CCD array subtends an angle of θ_1 to the mean surface normal.

$$\begin{aligned}\cos \theta_2 &= \frac{z}{R} \\ \sin \theta_3 &= \frac{q}{x}\end{aligned}\tag{4.40}$$

where

$$x = d \sin \theta_1 + p \cos \theta_1$$

$$z = d \cos \theta_1 - p \sin \theta_1$$

$$R = \sqrt{x^2 + q^2 + z^2}$$

The numerically averaged result is compared against experiment in figure 4.10. This graph is identical to figure 4.8 in all other respects. It can be seen that by averaging equation (4.33) a result very close to the experimental observation is obtained.

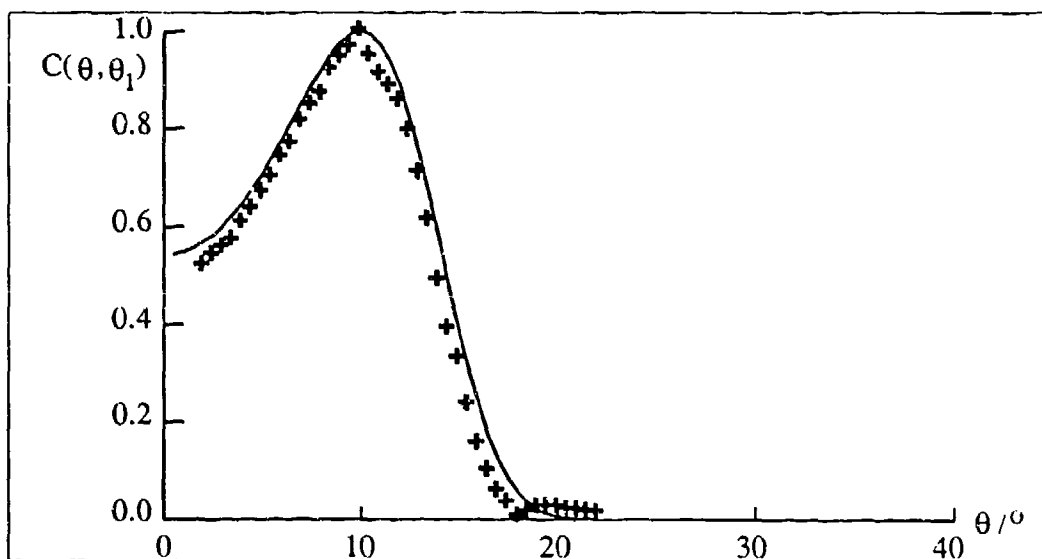


Figure 4.10: Equation (4.33) averaged over the area of the CCD element (solid line) plotted with experimental correlations (+'s) taken from surface #80 with the reference at 10 degrees, incidence light is s-polarised and observed speckle patterns in the specular direction are also s-polarised. $\lambda = 0.633\mu m$.

Having now determined that it is necessary to average equation (4.33) to gain a similarity with experiment, it is desirable to examine the effect this has on the various arrangements discussed above and graphed in figures 4.5 to 4.7.

Figures 4.11 to 4.13 are the equivalents of the above mentioned graphs but now using equation (4.33) averaged over an area around the observed direction.

As expected for the specular case, the correlation at any point is generally less

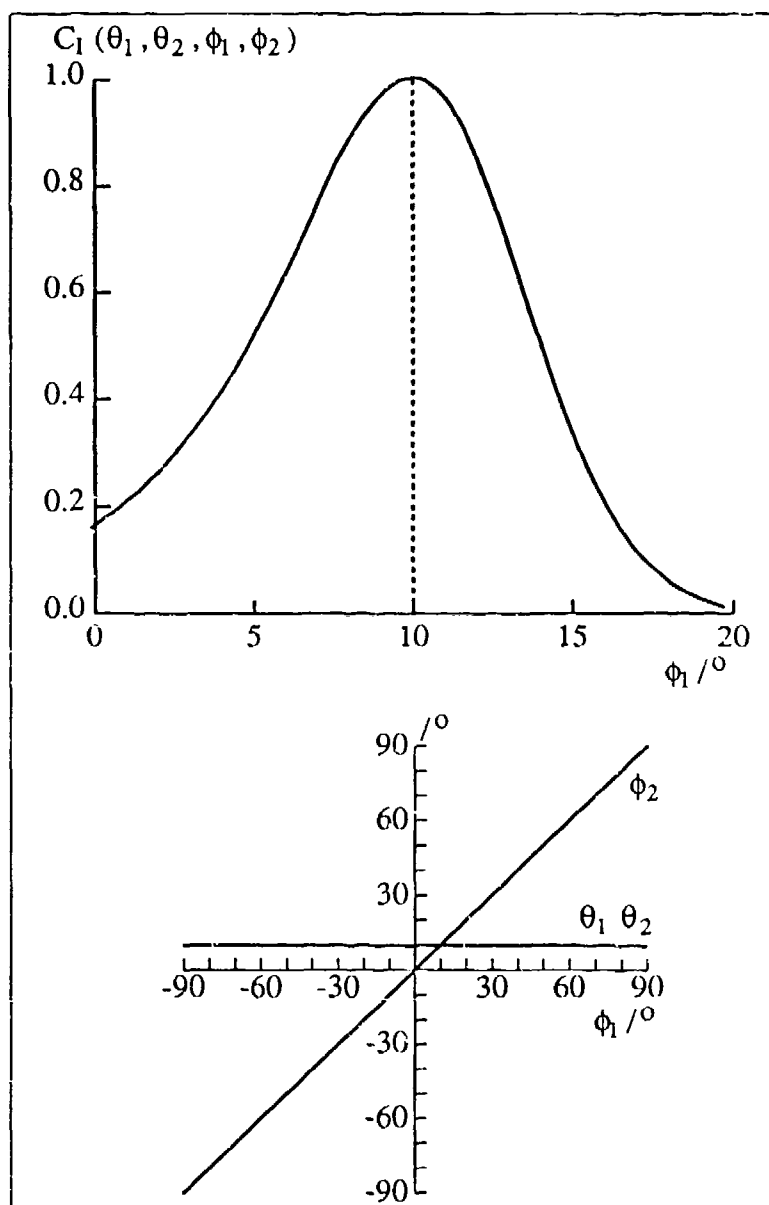


Figure 4.11: $C_I(\theta_1, \theta_2, \phi_1, \phi_2)$ (averaged) plotted for the specular case with the reference at 10 degrees and all angles satisfying equation (4.36).

than in the unaveraged situation. For the back-scatter and fixed reference case, the correlation coefficient is zero apart from at the point where the two angular arrangements are the same, where it is one. The resolution of this curve is one point

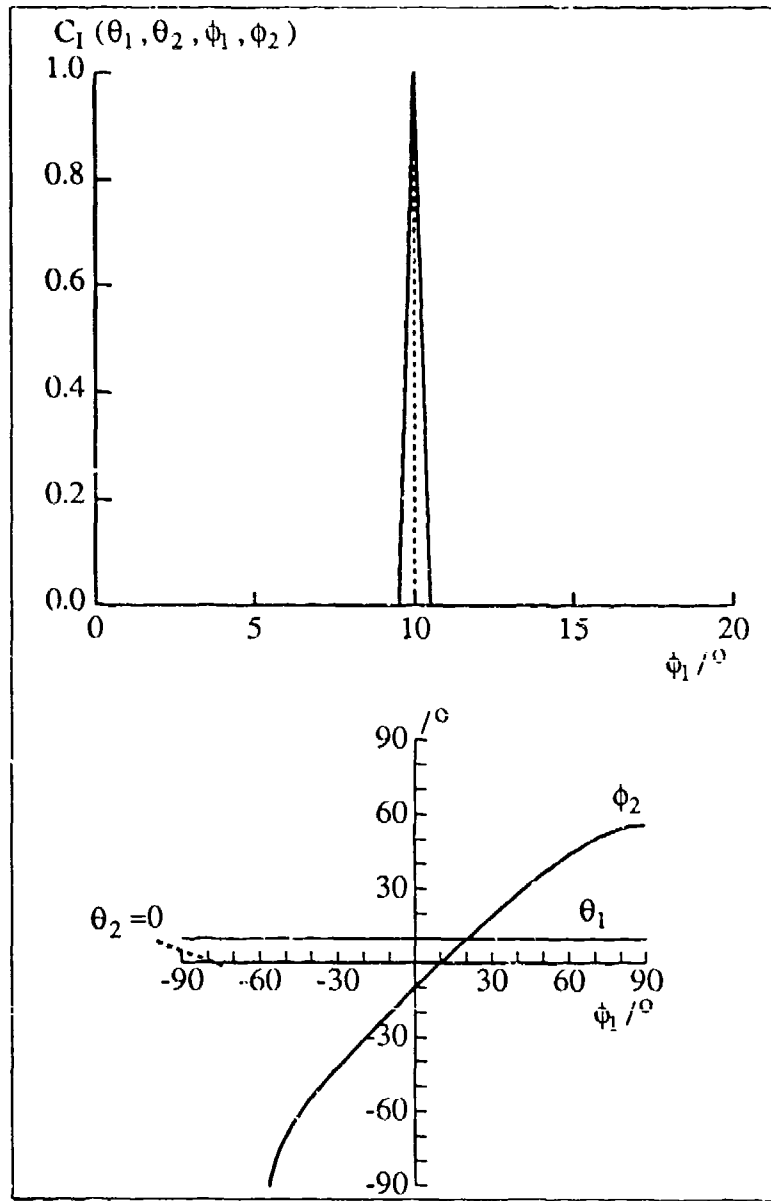


Figure 4.12: $C_I(\theta_1, \theta_2, \phi_1, \phi_2)$ (averaged) plotted with the reference at $\theta_1 = 10$ degrees, and $\theta_2 = 0$. All angles satisfy equation (4.36).

every half a degree — if a finer resolution were used the spike might be expected to have an angular width about that of a speckle.

The reason for the reduction in the correlations is that the terms in equation (4.33)

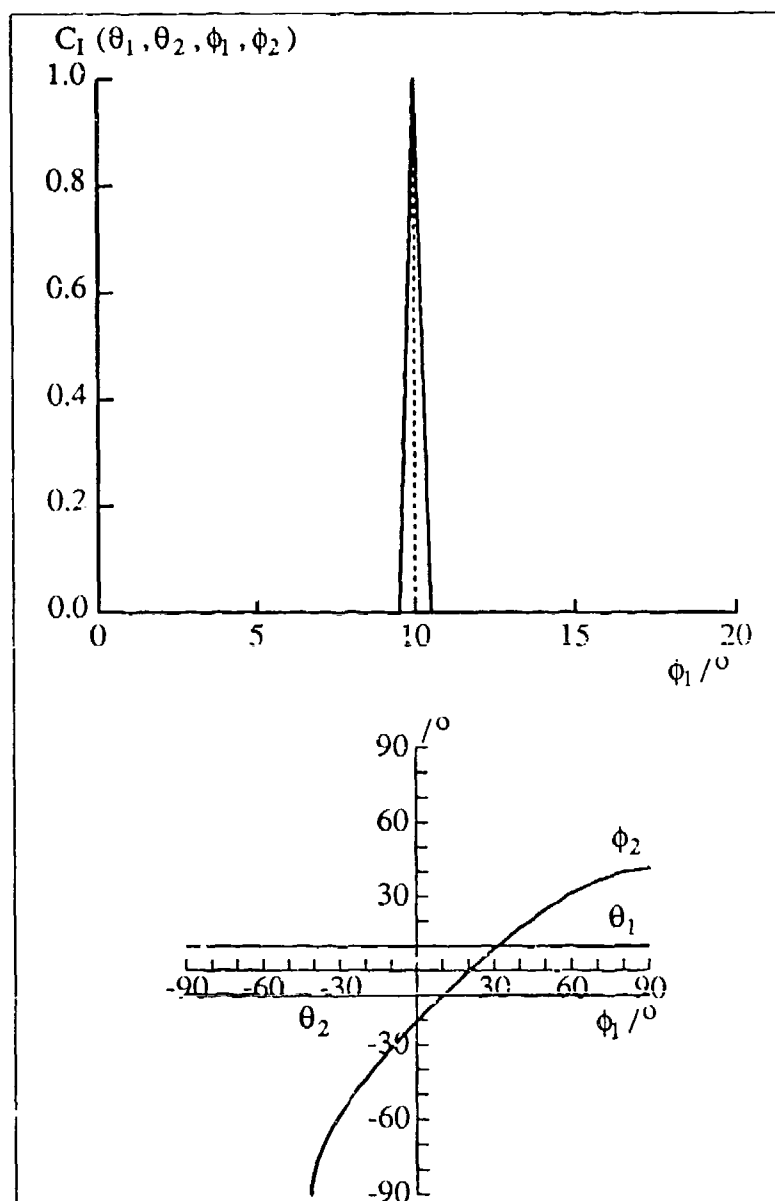


Figure 4.13: $C_I(\theta_1, \theta_2, \phi_1, \phi_2)$ (averaged) plotted for the reference in back-scatter ($\theta_1 = 10$ degrees and $\theta_2 = -10$ degrees). All angles satisfy equation (4.36).

which varied slowly to give the larger correlations in the previous section, in particular V_{z_2} , vary rapidly with θ_2 while θ_1 is fixed, as is the case when averaging.

It is interesting to note that figure 4.12 and figure 4.13 are now in line with the

intuitive argument presented in chapter one, justifying the use of the specular arrangement when considering experimental correlations.

4.3 Results

Figures 4.14 and 4.15 show the experimentally observed correlation coefficients for surface #80, plotted with the results of averaging equation (4.33) as described above, for situations where incident and detected light are both s-polarised and p-polarised respectively. Although equation (4.33) does not take any polarisation effects into account, it is obviously adequate for predicting the observed behaviour.

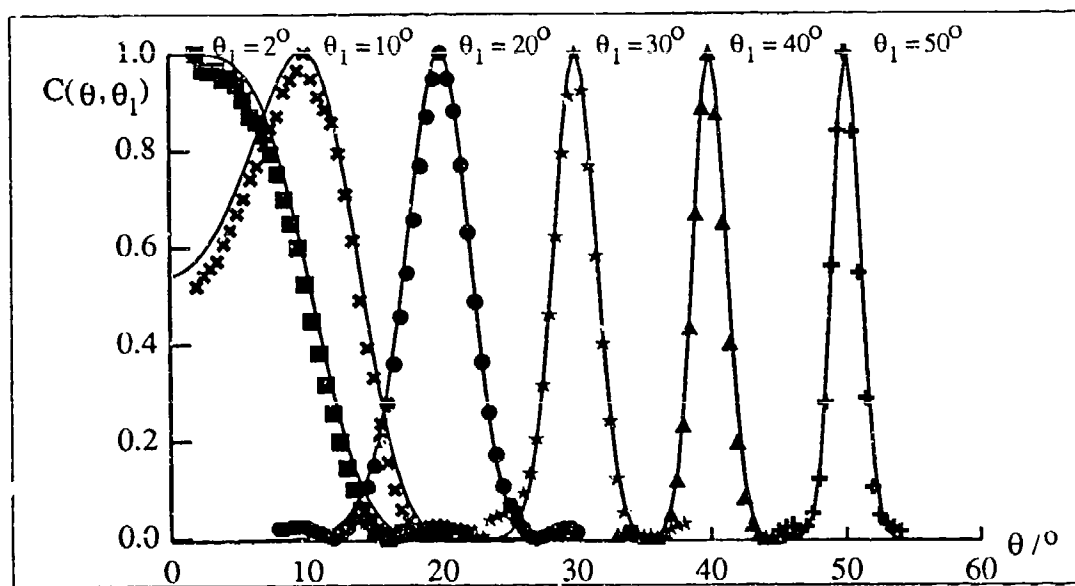


Figure 4.14: Experimental intensity correlations for surface #80 with incident and detected light s-polarised. Curve labels represent the (incident) angle at which the reference was taken. Observation is in the specular direction and $\lambda = 0.633\mu m$. The solid curves represent the results of averaging equation (4.33) using the experimental parameters. The symbols are experimental results.

As the measurements of the surface parameters obtained had some margin of doubt associated with them, figure 4.14 has been regraphed in figure 4.16 with the aver-

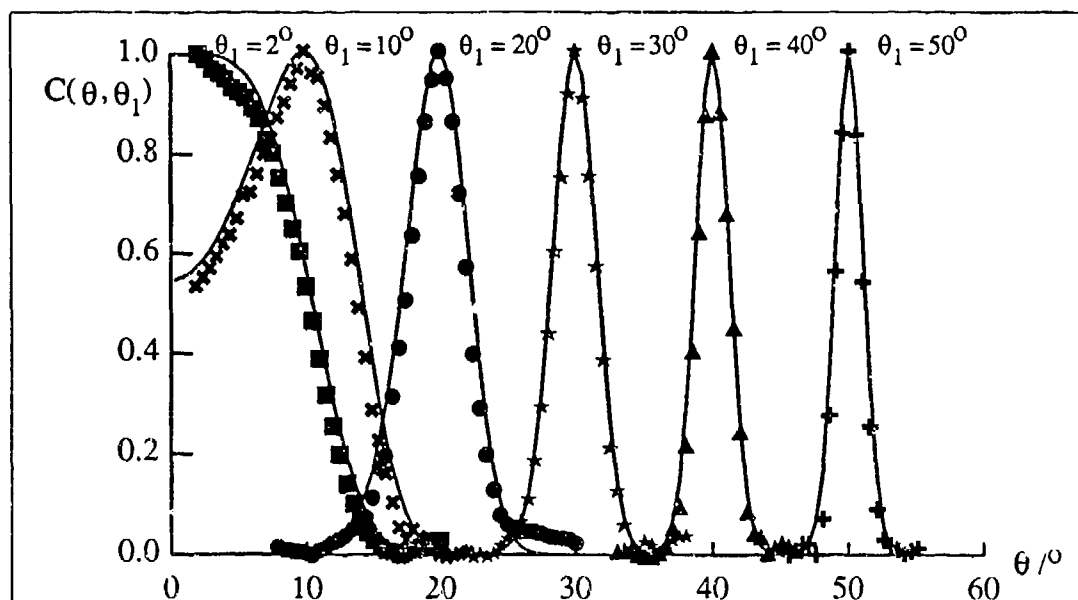


Figure 4.15: Experimental intensity correlations for surface #80 with incident and detected light p-polarised. Curve labels represent the (incident) angle at which the reference was taken. Observation is in the specular direction and $\lambda = 0.633\mu\text{m}$. The solid curves represent the results of averaging equation (4.33) using the experimental parameters. The symbols are experimental results.

aged equation (4.33), for the extremes of the error ranges in the R.M.S height and correlation length.

For the sake of completeness, the average intensity plot for surface #80 is given in figure 4.17. Both the incident and observed light are s-polarised. As may be expected, as the angle of incidence moves further away from being normal to the surface, the amount of light which is specularly reflected (as opposed to any other direction) increases.

As a matter of interest, analytical and experimental curves are also plotted for surface #239. This surface is predicted to show double scattering more evidently as the angle of incidence increases. For the co-polarised situations, figures 4.18 and 4.19, theoretical curves as above are plotted.

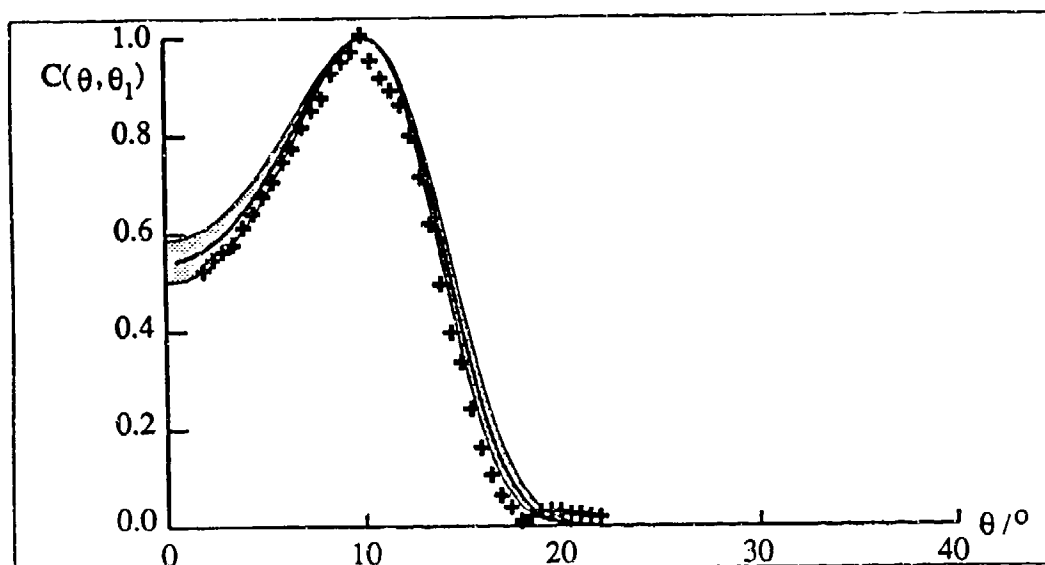


Figure 4.16: Equation (4.33) averaged over the area of the CCD element plotted with experimental correlations (+'s) taken from surface #80 as per figure 4.10 The grey area represents the region of uncertainty in the measurement of the surface parameters.

The agreement to the theoretical curves is not as good as it is with surface #80. This

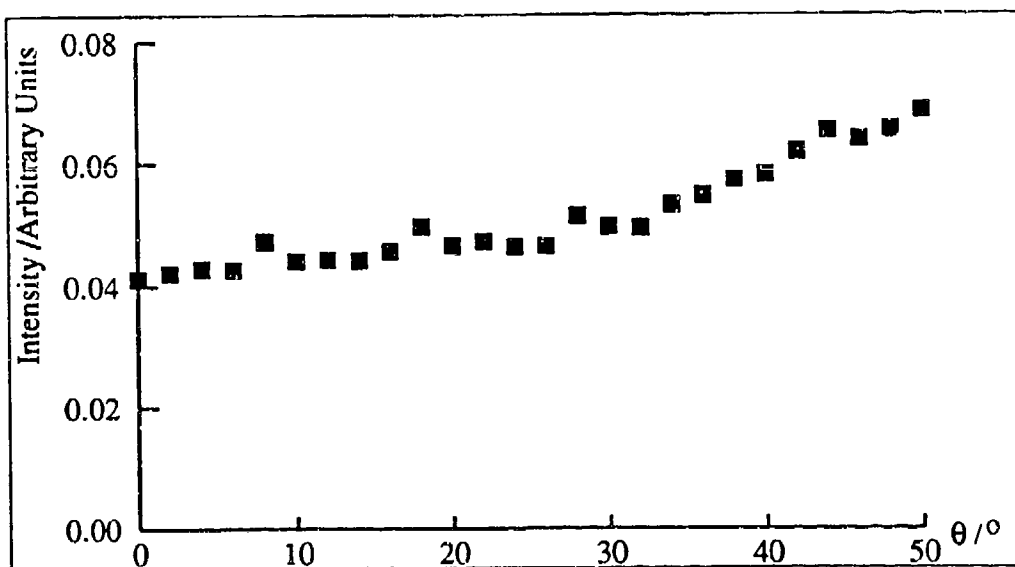


Figure 4.17: Averaged intensity plot for surface #80 with observation in the specular direction. The illuminating light has wavelength $0.633\mu\text{m}$ and it and the detected light are s-polarised.

may be expected as surface #239 is bordering on the margins of being a multiply scattering surface. It must be stressed that due to large gradients involved, the graphs can be misleading: to see the discrepancy between the experimental and analytical curves in its true light, the vertical distance between an experimental point and the theoretical curve must be considered.

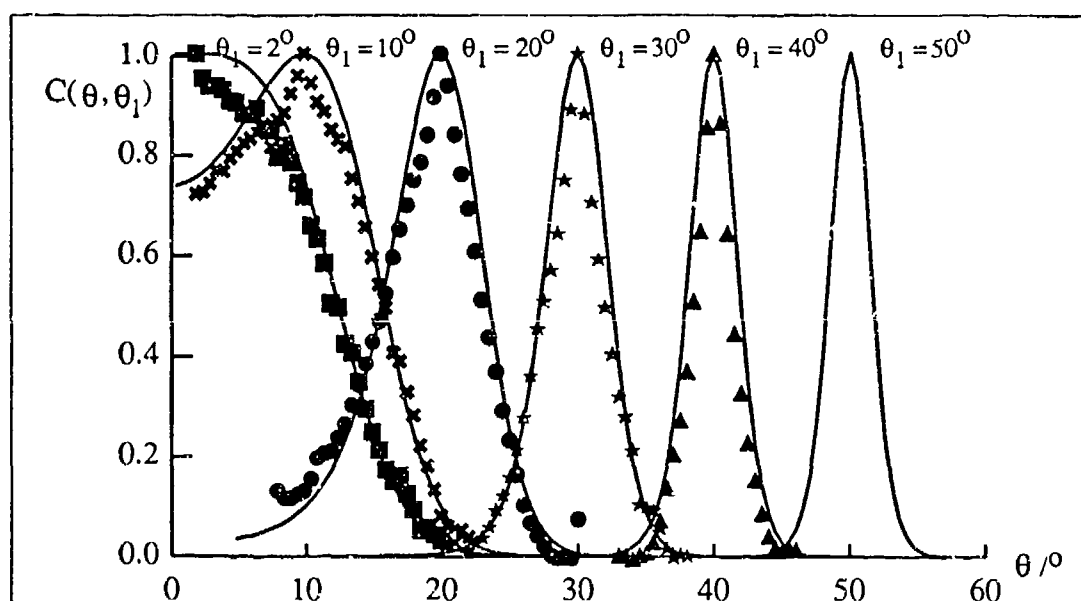


Figure 4.18: Experimental intensity correlations for surface #239 with incident and detected light s-polarised. Curve labels represent the (incident) angle at which the reference was taken. Observation is in the specular direction and $\lambda = 0.633\mu\text{m}$. The solid curves represent the results of averaging equation (4.33) using the experimental parameters. The symbols are experimental results.

Now that some double scattering is possible, cross-polarised correlations may be obtained, as shown in figures 4.20 and 4.21.

The cross-polarised component is very much less intense than the co-polarised one, so much so that Kim^[41] reported that no depolarisation was evident in scattering from this surface. For these results, long exposure times were required to produce speckle images with pixel values in the range specified in chapter three. The exposure time

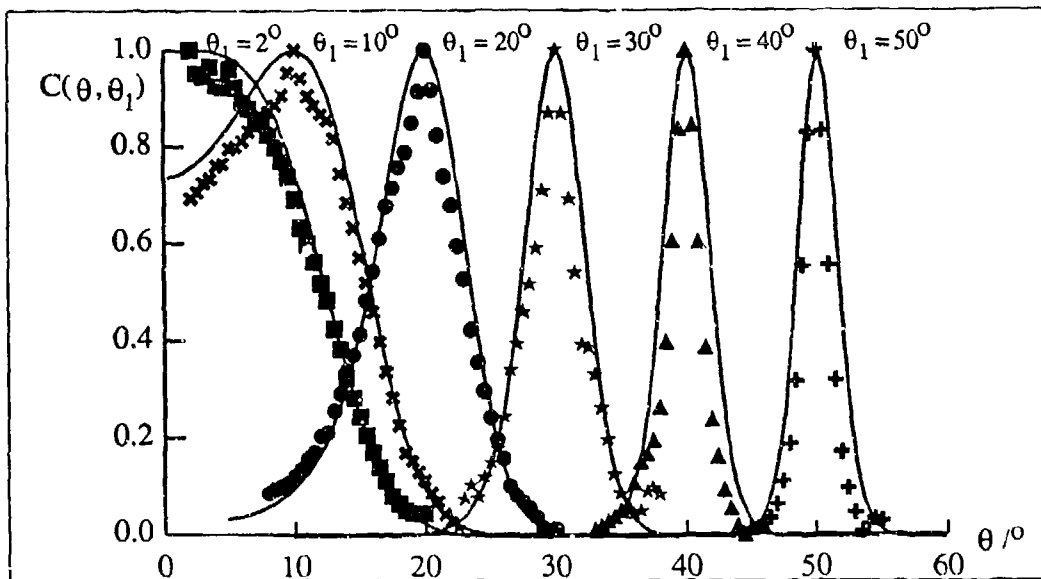


Figure 4.19: Experimental intensity correlations for surface #239 with incident and detected light p-polarised. Curve labels represent the (incident) angle at which the reference was taken. Observation is in the specular direction and $\lambda = 0.633\mu\text{m}$. The solid curves represent the results of averaging equation (4.33) using the experimental parameters. The symbols are experimental results.

was greater than 30 seconds for most of the data shown, coming close to 2 minutes for the higher angles. Although the large exposure times allow large amounts of ambient light to enter the camera, this is subtracted when the speckle images are processed. Further problems may be introduced experimental apparatus, with small amounts of detected cross polarised light, as discussed in chapter three.

One notable feature present in the cross-polarised curves is the existence of extra humps in the correlation at certain angles away from the main peak. The shapes of these curves are explained in chapter six.

The behaviour of the extra correlation humps in figure 4.20 is interesting, each individual curve has peaks at around three degrees either side of the main peak, but the value to which these rise varies, becoming lower with higher reference angles.

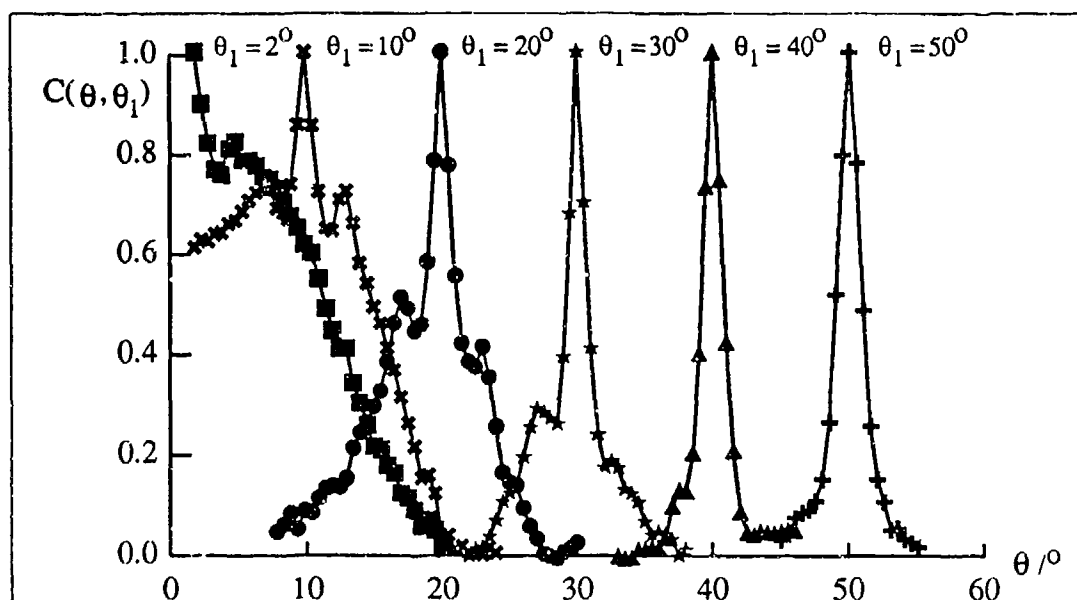


Figure 4.20: Experimental intensity correlations for surface #239 with incident light s-polarised and detected light p-polarised. Curve labels represent the (incident) angle at which the reference was taken. Observation is in the specular direction and $\lambda = 0.633\mu\text{m}$.

Figure 4.21 shows similar behaviour, but with the extra correlation humps being more evident at the larger reference angles. At the lower angles, however, the correlation coefficients seem to fluctuate randomly — no clearer picture is given if the curves are examined separately.

Figure 4.22 and figure 4.23 show averaged intensity plots for surface #239, for the case of observation in the specular direction, for s-polarised light incident and s- and p- polarised light detected respectively. The relative scaling between these graphs has not been preserved, the s-polarised experiment requiring a neutral density filter in the system to attenuate the amount of light incident on the surface.

As can be seen in the figures, as the angle of incidence moves away from normal, the amount of co-polarised light scattered into the specular direction increases. Con-

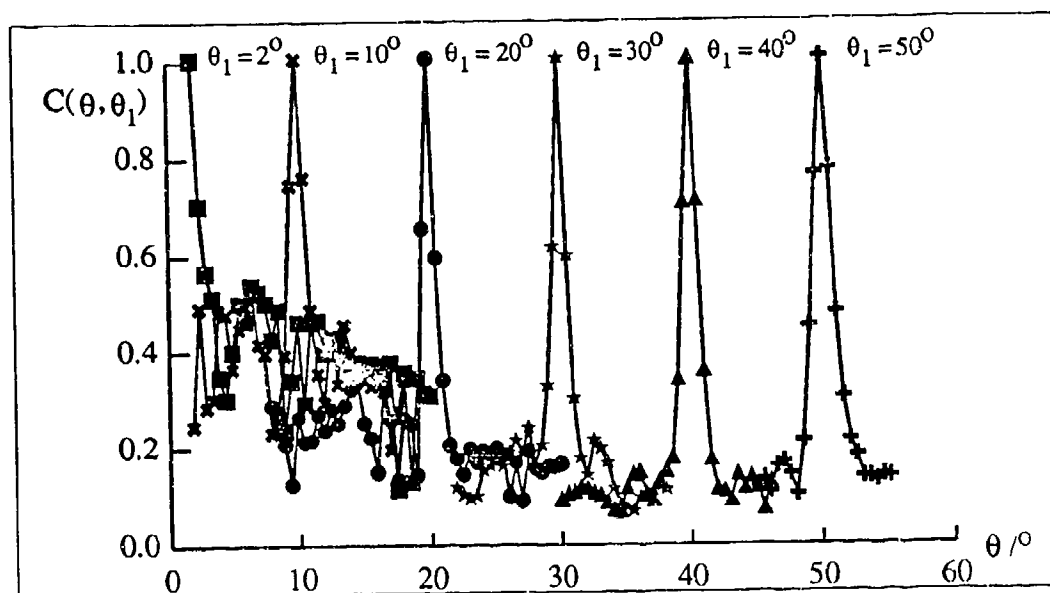


Figure 4.21: Experimental intensity correlations for surface #239 with incident light p-polarised and detected light s-polarised. Curve labels represent the (incident) angle at which the reference was taken. Observation is in the specular direction and $\lambda = 0.633\mu m$.

sequently, the amount of cross-polarised light (already small) decreases, hence the

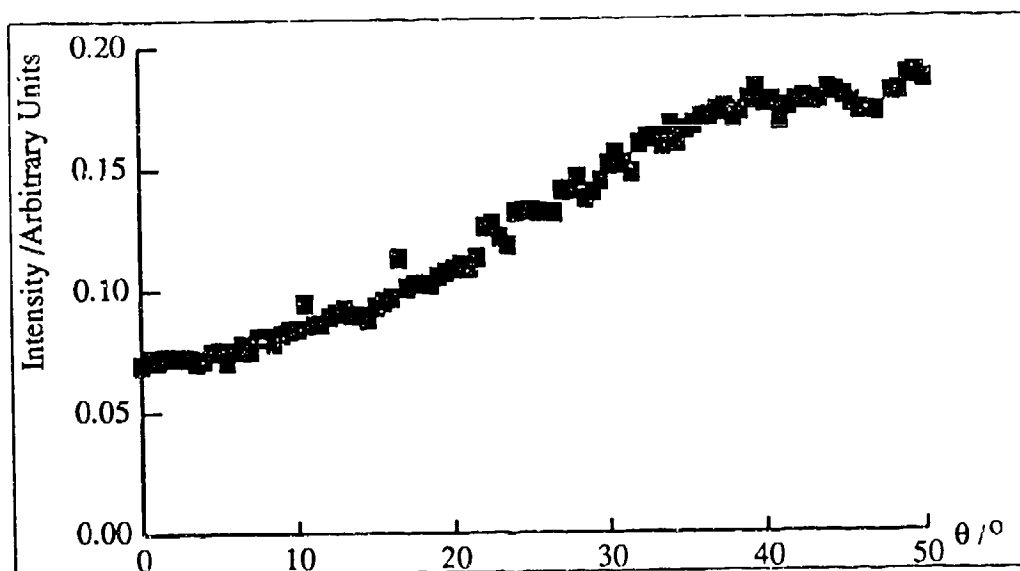


Figure 4.22: Averaged intensity plot for surface #239 with observation in the specular direction. The illuminating light has wavelength $0.633\mu m$ and it and the detected light are s-polarised.

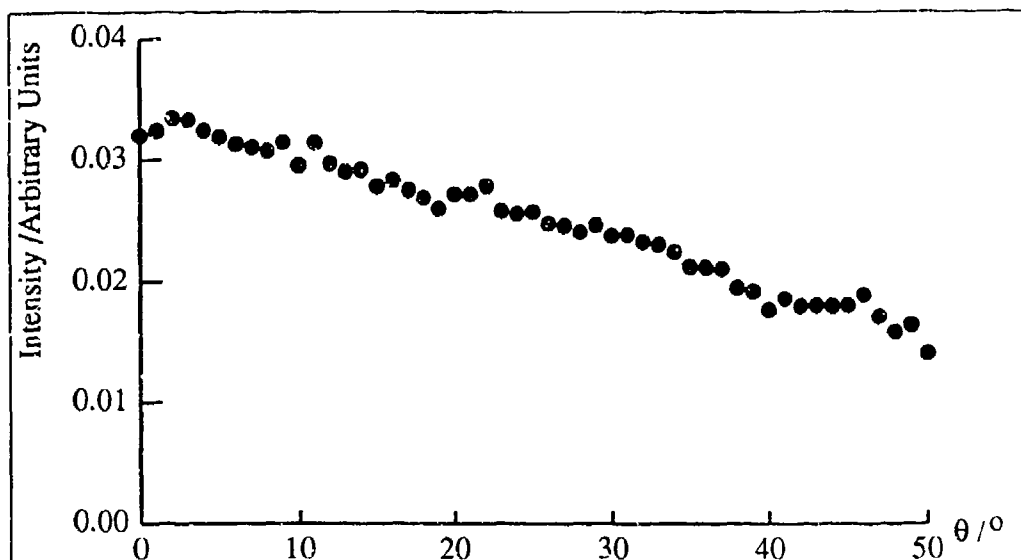


Figure 4.23: Averaged intensity plot for surface #239 with observation in the specular direction. The illuminating light has wavelength $0.633\mu m$ and is s-polarised. The detected light is p-polarised.

long exposure times needed to obtain the speckle images.

Since there are no obvious side lobes in figure 4.22 or figure 4.23, it seems that the correlation of speckle patterns is a much more sensitive probe of the multiple scattering regime than is the average intensity. This final piece of evidence offered up by scattered light from surface #239 (that the surface only shows slight evidence of double scattering), lends a great deal of support to the simple model near the start of this chapter which predicted such behaviour on the basis of equation (4.16).

Chapter 5

Double Scatter Simulation

5.1 Theory

The Kirchhoff approximation will be used to obtain an expression for the double scatter component of the scattered light in the far field by applying it to the Helmholtz-Kirchhoff integral. This method was employed by Bruce^[6] for one-dimensional surfaces and it seemed the most likely candidate for an extension into two dimensions.

Light incident on the surface is treated as being scattered into two states — one in which the light leaves the surface, and the other in which the light strikes the surface again at a different point. Of the light which impinges on the surface again, some will scatter and leave the surface and some will strike it a third time. Light continues to be scattered from the surface until it has all escaped (or in the case of a non-perfect conductor, been absorbed).

Bruce found that when considering perfectly conducting surfaces for which the Kirchhoff approximation can be applied, such as those discussed here, over 97%

of the incident light had left the surface after the second contact^[22]; the amount of triple (and higher) scattered light gave a negligible contribution to the final scattered field.

Only the single and double scatter components of the scattered field will be dealt with in the present study. The small power loss evidenced with this approach was deemed an acceptable price for extending the calculation to deal with two dimensional surfaces.

5.1.1 The Single Scatter Contribution

The equation to be used for the single scatter contribution is equation (4.10), derived in the previous chapter. It represents the contribution to the electric field due to light which only interacts with the surface once. Obviously, for surfaces which possess steep sided features, light will scatter from more than one point before it finally escapes.

5.1.2 The Double Scatter Contribution

Following a procedure similar to that used to gain the single scatter component, an expression will be derived for the double scatter component of the scattered light in the far field.

The nomenclature to be used is shown in figure 5.1, the subscripts 1 and 2 represent arbitrary realisations of functions at points 1 and 2, e.g., \mathbf{n}_1 is the surface normal at point 1, and is a function of the coordinates of that point.

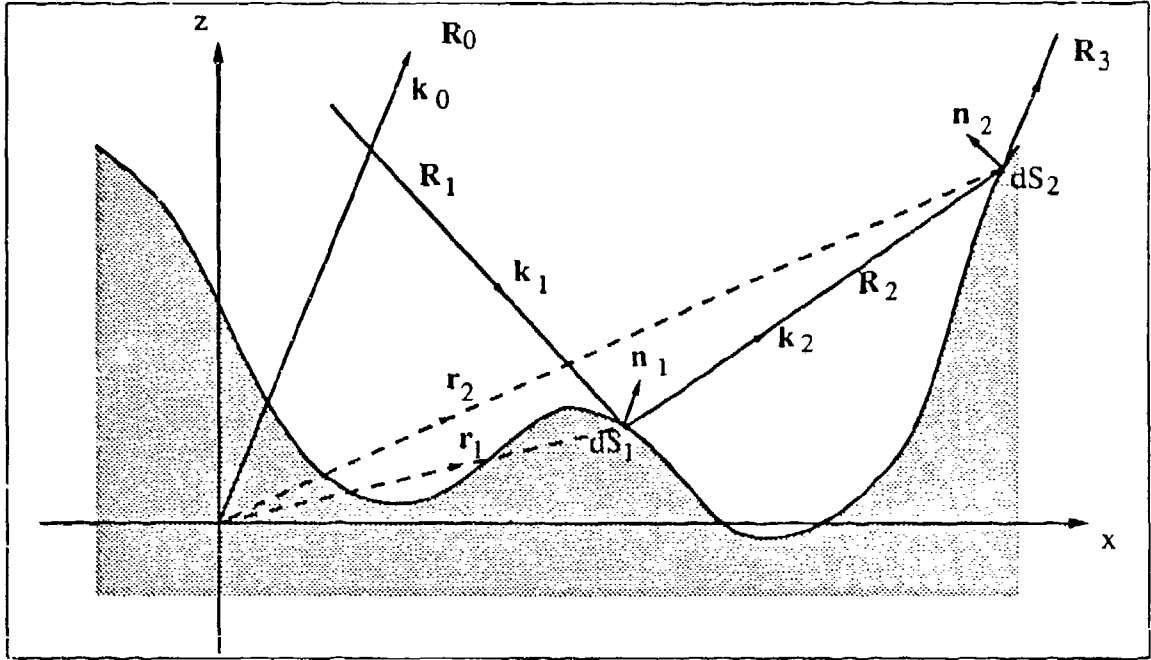


Figure 5.1: Geometry for the double scatter component of the scattered field.

Given an incident field on a surface, E_1 , the field after scattering once can be written, from equation (2.48), as

$$E_2 = \frac{1}{4\pi} \iint_{S_1} E_{1s} \frac{\partial \psi_{12}}{\partial n_1} - \psi_{12} \frac{\partial E_{1s}}{\partial n_1} dS_1 \quad (5.1)$$

and the double scattered component of the scattered field can be written as

$$E_3 = \frac{1}{4\pi} \iint_{S_2} E_{2s} \frac{\partial \psi_{23}}{\partial n_2} - \psi_{23} \frac{\partial E_{2s}}{\partial n_2} dS_2 \quad (5.2)$$

where, as previously, ψ is the free space Green's function,

$$\psi_{is} = \frac{e^{ik_s R_s}}{R_s} \quad (5.3)$$

The fields at the surface and their normal derivatives in equation (5.1 and equation 5.2), can be given by the Kirchhoff approximation, such that

$$E_{1s} = (1 + \mathcal{R}_1)E_1$$

$$\begin{aligned}
E_{2s} &= (1 + \mathcal{R}_2)E_2 \\
\frac{\partial E_{1s}}{\partial \mathbf{n}_1} &= (1 - \mathcal{R}_1)\frac{\partial E_1}{\partial \mathbf{n}_1} \\
\frac{\partial E_{2s}}{\partial \mathbf{n}_2} &= (1 - \mathcal{R}_2)\frac{\partial E_2}{\partial \mathbf{n}_2}
\end{aligned} \tag{5.4}$$

where \mathcal{R}_1 and \mathcal{R}_2 are the Fresnel reflection coefficients of the surface at points 1 and 2.

Combining equations (5.1, 5.2 and 5.4) leads to an expression for the double scattered field depending on the incident field,

$$\begin{aligned}
E_3 = \left(\frac{1}{4\pi}\right)^2 \iint_{S_2} \iint_{S_1} (1 + \mathcal{R}_2) \frac{\partial \psi_{23}}{\partial \mathbf{n}_2} \left[(1 + \mathcal{R}_1) E_1 \frac{\partial \psi_{12}}{\partial \mathbf{n}_1} - (1 - \mathcal{R}_1) \psi_{12} \frac{\partial E_1}{\partial \mathbf{n}_1} \right] \\
+ (1 - \mathcal{R}_2) \psi_{23} \left[(1 + \mathcal{R}_1) E_1 \frac{\partial \psi_{12}}{\partial \mathbf{n}_1 \partial \mathbf{n}_2} - (1 - \mathcal{R}_1) \frac{\partial \psi_{12}}{\partial \mathbf{n}_2} \frac{\partial E_1}{\partial \mathbf{n}_1} \right] dS_1 dS_2 \tag{5.5}
\end{aligned}$$

Taking the incident field as a plane wave of amplitude E_0 , as before

$$E_1 = E_0 e^{i\mathbf{k}_1 \cdot \mathbf{r}_1} \tag{5.6}$$

and the normal derivative at the surface at point 1 becomes

$$\frac{\partial E_1}{\partial \mathbf{n}_1} = i E_0 \mathbf{n}_1 \cdot \mathbf{k}_1 e^{i\mathbf{k}_1 \cdot \mathbf{r}_1} \tag{5.7}$$

Also, ψ_{12} may be written from equation (5.3) as

$$\psi_{12} = \frac{e^{ik_0 R_2}}{R_2} \tag{5.8}$$

and by taking the double scattered component of light out to the far field and so expressing \mathbf{R}_3 as

$$\mathbf{R}_3 = \mathbf{R}_0 - \mathbf{r}_2 \tag{5.9}$$

then (observing that \mathbf{k}_0 and \mathbf{k}_3 are identical),

$$\psi_{23} = \left(\frac{e^{ik_0 R_0}}{R_0} \right) e^{-i\mathbf{k}_3 \cdot \mathbf{r}_2} \quad (5.10)$$

and

$$\frac{\partial \psi_{23}}{\partial \mathbf{n}_2} = -i\mathbf{n}_2 \cdot \mathbf{k}_3 \left(\frac{e^{ik_0 R_0}}{R_0} \right) e^{-i\mathbf{k}_3 \cdot \mathbf{r}_2} \quad (5.11)$$

The remaining terms of equation (5.5) are derived by expanding equation (5.8) into cartesian coordinates (i.e., $R_2 = \sqrt{(x_2 - x_1)^2 + (y_2 - y_1)^2 + (z_2 - z_1)^2}$) and applying the operator (2.13). Their final forms are

$$\begin{aligned} \frac{\partial \psi_{12}}{\partial \mathbf{n}_1} &= (C - iD)\psi_{12} \\ \frac{\partial \psi_{12}}{\partial \mathbf{n}_2} &= (-A + iB)\psi_{12} \\ \frac{\partial \psi_{12}}{\partial \mathbf{n}_1 \partial \mathbf{n}_2} &= \left[\frac{\mathbf{n}_2 \cdot \mathbf{n}_1}{R_2} \left(\frac{1}{R_2} - ik_0 \right) + 2iAD - 3AC + BD \right] \psi_{12} \end{aligned} \quad (5.12)$$

where

$$\begin{aligned} A &= \frac{\mathbf{n}_2 \cdot \mathbf{R}_2}{R_2^2} \\ B &= \mathbf{n}_2 \cdot \mathbf{k}_2 \\ C &= \frac{\mathbf{n}_1 \cdot \mathbf{R}_2}{R_2^2} \\ D &= \mathbf{n}_1 \cdot \mathbf{k}_2 \end{aligned} \quad (5.13)$$

Thus, for a given arrangement of illumination and observation, and with a known surface profile, only the reflection coefficients remain to be determined in equation (5.5). With a perfectly conducting surface, the reflection coefficients can be set to +1 or -1 for p-polarised or s-polarised incident light respectively: this is due to a perfect conductor being a perfect reflector^[39]. For the one dimensional case, where

no change in polarisation occurs upon scattering, this is all that is required; but for a two dimensional surface — where the polarisation can change upon scattering out of the incident plane — changes in the reflection coefficients must be taken into account.

5.1.3 Including Polarisation

Following Mitzner^[46] and Beckmann^[19], the electric field E can be split into two orthogonal components, one which is s-polarised E^- , and the other p-polarised E^+ . The scattering geometry is shown in figure 5.2. The vectors \mathbf{e}^- and \mathbf{e}^+ are unit vectors representing the s-polarised and p-polarised electric vector alignments respectively. \mathbf{x}, \mathbf{y} and \mathbf{z} are orthogonal unit vectors describing the coordinate system used. The scattered field can be expressed in terms of the incident field as

$$\begin{bmatrix} E_s^- \\ E_s^+ \end{bmatrix} = \begin{bmatrix} \Gamma_{\parallel}^- & \Gamma_{\perp}^- \\ \Gamma_{\perp}^+ & \Gamma_{\parallel}^+ \end{bmatrix} \begin{bmatrix} E_i^- \\ E_i^+ \end{bmatrix} \quad (5.14)$$

where E_i^- and E_i^+ is the incident field, E_s^- and E_s^+ the scattered field, and the Γ 's are the reflection coefficients; subscript \parallel indicates the component of the reflection coefficient which does not change polarisation and \perp indicates the component of the reflection coefficient which maps one polarisation state to the other. These reflection coefficients are effectively the Fresnel reflection coefficients (\mathcal{R}^- and \mathcal{R}^+) transformed from the local scattering plane into the world frame. Note that in the world frame the s-polarised and p-polarised electric vectors lie perpendicular and parallel to the plane of incidence — once scattering is considered from a local point of view this is no longer true, hence the coordinate transforms. These new reflection coefficients are derived by Mitzner^[46]:

$$\Gamma_{\parallel}^- = \mathcal{R}^- \cos \beta_i \cos \beta_s + \mathcal{R}^+ \sin \beta_i \sin \beta_s$$

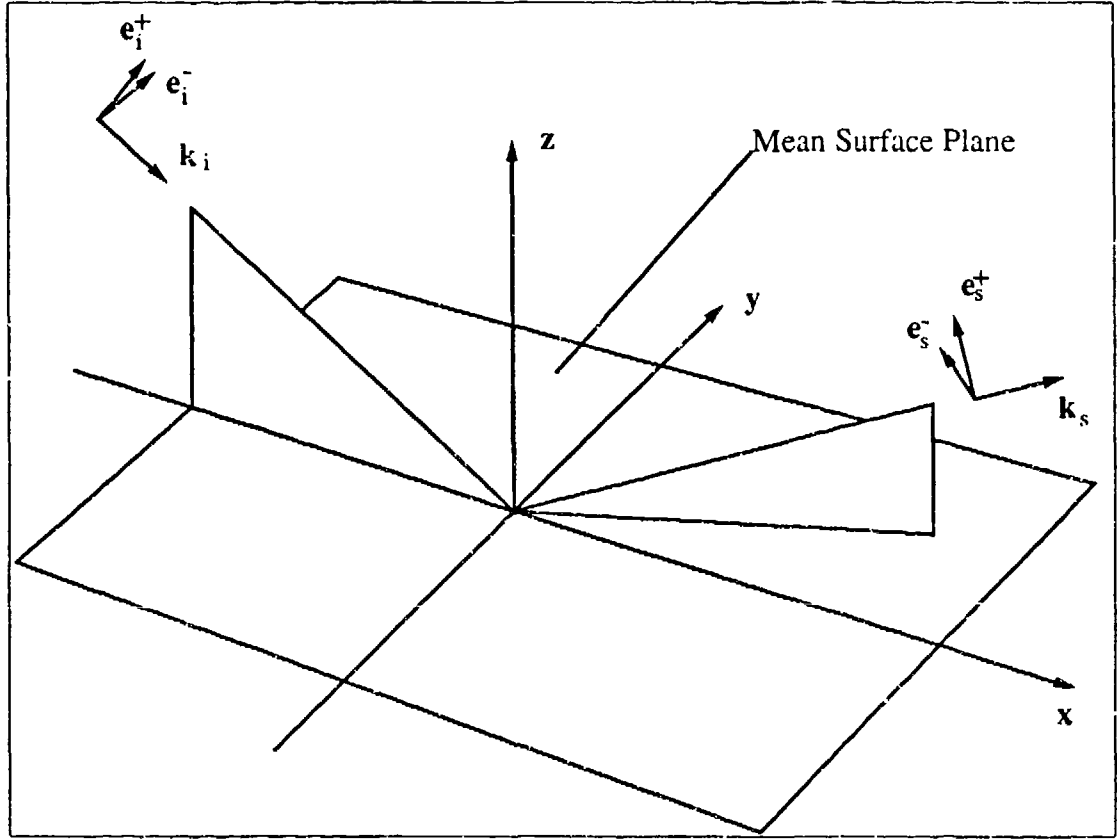


Figure 5.2: Geometry for polarisation showing the orientation of the electric field coordinate systems within the world frame.

$$\begin{aligned}
 \Gamma_{\parallel}^{+} &= \mathcal{R}^{-} \sin \beta_i \sin \beta_s + \mathcal{R}^{+} \cos \beta_i \cos \beta_s \\
 \Gamma_{\perp}^{-} &= -\mathcal{R}^{-} \sin \beta_i \cos \beta_s + \mathcal{R}^{+} \cos \beta_i \sin \beta_s \\
 \Gamma_{\perp}^{+} &= -\mathcal{R}^{-} \cos \beta_i \sin \beta_s + \mathcal{R}^{+} \sin \beta_i \cos \beta_s
 \end{aligned} \tag{5.15}$$

β_i and β_s are the angles between the local scattering plane and the incident and scattered polarisation coordinate systems respectively, as shown in figure 5.3, and can be defined as

$$\cos \beta_x = \mathbf{t}_x \cdot \mathbf{e}_x^{-} \tag{5.16}$$

or

$$\sin \beta_x = \mathbf{q}_x \cdot \mathbf{e}_x^{-} \tag{5.17}$$

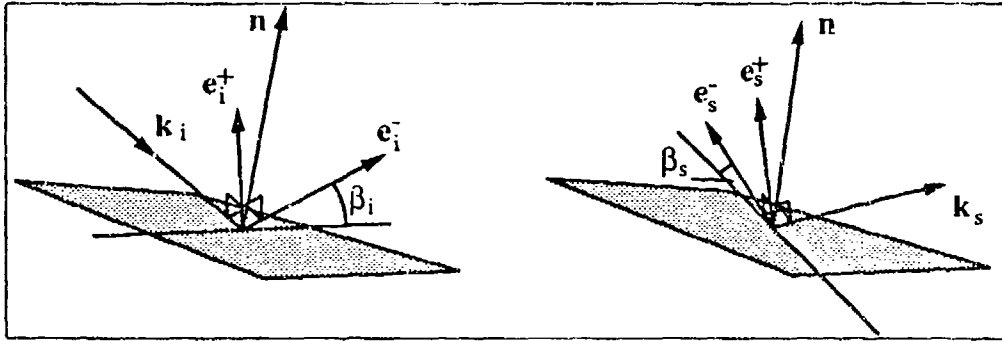


Figure 5.3: Relative orientation of the electric field coordinate systems with respect to the local scattering plane.

for $x = i, s$, where

$$\mathbf{t}_x = \frac{\mathbf{n} \times \mathbf{k}_x}{|\mathbf{n} \times \mathbf{k}_x|} \quad (5.18)$$

is a unit vector along the intersection of the local scattering plane with the wave fronts, as shown (along with \mathbf{q}_x) in figure 5.4, and \mathbf{e}_x^- is the direction of the s-polarised component of the electric field. Expressed in world coordinates,

$$\mathbf{e}_i^- = \mathbf{y} \quad (5.19)$$

and

$$\mathbf{e}_s^- = \frac{-(\mathbf{k}_s \cdot \mathbf{y})\mathbf{x} + (\mathbf{k}_s \cdot \mathbf{x})\mathbf{y}}{\sqrt{1 - (\mathbf{k}_s \cdot \mathbf{z})}} \quad (5.20)$$

The process of keeping track of the polarisation can be thought of as first a transformation of the $(\mathbf{e}_i^-, \mathbf{e}_i^+)$ system into one which lies in the $(\mathbf{t}_i, \mathbf{q}_i)$ plane. This is followed by scattering the light according to equation (5.1) or (5.2). Finally the coordinate system (which now lies in the $(\mathbf{t}_s, \mathbf{q}_s)$ plane) is transformed to the $(\mathbf{e}_s^-, \mathbf{e}_s^+)$ arrangement. The overall effect is a change in polarisation.

A limitation must now be imposed: the Fresnel reflection coefficients only apply to a specular reflection from a flat plane, and so the above procedure will not work if

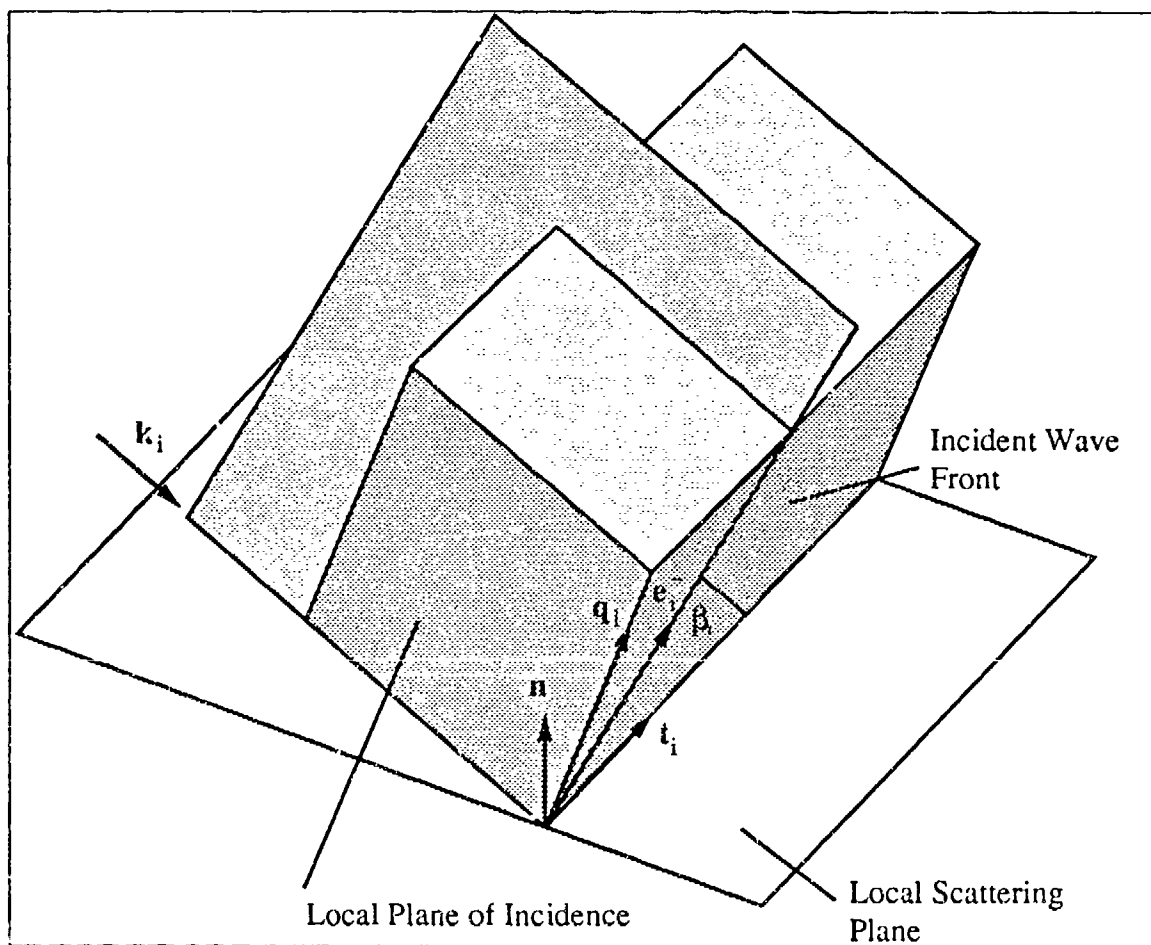


Figure 5.4: Detail of the relationship between the electric field coordinate system and the local scattering plane.

k_i , k_s and n do not lie within the same plane. When they do, $t_i = t_s = t$, and the polarisation is correct. Having imposed this limitation, the polarisation change no longer depends explicitly on the surface normal, and t may be rewritten in terms of the incident and scattered wave vectors:

$$t = \frac{k_i \times k_s}{|k_i \times k_s|} \quad (5.21)$$

A model is now needed to cope with light scattered out of the local plane of incidence (a diffraction effect supported by the Kirchhoff method used). If any light is

scattered in some direction \mathbf{k}_s , from a scattering element, with incident light in the direction \mathbf{k}_i , then the existence of a virtual plane, oriented such that the scattered light is specularly reflected, may be considered. The polarisation of the light is then given, as above, by applying the reflection coefficients on this plane with \mathbf{t}_i and \mathbf{t}_s as in equation (5.21). The actual orientation of the virtual plane is never needed as \mathbf{k}_i and \mathbf{k}_s are already determined. This approximation to whatever polarisation change is occurring is justified since the surfaces to be studied here must conform to the Kirchhoff approximation, i.e., most of the light scattered from any point will be as if from a plane mirror. A qualitative argument successfully explaining polarisation changes in enhanced back-scatter has been based on a similar assumption^[11].

Clearly it is necessary, from equation (5.14), to work out both the s- and p-polarised components of E_2 (cf. equation (5.1)), before a single realisation of E_3 (equation (5.2)), be it s- or p-polarised, can be determined.

5.2 Implementation

Given that the single and double scatter components of the electric field are now realised, the total scattered field is simply the sum of the two components.

The angular intensity correlation, the quantity sought here, depends on two realisations of the intensity, $I_1 = I(\mathbf{k}_1, \mathbf{k}_3)$ and $I_2 = I(\mathbf{k}'_1, \mathbf{k}'_3)$, taken from N realisations of the surface, and is obtained using equation (2.15) from chapter two:

$$C_I(\mathbf{k}_1, \mathbf{k}_3, \mathbf{k}'_1, \mathbf{k}'_3) = \frac{\frac{\sum I_1 I_2}{N} - \frac{\sum I_1}{N} \frac{\sum I_2}{N}}{\sqrt{\left(\frac{\sum I_1^2}{N} - \left(\frac{\sum I_1}{N}\right)^2\right) \left(\frac{\sum I_2^2}{N} - \left(\frac{\sum I_2}{N}\right)^2\right)}} \quad (5.22)$$

The total electric field can be expressed as an intensity (defined as the energy crossing a unit area in unit time) by:

$$I = \frac{c}{4\pi} EE^* \quad (5.23)$$

Examining equation (5.22), it can be seen that any constant factors in I , and hence (from equation (5.23)) in the electric field E , may be discarded when only considering the correlation. Note that this only applies to factors common to both the single and double scatter components of E and I — their relative scaling must not be disturbed. This removal of all terms constant with respect to angle means, especially, that the correlation does not depend upon R_0 , a term which (as it is the position of observation in the far field) tended towards infinity.

5.2.1 Discretisation for Computer Modeling

The integration over the surface in equations (4.4) and (5.5) shall be performed simply by multiplying the value calculated at the centre of a unit by the area of that unit, as shown in figure 5.5. This makes discretisation of the equations simple; it is achieved merely by changing the integral signs to sums over the x and y directions and replacing dS with ΔS_{xy} , the area of the unit. Obviously this is a very simplistic approximation to the actual integral — a more accurate calculation might extend Simpson's rule into two-dimensions.

It is generally deemed necessary, while considering discretisation of equation (5.5) and all associated parts, that the phase terms present, namely $e^{-ik_1 \cdot r_1}$, $e^{ik_3 \cdot r_2}$ and $e^{ik_0 R_2}$, must be viewed with respect to their variation. In order to maintain a realistic idea of this phase over a discretised surface, its variation must be much smaller than

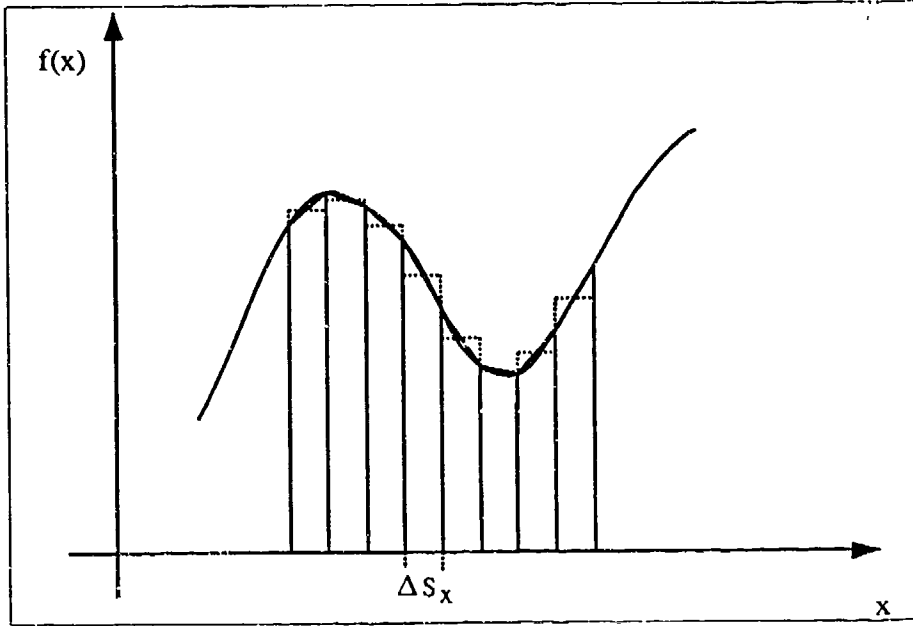


Figure 5.5: Numerical integration performed by taking the mid-point of two realisations of a function and multiplying it by their separation.

2π between two consecutive surface points. Taking just the $k_0 R_2$ term, as this varies fastest, the condition can be written as

$$\Delta(k_0 R_2) \ll 2\pi \quad (5.24)$$

where Δ indicates the change over consecutive points. Replacing k_0 by $2\pi/\lambda$, the condition becomes

$$\Delta R_2 \ll \lambda \quad (5.25)$$

The largest change in R_2 will be of the order of the distance between points on the discretised surface, so to track the phase reliably across a discretised surface there must be many sample points per wavelength. There is, however, a problem with this approach: the discretised surface will have so many points on it that the calculation would be unrealistically slow; also, the fast shading algorithm (see below), would require so much memory that it would not be possible to implement

it. The integration will therefore be performed with a grid separation controlled by the correlation length of the gradient of the surface, this being the c^{-1} half width of the correlation function of the gradient (from equation (2.30)):

$$C_{S'S'}(t) = \left(1 - 2\frac{t^2}{\tau^2}\right) e^{-\frac{t^2}{\tau^2}} \quad (5.26)$$

When this is equal to c^{-1} , the value of $t = \tau_{S'}$, the correlation length of the gradients (found by Newton-Raphson iteration), is approximately given by

$$\tau_{S'} \approx 0.51104\tau \quad (5.27)$$

i.e., for a surface with a correlation length $\tau = 4.31\lambda$, surface points will be separated by $4.31\lambda * 0.51104 = 2.20\lambda$. If 2048 points are available, then the surface side should be $\sqrt{2048 \times (2.20\lambda)^2} = 99.74\lambda$.

Surface segments spaced by this distance will still have similar gradients, and hence each segment may be considered to be locally flat. The distances between points on a surface will now constitute a random distribution (cf. Monte Carlo method). It can be seen from figure 5.6 that the phase spread over an ensemble average of 100 surfaces is relatively uniform, implying that it does not need to be tracked on a finer scale. The randomness of the surface points is enhanced by adding a small random offset to each x and y coordinate (which is linear and up to a maximum of $\lambda/10$) and interpolating to find the correct z coordinate on the surface; i.e., the surface realisations are not confined to a fixed grid which may impose its own structure onto any results.

To perform the integration, a sum over flat surface segments must be conducted (a requirement of the Kirchhoff approximation). Somehow, these flat facets must be

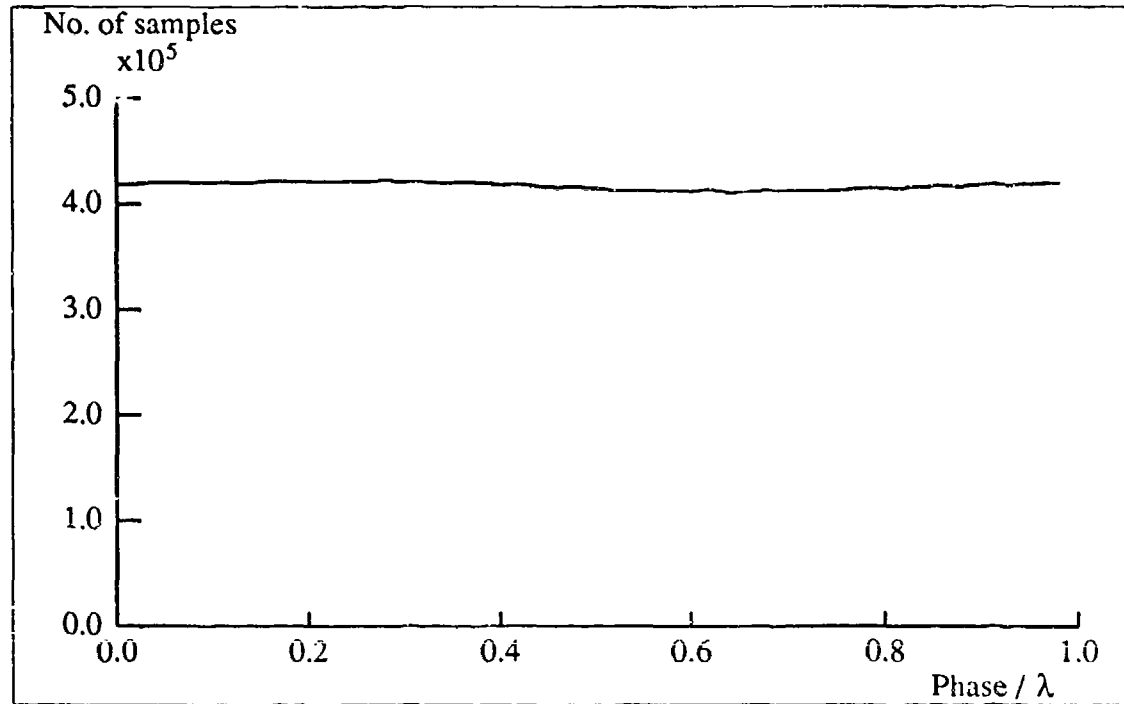


Figure 5.6: The distribution of the phase differences between two points binned 50 times over the wavelength, on a 100×100 wavelength surface consisting of 2048 points, with parameters $\sigma = 1.42\lambda$ and $\tau = 4.31\lambda$, over an ensemble average of 100 surfaces. Point to point shading has been taken into account.

obtained from the data available, namely a square grid of surface heights (given the nature of the surface generation technique which relies on fast Fourier transforms — see below). In actual fact, the grid must be disturbed to create a random distribution of points, but for the purposes of this explanation a square grid will be considered.

Since it is unlikely that four independent points will all lie in a flat plane, each 'square' of the surface (defined by the four corner points), must be split into two triangles, both of which are uniquely defined planes, as shown in figure 5.7. This complicates the summation procedure slightly as it is now necessary to cater for the two sub-triangles within each unit.

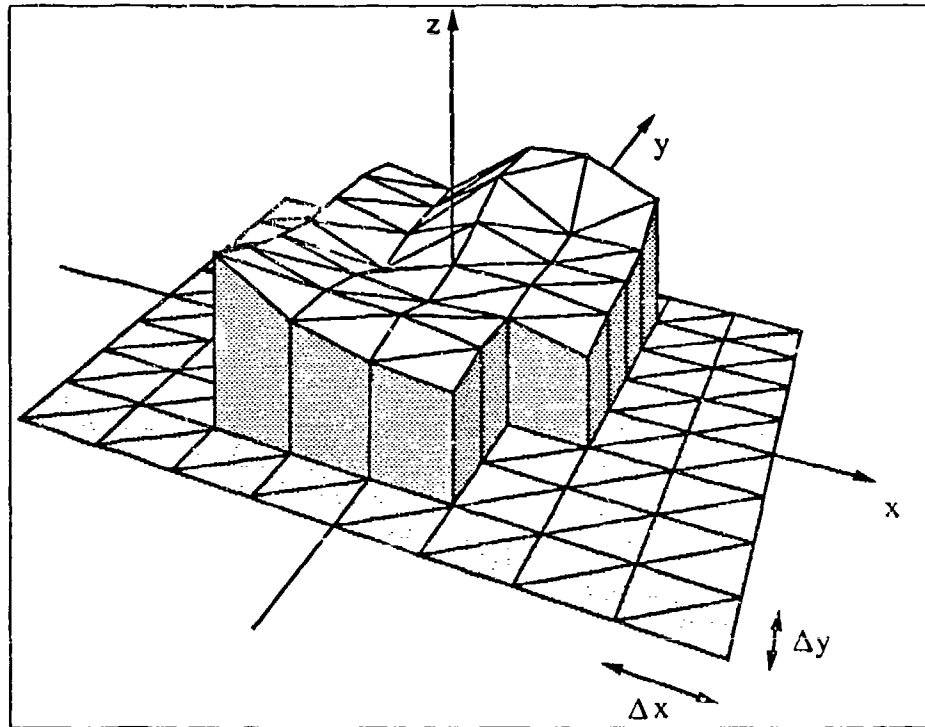


Figure 5.7: A discretised two-dimensional surface — each facet is a flat plane.

The ΔS_{xy} required for a triangular unit can be defined as

$$\Delta S_{xy} = \frac{\Delta x \Delta y}{2n_z} \quad (5.28)$$

the area of a surface facet with a surface normal \mathbf{n} (n_z is the component which lies along the z direction) on a triangular base of area $\Delta x \Delta y / 2$. The positions of the mid-point of each facet (see figure 5.8) are given by averaging the positions of the three corners, for facet A the mid-point is

$$\begin{aligned} A_x &= \frac{P_{1x} + P_{2x} + P_{3x}}{3} = P_{1x} + \frac{1}{3} \Delta x \\ A_y &= \frac{P_{1y} + P_{2y} + P_{3y}}{3} = P_{1y} + \frac{2}{3} \Delta y \\ A_z &= \frac{P_{1z} + P_{2z} + P_{3z}}{3} \end{aligned} \quad (5.29)$$

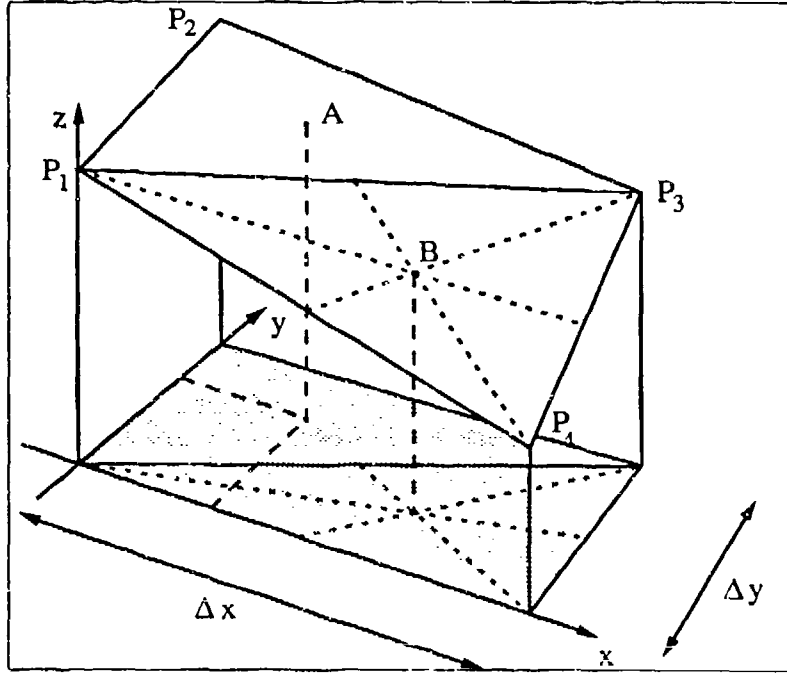


Figure 5.8: Geometry for calculating the positions of surface facets.

and for facet B

$$\begin{aligned}
 B_x &= \frac{P_{1x} + P_{3x} + P_{4x}}{3} = P_{1x} + \frac{2}{3}\Delta x \\
 B_y &= \frac{P_{1y} + P_{3y} + P_{4y}}{3} = P_{1y} + \frac{1}{3}\Delta y \\
 B_z &= \frac{P_{1z} + P_{3z} + P_{4z}}{3}
 \end{aligned} \tag{5.30}$$

where the points P_1, P_2, P_3 and P_4 are four realisations at the corners of the square unit. The surface normal for each facet can be derived by taking the vector cross product of two sides of a facet:

$$\mathbf{n}_A = P_2P_1 \times P_2P_3 = -\Delta y(P_{3z} - P_{2z})\mathbf{x} + \Delta x(P_{1z} - P_{2z})\mathbf{y} + \Delta x\Delta y\mathbf{z} \tag{5.31}$$

$$\mathbf{n}_B = P_4P_3 \times P_4P_1 = \Delta y(P_{1z} - P_{4z})\mathbf{x} - \Delta x(P_{3z} - P_{4z})\mathbf{y} + \Delta x\Delta y\mathbf{z} \tag{5.32}$$

Of course, these vectors still need to be normalised by dividing each component by $|\mathbf{n}|$.

As mentioned above, the randomness of the distribution of points on the surface needs to be increased, this is achieved by shifting the corners of each square by a small random amount. The surface normal may still be defined by a cross product of two vectors describing the sides,

$$\begin{aligned} \mathbf{n}_A &= \mathbf{a}_A \times \mathbf{b}_A = P_2 P_1 \times P_2 P_3 \\ \mathbf{n}_B &= \mathbf{a}_B \times \mathbf{b}_B = P_4 P_3 \times P_4 P_1 \end{aligned} \quad (5.33)$$

although the solution is not so trivial as before, it is nevertheless a simple calculation.

The most significant complication introduced by randomising the surface nodes is that the surface area dS of each facet needs explicit calculation (see figure 5.9), not particularly difficult in itself, but meaning one more quantity to keep track of. The area of a triangle described by two vectors joined at their bases is,

$$dS = \frac{1}{2}bc = \frac{1}{2}b|\mathbf{a} - \alpha\mathbf{b}| \quad (5.34)$$

where

$$\alpha = \frac{\mathbf{a} \cdot \mathbf{b}}{ab} \quad (5.35)$$

and \mathbf{a} and \mathbf{b} are two vectors describing the sides of the facet as in equation (5.33), assigned such that $b > a$. Note that c may be calculated via the dot product of \mathbf{a} and the normal to \mathbf{b} , but this method requires a normalisation and hence a square root. Bearing in mind that calculation speed is of the essence, the above method was chosen as it avoids the slow square root and uses a number of faster operations.

By this point in the development of the theory, it is not practical to write the calculations as a single equation or even just a few equations. However, this is of no concern when considering that it will be implemented on a computer — in fact it is an advantage to have expressed the theory as many small parts.

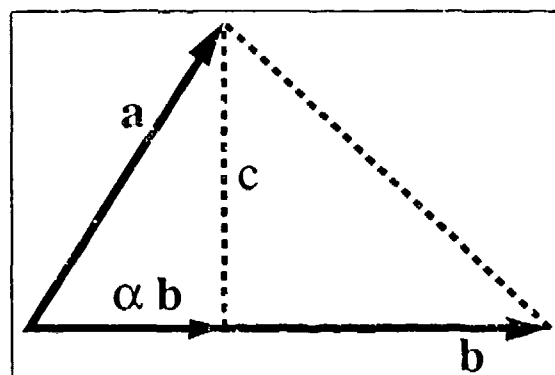


Figure 5.9: Geometry for calculation of area between two vectors.

5.2.2 Calculating Shaded Areas

So far, no allowance has been made for the effect the surface height variation has in terms of casting shadows; all points on the surface have been assumed illuminated at all times. Clearly, for steep sided features of the surface, especially at high (away from normal) angles of incidence, there are going to be portions of the surface which are in shadow. The inverse of this also applies: points on the surface which cannot be seen from the observation direction cannot directly contribute to the scattered light in that direction.

In the double scatter case, the effect of point to point shading must also be taken into account. Light cannot reach a point on one side of a hill from a point on the other side — this must be accounted for. Note that if the surface is discretised into N points, then the point to point calculation will have to be performed from 1 point to N points N times, i.e., N^2 point to point calculations. It is vital that this calculation is computationally as fast as possible. A direct ray trace, possibly the most obvious method for determining shaded regions, is too slow to be practical. Fortunately, it is not the only solution available.

Considering, for now, a one dimensional surface, figure 5.10 shows the shaded regions of that surface when light is incident on it. The vector \mathbf{s} is defined as that which lies

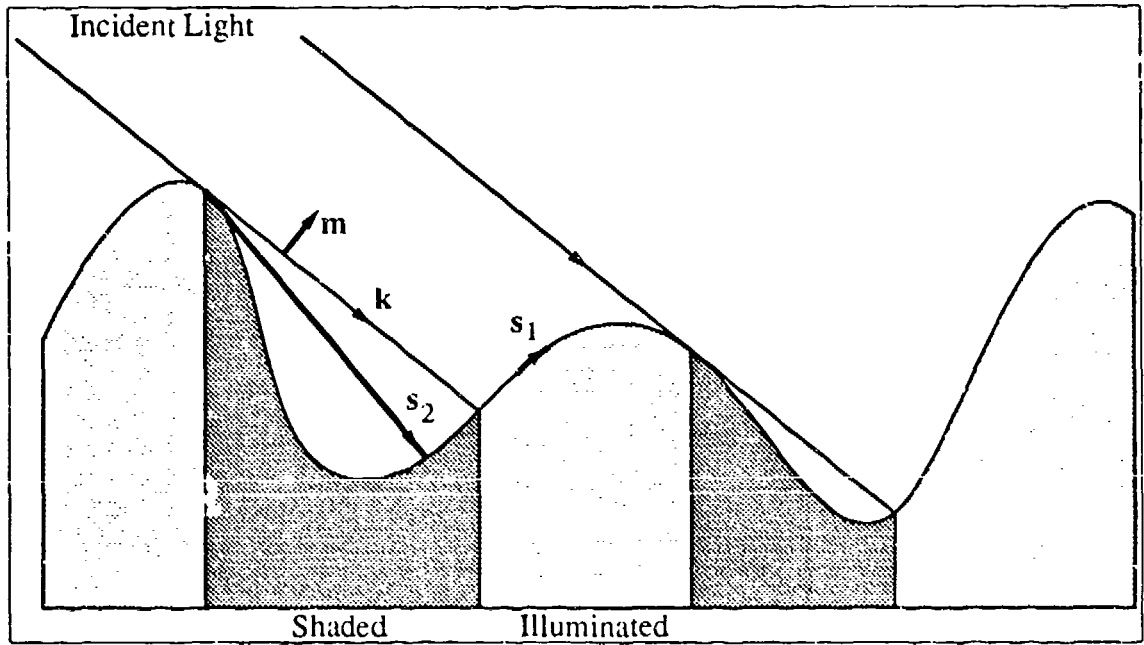


Figure 5.10: Shaded regions of a one-dimensional surface due to columnated incident light.

in the direction of the line joining the last illuminated point with the current point. Starting at the left side of the discretised surface, as each point is stepped through, \mathbf{s} is redefined. If a point lies in an illuminated area, then \mathbf{s} will simply be the vector joining two consecutive points (cf. \mathbf{s}_1). If, on the other hand, the point lies in a shaded region, then \mathbf{s} will be the vector joining the start of that shaded region with the current point (cf. \mathbf{s}_2). To determine if the current point is illuminated or shaded, the dot product of \mathbf{s} and the normal to the wave vector of the illuminating light, \mathbf{m} (as shown in figure 5.10), is taken. If

$$\mathbf{s} \cdot \mathbf{m} > 0 \quad (5.36)$$

then the current point is illuminated and the tail of \mathbf{s} is redefined as this point,

otherwise the point is shaded and the tail of \mathbf{s} is left alone.

For illumination to the right of the surface, the direction the surface is processed in must be reversed, i.e., stepping starts at the right hand side and the definition of \mathbf{m} is such that it still points 'up'. To calculate observed points, 'illumination' can be considered to be from the observation direction — 'shaded' regions are then areas which are not observable, and 'illuminated' regions, areas which are. Note that this algorithm only touches upon each surface point once.

As long as the observed direction is in the plane of incidence, a two-dimensional surface can be thought of (for the purposes of the above shadow calculations) as many one-dimensional surfaces lying side by side.

A similar method to that above can be used for point to point shadow calculations (see figure 5.11), the only difference being that the wave vector, and hence its normal \mathbf{m} , are no longer constant. However, the point to point calculation cannot be extended to that for a two-dimensional surface so trivially.

The solution to the problem of calculating point to point shadows is to work with a cylindrical system — cartesian vectors are no longer the optimum tool. Fortunately, the condition $\mathbf{s} \cdot \mathbf{m} > 0$ can be rewritten in terms of gradients. For this case: as you step out along the surface, if the gradient of the line joining the current point to the starting point is greater than the maximum gradient so far, then the point is illuminated. The gradient concept can easily be extended into the two-dimensional case, as no specification of direction has been made.

The final problem of determining which order to process the points on the surface

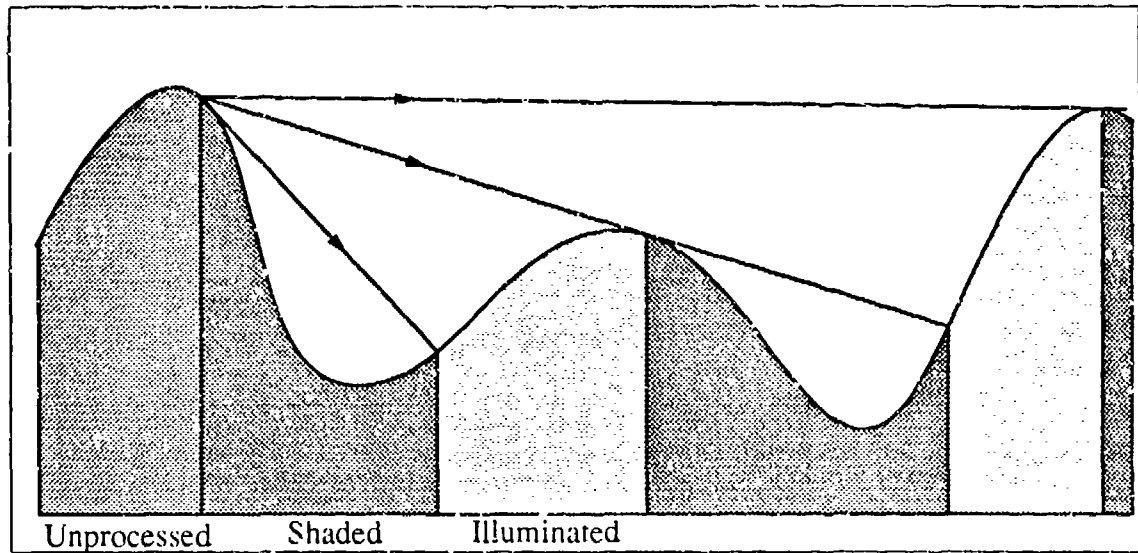


Figure 5.11: Shaded regions of a one-dimensional surface due to point to point scattering.

is still not simple — the most computationally effective being to spiral out from the 'source' point and calculating, only once for each point, whether that point is shaded or not. The difficulty lies in working out which points lie along the line of sight between the current point and the source position. Here, the most sensible course of action is to precalculate the point to point dependencies; i.e., for each point, create a list of points which will be directly affected by a change in it. Figure 5.12 shows the concept schematically. These lists can be created in such a way as to form a template which can be overlayed on the surface at any position. The template must be twice the area of the surface; thus ensuring that the centre of the template can be positioned at one corner of the surface while the whole surface still remains under its influence, even though only one quarter of it is used. If the template were the same size as the surface, then only when the template is positioned above the surface centre would the whole surface be processed.

All that need be done now is to spiral out, at each point working out the gradient

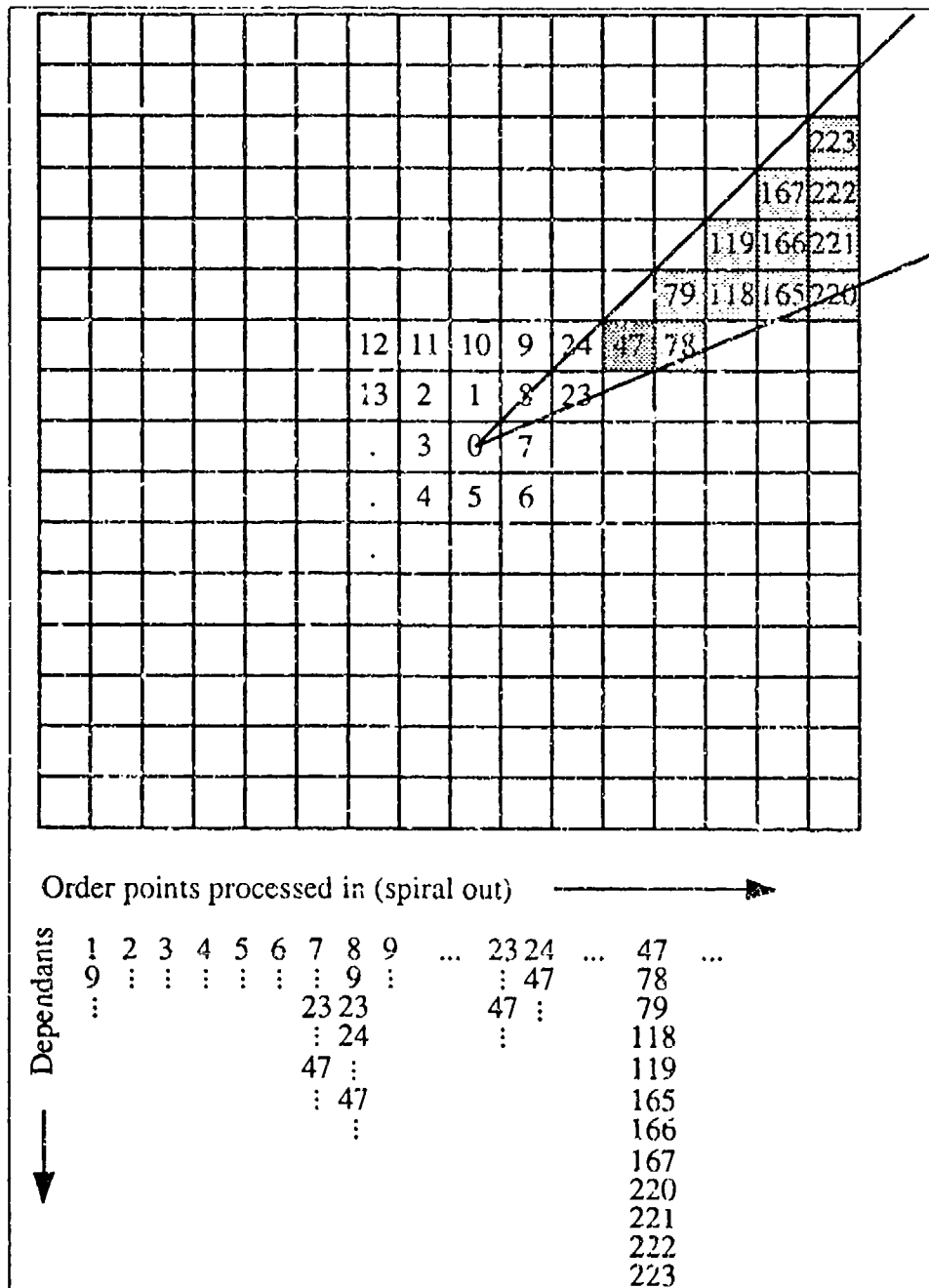


Figure 5.12: Creation of a template for determining point to point shadows on a two-dimensional surface. The dependencies are created by tracing a straight line between a point and the centre, inserting a reference to that point into the list of all points the line passes through. Point 47 has been added to the list of every point that has an effect on it; a completed list for point 47 is also shown.

of the slope from the centre to the current point. This is compared with the value

of the 'maximum' gradient associated with that point; if it is the new maximum the point is marked as illuminated, otherwise as shaded. The calculated gradient must still replace the maximum gradient of each point in the dependency list if it is greater, regardless of whether the original point was illuminated or not.

This last statement may seem unreasonable: how can a point which is not illuminated cast a shadow? The problem here is that each 'point' actually has a finite size — the whole defined as shaded or illuminated by the state of the centre of that point. It is possible though, that one corner of the point might be illuminated, the centre being shaded; this could cast a shadow, which if ignored, would propagate an error though to all dependencies. The question of whether the whole point should be set as shaded or illuminated is unresolved; a better model could give each point a more analogue value depending on the percentage of its area shaded. However, it should be noted that as the surface varies smoothly, only those points on a boundary between light and dark will not be totally one state or the other (a small percentage of the total number of points). This implies that for a point which is on the boundary, over half of its area will be of the same state as its centre. Finally, if the surface has been discretised to a sufficient degree, adjacent points will not have a noticeably different effect on the light which scatters from them, therefore some averaging of the shaded/illuminated state will occur.

The speed of this process can be improved by watching for when the gradient and distance from the initial position take the light above the surface — at this point, all dependents in the point's list can be marked as shaded.

Figure 5.13 shows a two-dimensional surface profile (left image) and the effect of the

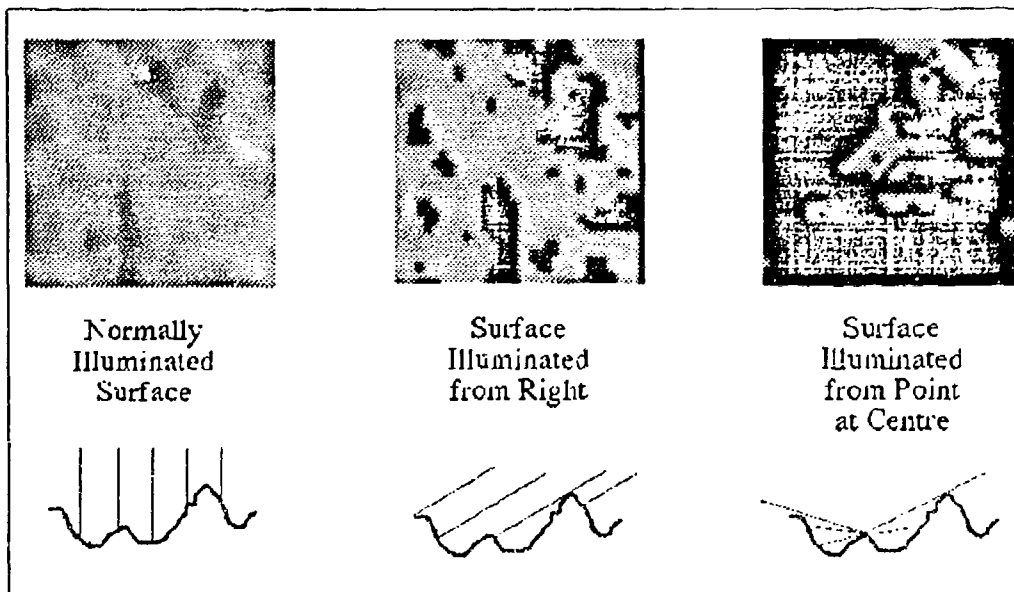


Figure 5.13: Representations of a computationally generated surface profile showing the results of the shading techniques. The surface height at a point is given by the brightness (light is high). The black regions indicate shaded areas.

two shading techniques, one of illumination from a certain angle (middle image), and the other of point to point shading (right image). The dark line down the right hand side of the middle image is present because the images actually represent point heights, but the shading calculations work on the connections between them; i.e. a surface with a side of 32 points will have 31 facets along it.

Extending the two-dimensional shadow calculations from a rectangular grid into one in which each rectangle is subdivided into two triangles is fairly simple. For the illumination and observation calculations, each 'row' of the surface can still be considered, except now a row has twice as many points. The point to point calculation requires slightly more thought, two templates are required, one for each of the two possible 'source' triangles. More care must also be taken when spiraling out — the same process outlined above can be used, but the order in which the sub-

triangles are processed must be intelligently defined: the one closer to the centre first.

The application of the methods described above is not limited to calculating shaded regions for numerical calculations. The author believes that these methods are the fastest possible for determining lines of sight, with potential use in various areas.

5.2.3 Numerical Random Surfaces

A numerical random surface with a standard height deviation of σ and correlation length τ can be created simply by convolving Gaussian white noise, of standard deviation σ , with a Gaussian correlation function, of $1/e$ half width τ . This is shown pictorially in figure 5.14. Computationally, the convolution is performed by a multiplication in Fourier space. Zero mean Gaussian white noise of standard deviation σ has (from Parseval's theorem) a Fourier transform which is also zero mean Gaussian white noise of standard deviation σ . The Fourier transform of the correlation function is obtained by applying a fast Fourier transform algorithm to an array containing a Gaussian envelope function with a $1/e$ half width of τ . This transform can be remembered and need only be calculated once for each execution of the program, no matter how many surfaces may need to be generated.

The actual process of creating a random surface consists of obtaining a random number from a Gaussianly distributed set^[47], multiplying this number by the relevant entry in the correlation transform array and storing it in a result array. After every element of the result array has been allocated, an inverse fast Fourier transform is performed upon it. The final result is an array of Gaussianly distributed

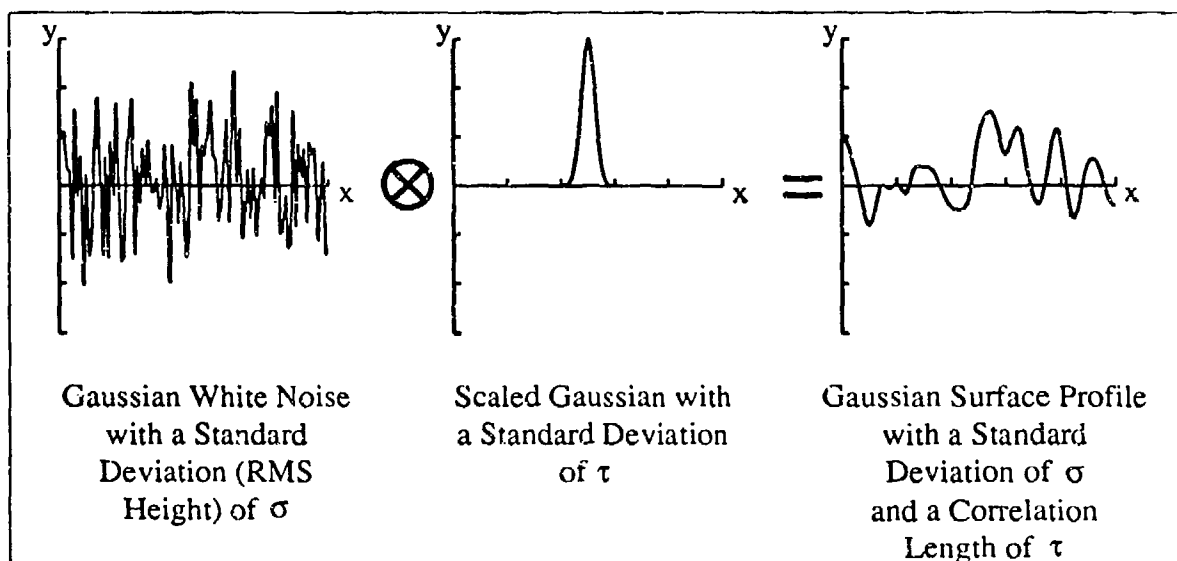


Figure 5.14: Convolution of Gaussian white noise with a Gaussian correlation function. The method is equally valid for two-dimensional surface creation.

numbers with a standard deviation σ and a Gaussian autocorrelation function with correlation length τ .

5.3 Results

5.3.1 Single Scatter Component of Simulation

Since the single scatter component and the analytical equation derived in the previous chapter both have a common origin, some degree of similarity between the two should be expected. Figure 5.15 shows the analytical and computational correlations obtained for the specular geometry with the reference at eight degrees. The simulation was run for a surface with parameters identical to those of surface #80, consisting of 2048 points and with a side length of 730λ . A square region with 24 points per side was illuminated (shading was incorporated) and the ensemble aver-

age consisted of 600 surfaces. The analytical curve was plotted using the expression for specular observation and with no averaging, equation (4.35) in chapter four.

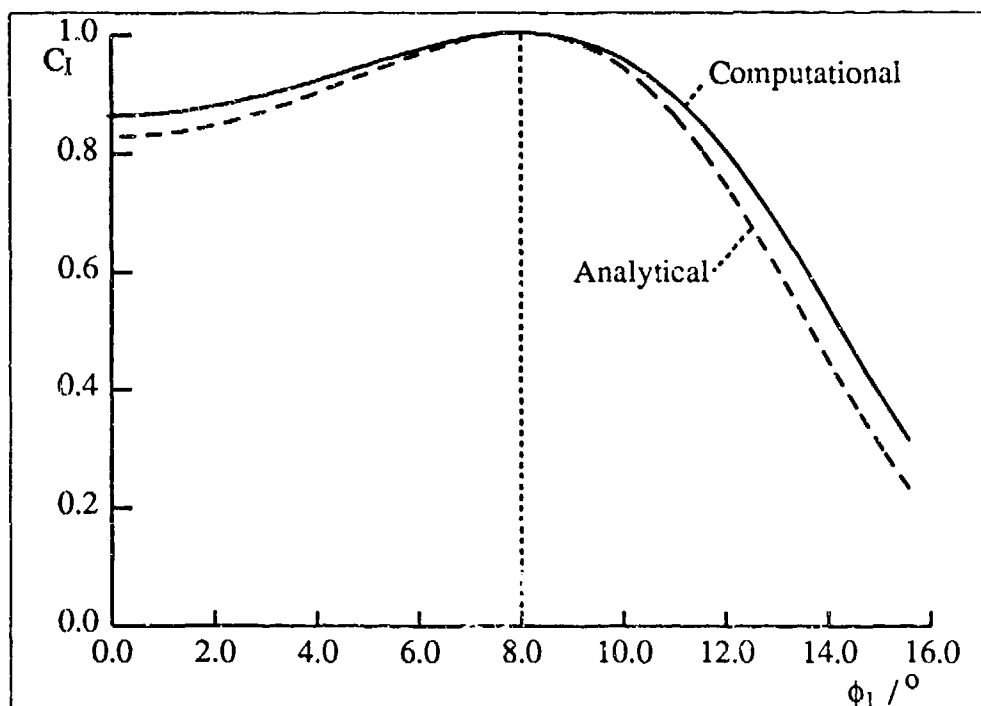


Figure 5.15: Analytical and single scatter computational intensity correlations for observation in the specular direction with the reference at 8 degrees. $\sigma = 2.27\mu m$, $\tau = 20.7\mu m$ and $\lambda = 0.633\mu m$. Both curves have data points every half degree.

The differences in the two curves may be attributed to two factors; the approximations made in the analytical derivation and the non-infinite, discretised surface in the simulation. The relatively small number of sampling points per surface might be expected to reduce the computational correlations, but as a reduction is not evident, the arguments presented previously in favour of large distances between surface points appear to be justified. However, although this appears unlikely, there may still be a netting off of two opposite effects, one increasing the correlation and one decreasing it, which could mask an error introduced by any particular approximation. Shadowing is not likely to have much effect for such a low sloped surface.

Figure 5.16 shows the effect of including polarisation tracking in the simulation, the curves show the correlations of the polarisation components. The s-polarised curve coincides with the calculation run with no polarisation tracking. In all cases the incident light was s-polarised, all simulation details are as above.

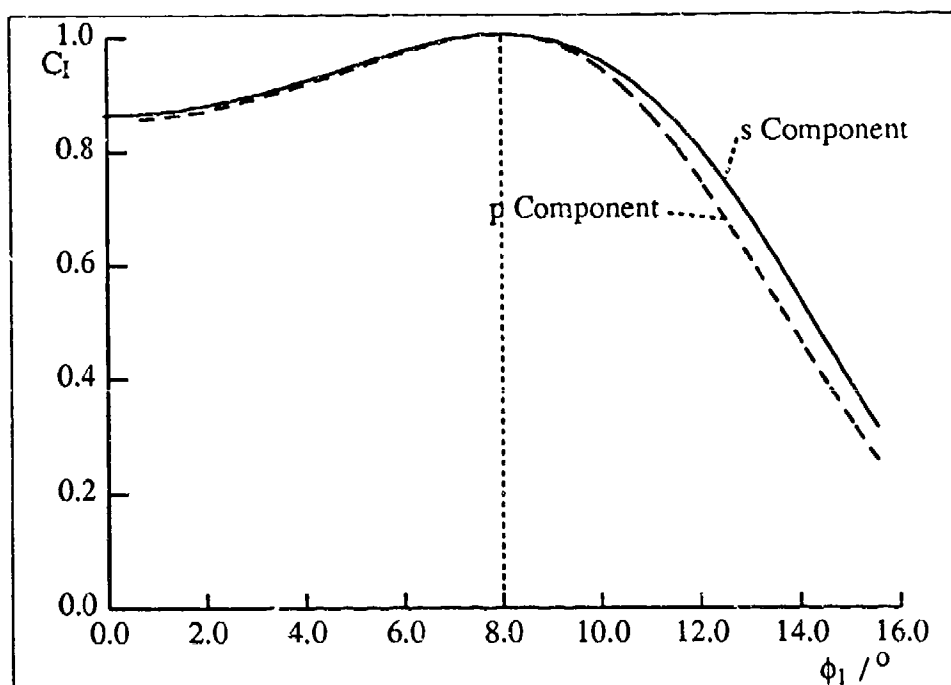


Figure 5.16: Single scatter intensity correlations with polarisation for observation in the specular direction with the reference at 8 degrees. The intensity of the p-polarised component was about 10^4 times smaller than the s-polarised one. $\sigma = 2.27\mu m$, $\tau = 20.7\mu m$ and $\lambda = 0.633\mu m$.

An interesting point to note here is that the simulation predicts a small amount of depolarisation in the specular direction. It is generally accepted that single scatter calculations do not predict depolarisation in this direction, and any cross polarised component noticed in experimental situations has been attributed to some degree of multiple scattering^[1].

The polarisation change shown here is an artifact of equation (4.10) and the method

chosen to control polarisation, the reflection coefficients. The cross-polarising reflection coefficient becomes zero for any specular scattering and on the face of things this will mean no depolarisation. However, when considering that a small amount of light may be scattered into the specular direction from slightly tilted surface facets, the last term of equation (4.10), not multiplied by the reflection coefficient, is non-zero, and makes a contribution to the cross-polarised light.

This result requires a more in depth study of polarisation changes from scattering elements. However, since the predicted depolarisation is very small (the cross-polarised component is about four orders of magnitude smaller than the co-polarised one), it will not be noticed by the experimental equipment, and may be ignored for the purposes of this work. It will make an insignificant contribution to any cross-polarised component due to multiple scattering. It may be that the result is merely an error, due to the specular approximation used to calculate the reflection coefficients or the finite size of the surface facets. Alternatively, it may be that the technique to control polarisation using reflection coefficients can not be applied to light which is not locally specularly reflected, or that the presumption that no depolarisation is present in the specular component of light scattered from a single scattering rough surface is invalid. Future work might like to consider this.

5.3.2 Experimental Results from a Multiply Scattering Surface

Figures 5.17, 5.18, 5.20 and 5.21 show, for incident-observed polarisation states of s-s, p-p, s-p and p-s respectively, experimental correlation results for surface #83. Within each figure, curves are plotted for reference angles of 2, 10, 20, 30, 40 and

50 degrees.

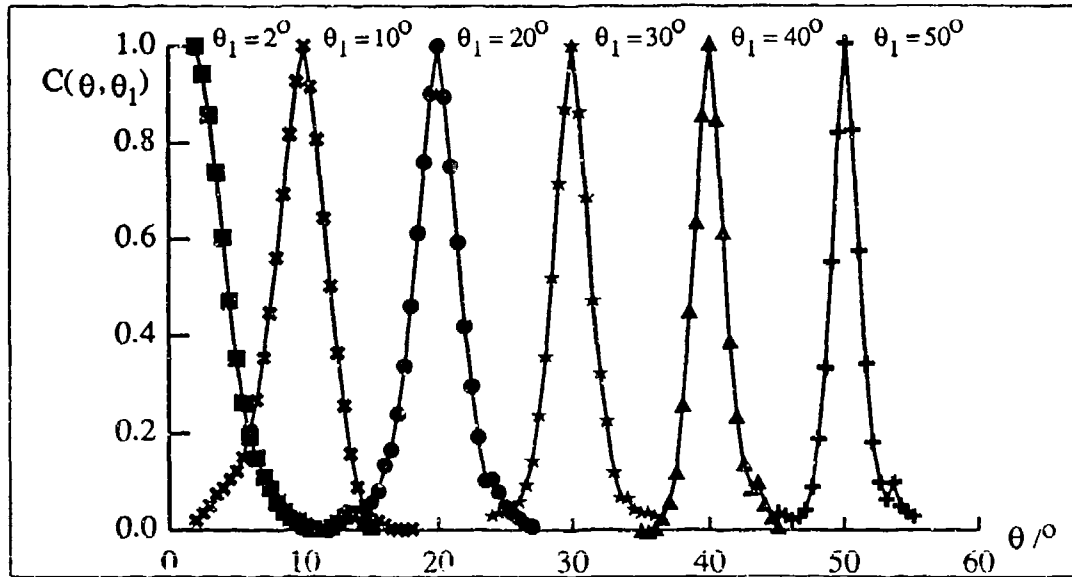


Figure 5.17: Experimental intensity correlations for surface #83 with incident and detected light s-polarised. Curve labels represent the (incident) angle at which the reference was taken. Observation is in the specular direction and $\lambda = 0.633\mu\text{m}$.

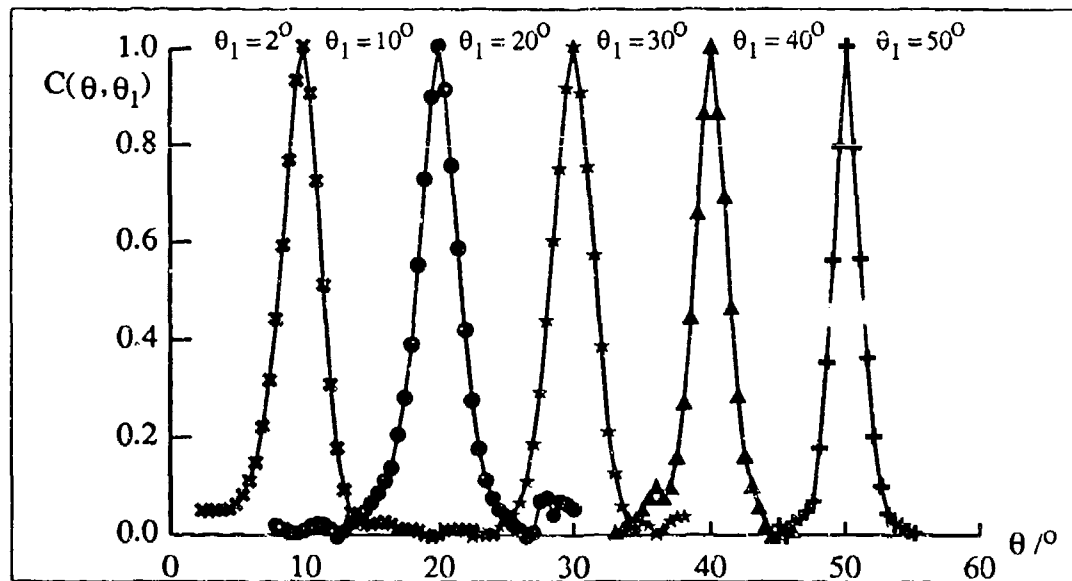


Figure 5.18: Experimental intensity correlations for surface #83 with incident and detected light p-polarised. Curve labels represent the (incident) angle at which the reference was taken. Observation is in the specular direction and $\lambda = 0.633\mu\text{m}$.

As can be seen in figure 5.17 and figure 5.18 — data from co-polarised arrangements — the narrowing of correlations at higher angles, or rather the widening at lower angles, observed in the single scattering case (cf. chapter four) is less evident. As expected then, this surface does not conform to the analytical theory in chapter four. Figure 5.19 emphasises the failure by showing the results of the analytical expression compared to the results in figure 5.17.

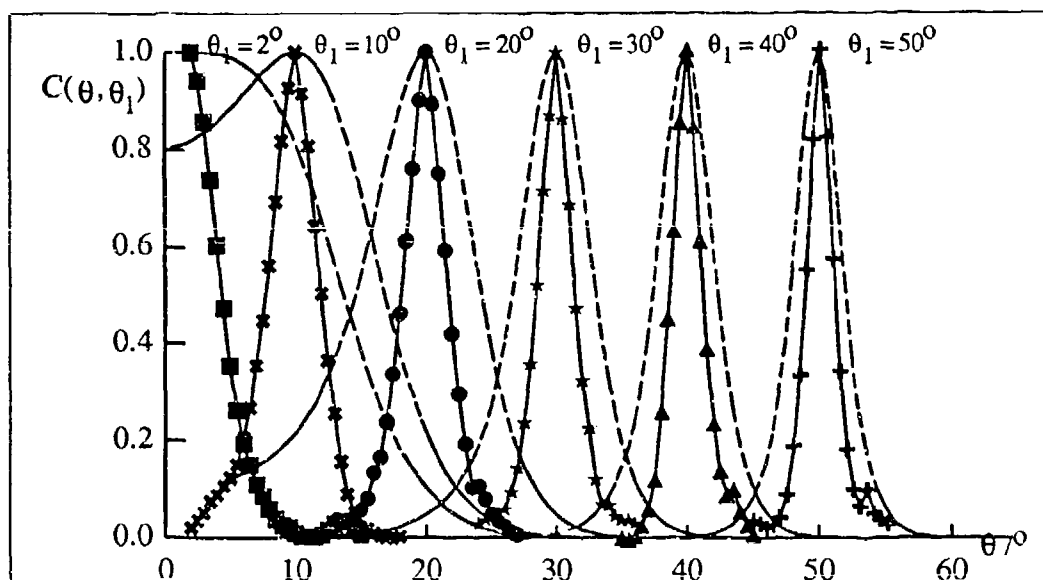


Figure 5.19: Experimental data as in figure 5.17 — surface #83, incident and detected light s-polarised — with averaged analytical curves (dashed lines) as described in chapter four overlayed.

Figure 5.20 and 5.21 are more interesting; these are plots in the cross-polarised case, showing the double scatter component of the scattered field. They are similar to the co-polarised graphs, figure 5.17 and figure 5.18, in as much as the widths of the peaks are the same and uniform, but at the lower angles an extra bump in the correlation coefficients has appeared at the sides. When considering that the experimental equipment correlates two separate speckle patterns (not just the point intensities, as do the calculations), this surprising result means the speckle produced

by one angular arrangement, in the double scattering case, is remarkably similar to that produced by another totally different arrangement. Chapter six discusses why this could be so.

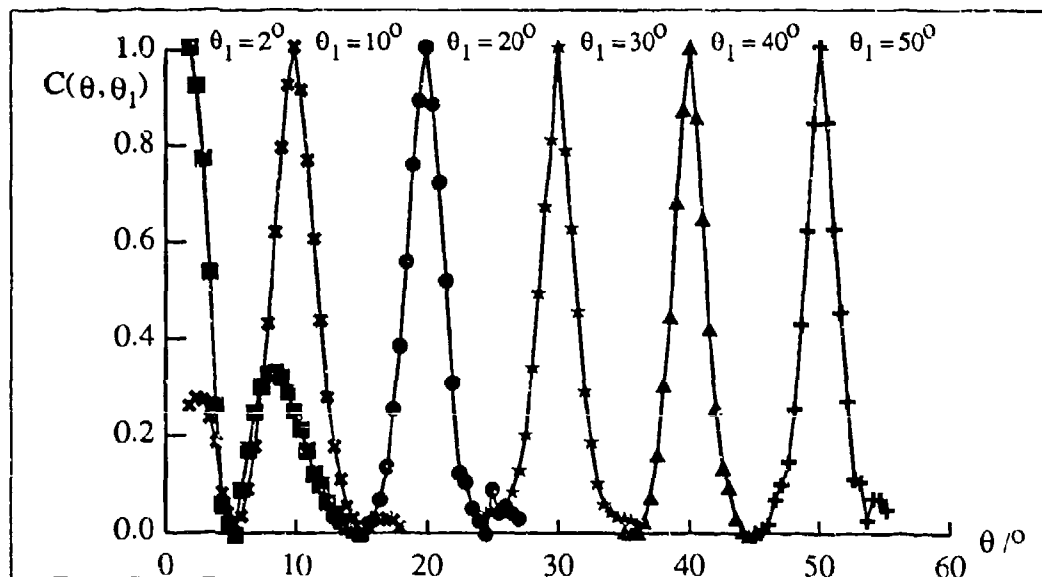


Figure 5.20: Experimental intensity correlations for surface #83 with incident light s-polarised and detected light p-polarised. Curve labels represent the (incident) angle at which the reference was taken. Observation is in the specular direction and $\lambda = 0.633\mu\text{m}$.

To show the extent of the double scatter extra correlation peak more clearly, a surface plot of the correlation coefficients is given, in figure 5.22, over all combinations of the two correlated angular arrangements, for surface #83, in the case where s-polarised light is incident and p-polarised light detected. Although a peak is evident either side of the main $\theta_1 = \theta_2$ ridge, this can be considered as simply a repetition of data — everything on one side of the ridge should be visible on the other. The peak of the extra correlation occurs when the reference image is at two degrees and correlated with one at eight and a half, or vice versa due to the symmetry. The data was taken with an eight bit Pulnix CCD camera which was used before the low noise Princeton

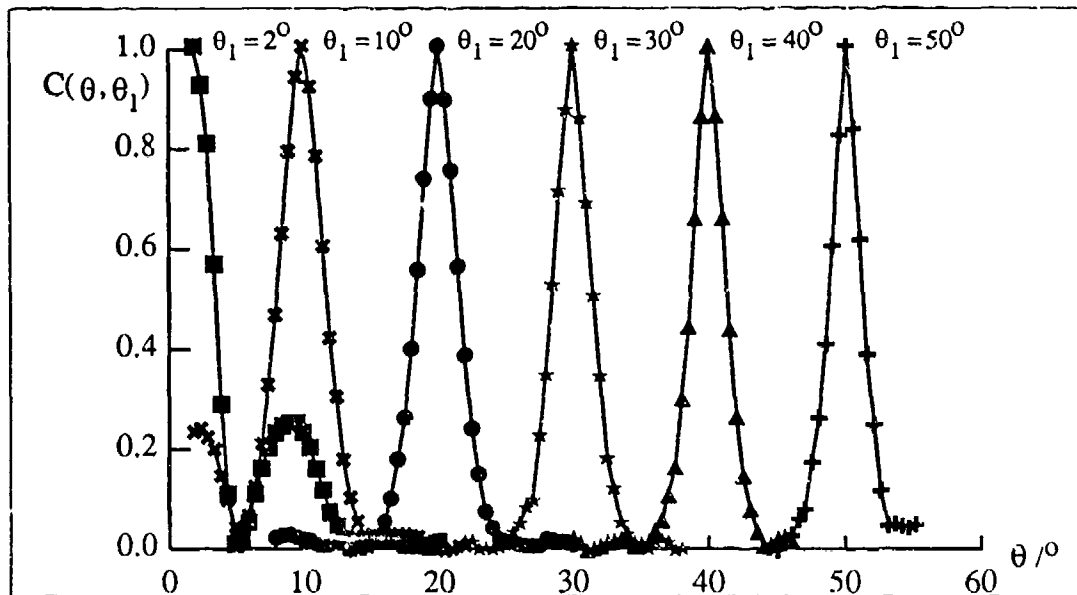


Figure 5.21: Experimental intensity correlations for surface #83 with incident light p-polarised and detected light s-polarised. Curve labels represent the (incident) angle at which the reference was taken. Observation is in the specular direction and $\lambda = 0.633\mu m$.

Instruments camera was available.

To help compare these results to the discussion of intensity results previously reported with this surface^[11], figure 5.23 shows the intensity plot for surface #83, where as usual, the detector is in the specular direction and the illuminating light has a wavelength of $0.633\mu m$. The figure shows two graphs for the average intensity, one with s-polarised light detected, the other p-polarised. Both curves were obtained with s-polarised light incident.

As with previous average intensity results presented, in the co-polarised situation, the light level detected tends to increase as the angle of incidence moves away from normal. The cross polarised case, however, shows some interesting behaviour; the intensity drops and then rises back up again before tailing off as with surface #239.

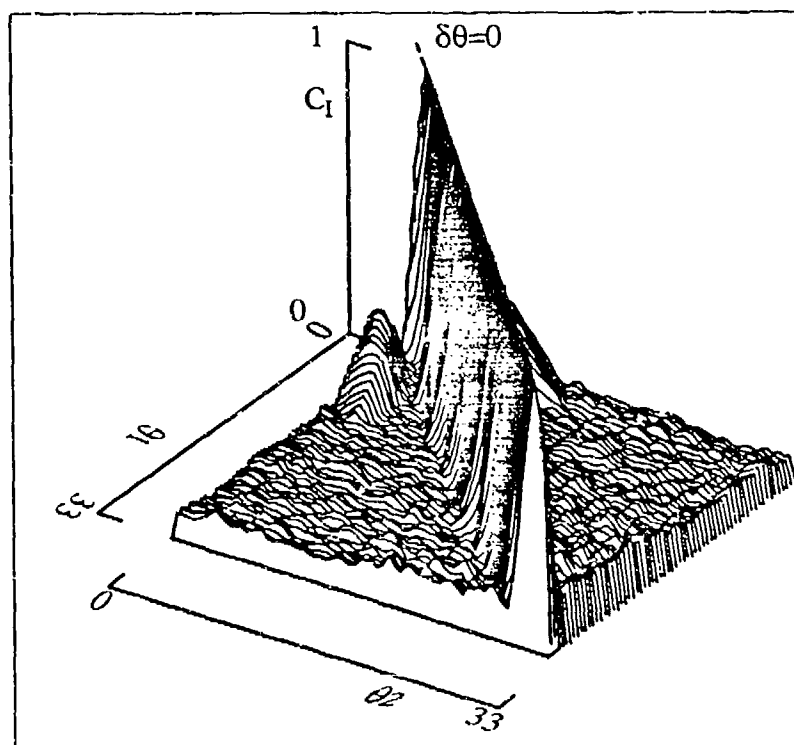


Figure 5.22: Surface plot of correlation coefficients for surface #83 with incident light s-polarised and observed speckle patterns p-polarised.

The rise in intensity is one of the 'side lobes' noticed by Mendez and O'Donnell^[11] when scattering from this surface, occurring here at a larger angle than they observed due to the geometrical arrangement used. No back-scatter peak is seen at normal incidence because the equipment was not set up to observe in that direction — the detector's view of the surface is obstructed by a mirror used in the beam delivery.

Figure 5.24 shows a close-up of the p-polarised component of figure 5.23. Two peaks are clearly evident in the intensity profile. The first peak is the side-lobe previously mentioned. The second peak, not observed in the work referenced above — most likely because of the geometrical arrangement used, is discussed in chapter six. It is shown to be a second order effect (where the back-scatter peak is zeroth order and

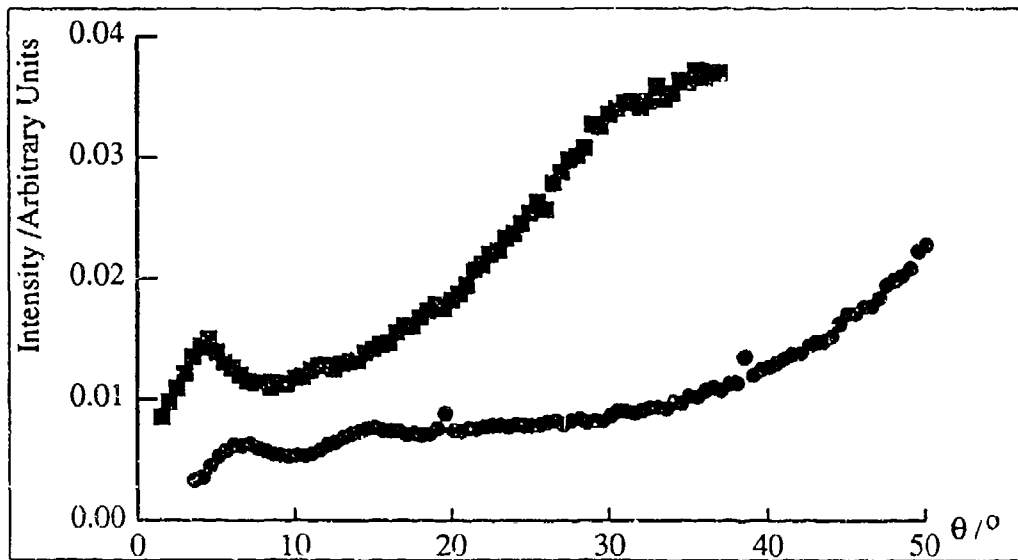


Figure 5.23: Average intensity plot for surface #83 with observation in the specular direction and with s-polarised (squares) and p-polarised light (circles) detected. The illuminating wavelength is $0.633\mu m$ and s-polarised.

the side-lobe first order).

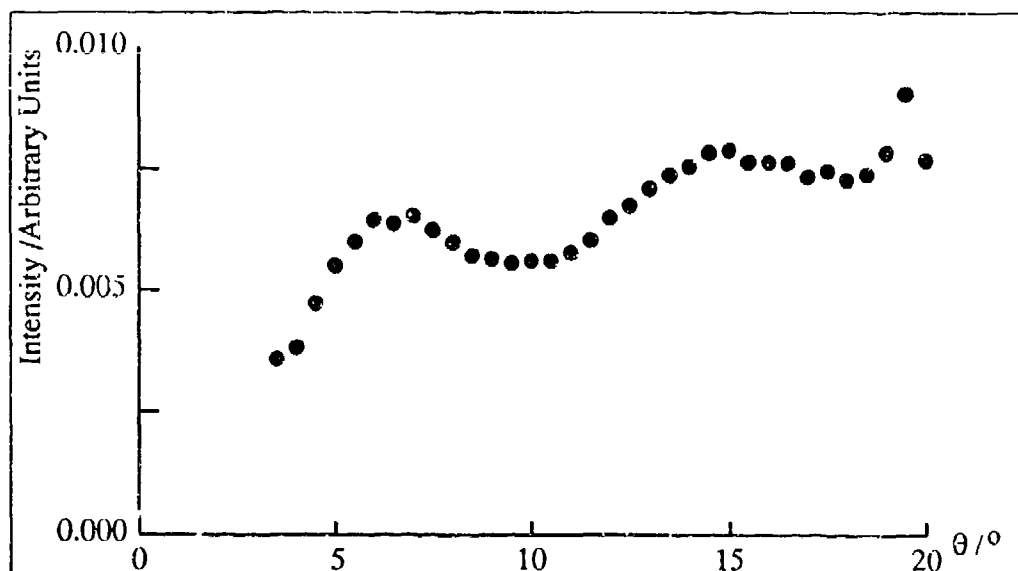


Figure 5.24: Average intensity plot for surface #83. This graph shows an expanded view of the p-polarised component of figure 5.23

5.3.3 Computational Results

Figure 5.25 shows the correlation curve produced by the computational method detailed above for a surface with rms height and correlation length as for surface #83. The graph shows the single and double scatter components for s-polarised and p-polarised light observed (with the incident field s-polarised), and also the combinations of the single and double components, the total curves, for each polarisation state.

As discussed in chapter four, there is no point trying to directly compare this result with an experimental one as the latter is spatially averaged, reducing the correlation values. A superficial examination reveals that the total computational values are, as expected, higher than the experimental ones at any given angle. It may be seen, however, that the distinctive bumps present in the experimental curves are noticeably lacking in figure 5.25.

Figure 5.26 is a curve produced by the method when an ensemble average is taken over only 100 surface realisations. As can be seen, extra correlation peaks are now present at the lower angles. The reason they are not observed in figure 5.25 is because they have been averaged out. This computational method gives extra correlation peaks of different heights and at different positions for each run of 100 frames. Averaging over greater numbers of frames washes the peaks out.

The inconsistent manner in which the extra peaks appear may be explained by the following points. A possible mechanism to describe the origin of the extra correlation peaks, given in chapter six, relies heavily on the phase change of the light scattered between sides of a well in the surface. The main approximations

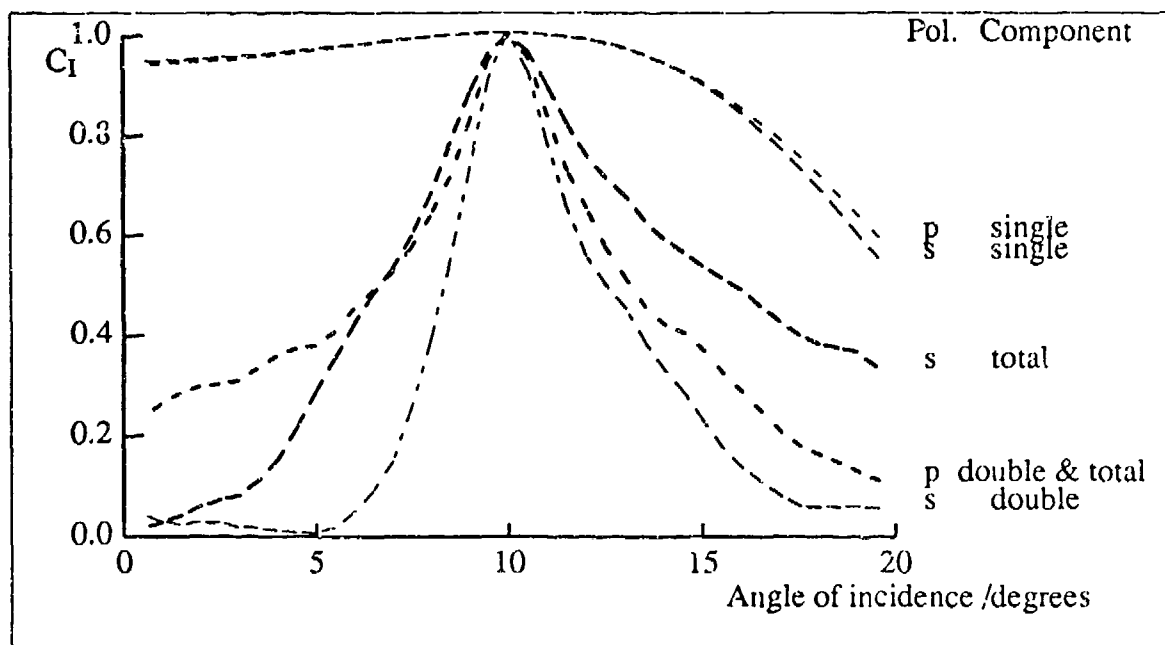


Figure 5.25: Computational correlation curves, for a surface with parameters identical to surface #83, with the reference image at 10 degrees and showing the different components. The incident field has a wavelength of $0.633\mu m$ and is s-polarised. The ensemble average was taken over 800 frames of a 2048 point surface with a side length of 60λ .

necessarily introduced into the computational method in order to get some results, namely the large spacing between surface points, will mean that this very critical distance (around seven wavelengths for surface #83) is constrained by the spacing and size of the surface facets. There are less than five surface facets over this critical distance. The random additions to the coordinates of the surface points to give a uniform phase distribution of the light scattered from *all* points of the surface will not help in this localised situation — the critical distance, over any five facets contributing to the extra correlation peak, being randomly adjusted.

Nevertheless, although it is not possible to compare figure 5.25 and figure 5.26 directly to the experimental results, they do show clearly which components of the

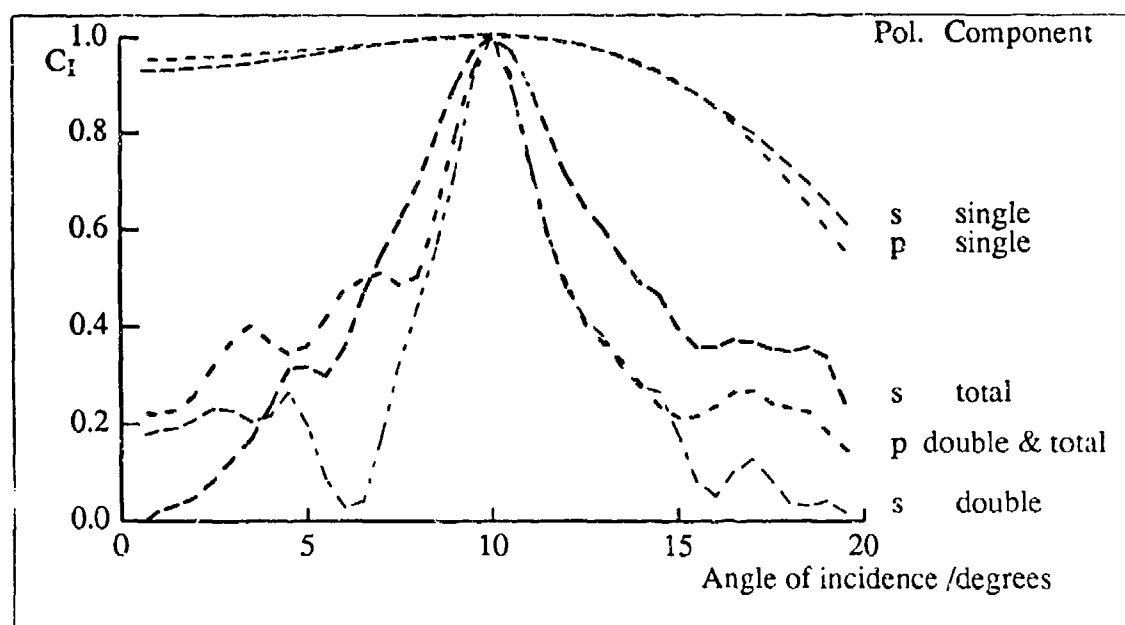


Figure 5.26: Computational correlation curves, the variable parameters are identical to that of figure 5.25 except that the ensemble average was taken over only 100 frames.

correlation curves are a result of the single scatter and double scatter processes. It is clearly evident that the double scatter process is responsible for introducing side peaks into the correlation curves. It may also be seen that the cross polarised, double scatter component of the simulation and the total curve are the same; proving that the cross-polarised, single scatter component (discussed above) has a negligible effect on the overall result.

Figure 5.27 and figure 5.28 show graphs of the correlation coefficients for, respectively, s-polarised and p-polarised components of the total (i.e., single plus double) field scattered from the computational statistical equivalent of surface #83 using the method above. All the results were taken over a 2048 point surface with a side length of 60 wavelengths and a wavelength of $0.633\mu m$. Each graph shows four curves, with the reference angles set at 10, 20, 30 and 40 degrees.

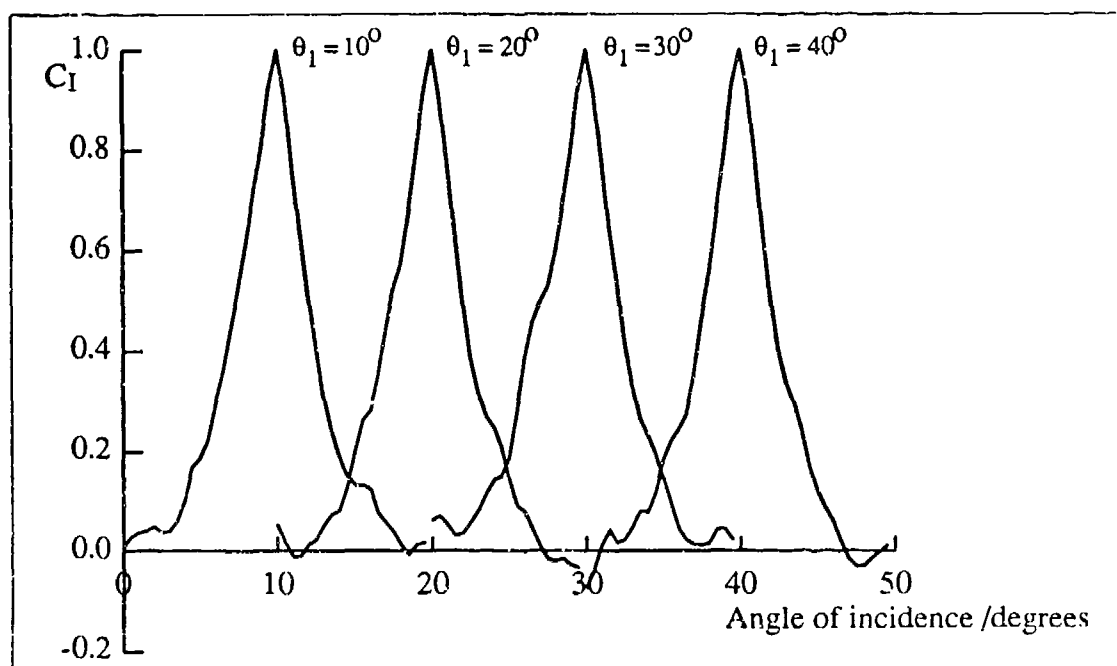


Figure 5.27: Total (single + double) computational correlation curves for surface #83 for various reference images (at 10, 20, 30 and 40 degrees). The incident field has a wavelength of $0.633\mu\text{m}$ and is s-polarised. The correlations consider only the s-polarised scattered component. The ensemble average was taken over 600 frames of a 2048 point surface with a side length of 60λ .

It is immediately noticeable that both of these figures show roughly the expected shapes for the correlation curves. The curves in each diagram are all about the same width irrespective of angle. The finding differs from the single scatter prediction that the widths of the peaks should reduce as the angle of incidence increases, but is in accordance with the experimental results (cf. figure 5.17 and figure 5.20).

The above results, derived from the computational model, go to show that the departure of the single scattering Beckmann theory from the experimental results arises solely because of its failure to cope with multiple scattering. In fact, it has been shown that consideration of just the single and double scatter components of the scattered field is sufficient to bring theoretical calculations into line with the

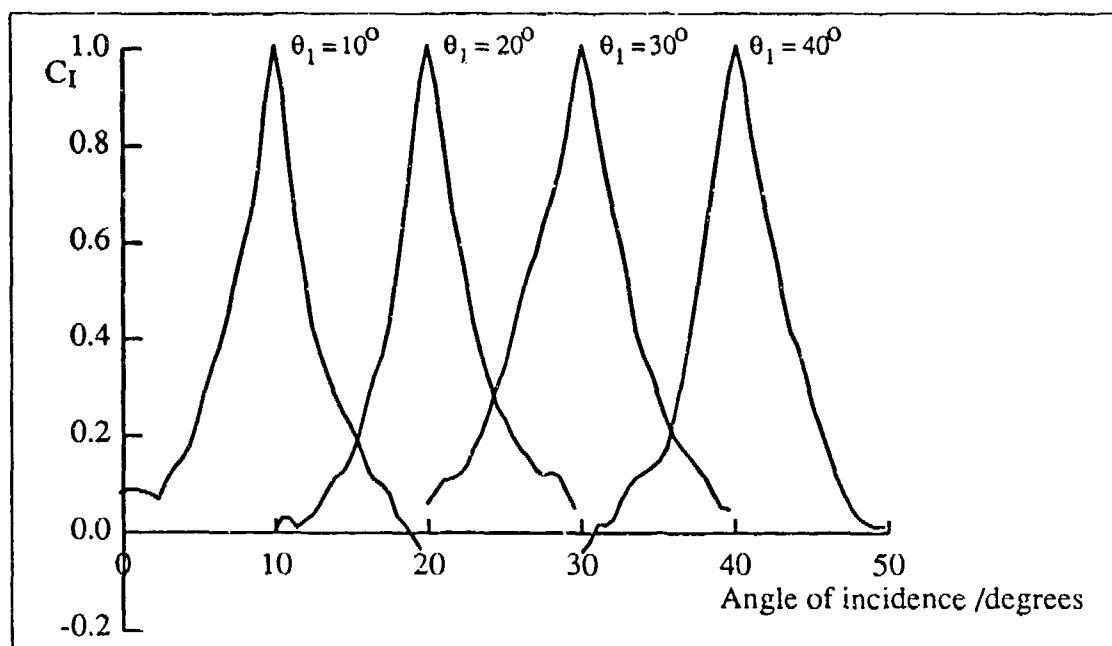


Figure 5.28: Total (single + double) computational correlation curves for surface #83 for various reference images (at 10, 20, 30 and 40 degrees). The incident field has a wavelength of $0.633\mu\text{m}$ and is s-polarised. The correlations consider only the p-polarised scattered component. The ensemble average was taken over 600 frames of a 2048 point surface with a side length of 60λ .

experimental results (from surface #83).

As shown in chapter four, surface #83 was expected to fall within the regime of the Kirchhoff approximation, but not to conform with the Beckmann solution. The similarity between experimental results and results from the computational model facing the same constraints shows that the conceptual basis of the statistical analysis of the surface parameters is trustworthy. An argument is presented in the next chapter which is based upon similar concepts and can explain the shapes of various scattering results from doubly scattering surfaces.

Chapter 6

Discussion and Conclusion

6.1 Single Scatter

It has been shown that for a Gaussian random rough surface with its rms surface height and correlation length within certain ranges, such that the surface may be considered to be single scattering, Beckmann theory adequately explains all experimental results presented once allowances for the particular experimental situation are incorporated. As an existing, well established theory copes well with the situation, no further explanation is deemed necessary here.

If any future work is proposed in this area, it should be to quantitatively examine the effect that spatially averaging the speckle around the observed direction has on the correlation coefficients.

6.2 Double Scatter

For Gaussian random rough surfaces with rms heights and correlation lengths such that they may be considered as double scattering, but still conforming to the restrictions on the Kirchhoff approximation, experimental results were found to depart from the Beckmann theory (which only considers a single scattering mechanism) to a greater degree as the surface parameters fall further from the ranges that indicate single scattering. Polarisation changes were also noticed which are not addressed by the Beckmann approach.

As there is no analytical theory known to the author which can account for multiple scattering from two dimensional surfaces, a computational model has had to provide the theoretical comparison for the results obtained. Vast demands on computer resources limited the extent of this comparison. However, a very simple model is now proposed which explains some features of the experimental results, namely the peaks in the correlation curves and their relation to the side lobe in the intensity plots.

The first part of this analysis will concentrate on an examination of the scattered intensity envelope.

6.2.1 Scattered Intensity Envelope Considerations

The following is based on an intuitive argument that some observable macro-effect (e.g., a side lobe) is simply related to micro-causes (e.g., phase differences due to a collection of individual scattering paths). This is not a new approach; various

authors (mentioned below) have explained the double scatter effect in this way, but only in a qualitative manner.

Consider figure 6.1, which shows one valley on a surface and one possible pair of interfering paths ace and dcb , both of which travel along the same line between the two points of contact with the surface. All incident light is at an angle θ with respect to the mean surface normal, and only the light scattered in the specular direction is considered. As vector quantities are used, the representation can be applied to two dimensional surfaces.

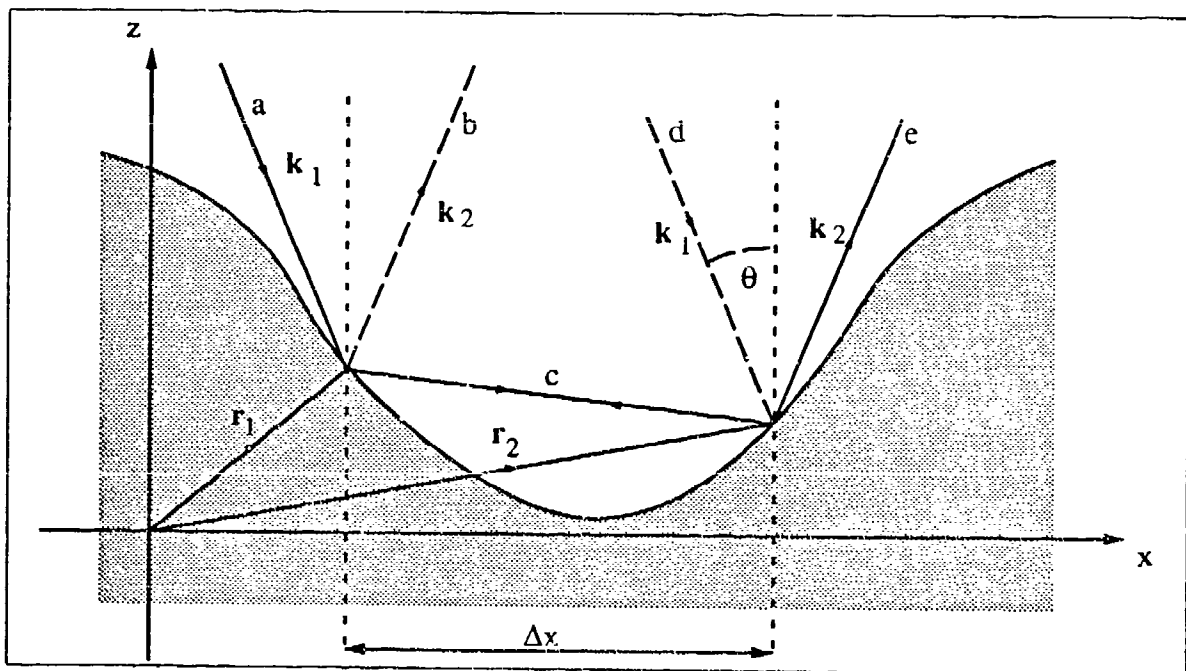


Figure 6.1: A pair of the many possible interfering paths within a valley of a rough surface.

Previous arguments along these lines^{[11][41]} have concluded by stating that the back-scatter peak observed when illuminating multiply scattering surfaces is due to constructive interference between two equal and opposite paths, one the time reversal of the other (a less general situation than with paths ace and dcb). These paths

are guaranteed to constructively interfere, all other paths resulting in no net interference. This argument may be extended to include the so called 'side lobes' by simply considering the first order interference fringe between more general paths^[34]. Figure 6.2 shows the equivalent of the side lobes evident when observation is in the specular direction.

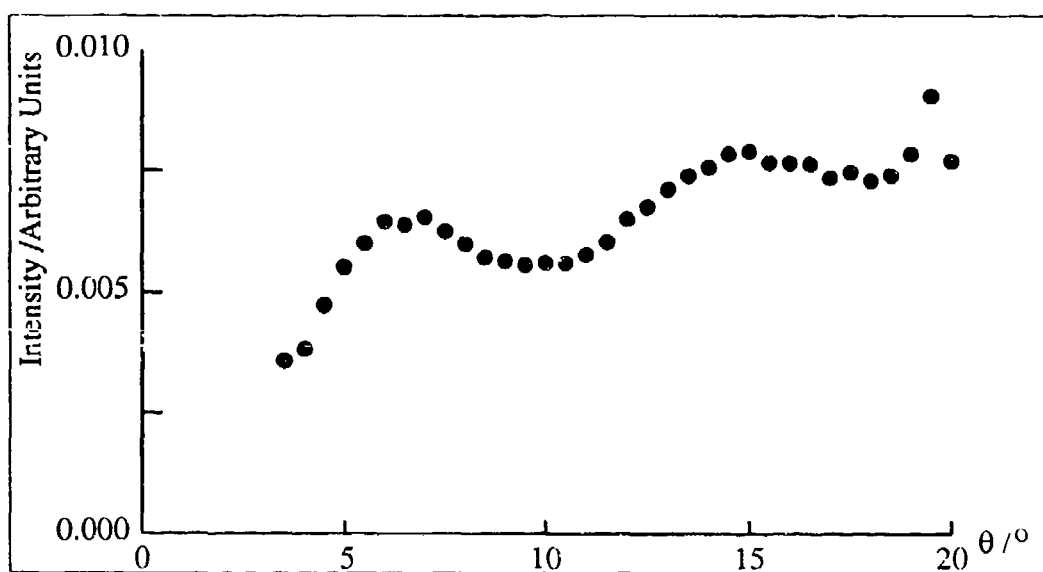


Figure 6.2: A graph showing the cross-polarised intensity scattering envelope from surface #83. This is a duplicate of figure 5.24 in chapter five. Observation is in the specular direction and the incident light has a wavelength of $0.633\mu m$.

Examining the arrangement more closely, the phase difference between the paths, ϕ , is easily determined:

$$\begin{aligned}
 \phi &= (k_1 \cdot r_1 - k_2 \cdot r_2) - (k_1 \cdot r_2 - k_2 \cdot r_1) \\
 &= (k_1 + k_2) \cdot (r_1 - r_2)
 \end{aligned} \tag{6.1}$$

For the specular case considered,

$$k_1 = \frac{2\pi}{\lambda}(\sin \theta x - \cos \theta z) \tag{6.2}$$

$$\mathbf{k}_2 = \frac{2\pi}{\lambda}(\sin \theta \mathbf{x} + \cos \theta \mathbf{z})$$

giving the phase difference

$$\phi = \frac{4\pi}{\lambda} \sin \theta \Delta x \quad (6.3)$$

where Δx is the distance between the two scattering points along the x axis. As no concessions to a one dimensional surface have been made, this is true even for a two dimensional surface — it is a consequence of the in-plane scattering geometry used.

For constructive interference, ϕ must be an integer number of 2π , i.e.,

$$2n\pi = \frac{4\pi}{\lambda} \sin \theta \Delta x \quad (6.4)$$

where n is an integer, or equivalently,

$$\sin \theta = \frac{n\lambda}{2\Delta x} \quad (6.5)$$

The question is now posed as to what Δx is in a macro sense. By averaging equation (6.5), over an ensemble of wells, the surface may be considered as a whole, such that

$$\sin \theta = \frac{n\lambda}{2\eta_{\Delta x}} \quad (6.6)$$

where the quantity $\eta_{\Delta x}$ has simply replaced Δx , and may be considered as the mean well width (across the direction of the incident plane).

Equation (6.6) can now qualitatively explain the features of figure 6.2. The backscatter peak is the zeroth order fringe $n = 0$, i.e., when $\theta = 0$; and subsequent peaks are the higher orders, $n = 1, 2, \dots$, their actual position determined by Δx .

When $\theta = 0$, $n = 0$ regardless of the fluctuations in Δx . This is the backscattering condition — all contributions are in phase. However, higher n values will

not preclude the variance of Δx . The prominence of any fringe at these values will depend upon the variance in the phase. The standard deviation in the phase may be determined from equation (6.3),

$$\sigma_\phi = \frac{4\pi}{\lambda} \sin \theta \sigma_{\Delta x} \quad (6.7)$$

The larger σ_ϕ is, the smaller the intensity of any higher order fringes. Obviously, to determine the exact condition the general form of the probability density function of Δx must be found. The values of $\eta_{\Delta x}$ and $\sigma_{\Delta x}$ may also then be obtainable.

Antibackscatter^[43] is also allowed by this model, since it has now been established that time reversed paths are not required for a peak in an intensity envelope.

One final feature of the intensity plots, which has not been previously addressed and which this model can explain, is why the co-polarised and cross-polarised components of the detected light show peaks at different angles. This is evident in figure 5.23 in chapter five, and also for the side lobes in other scattered intensity results from two dimensional surfaces^{[11][11]}.

Figure 6.3 shows intensity results similar to those shown in chapter five, but was obtained by summing up all of the pixels in a speckle image taken with a Pulnix CCD camera^[48]. This camera was used before the lower noise Princeton Instruments camera was available. The general shape of these curves should be ignored — they result from an automatic gain which the camera possessed — but the angles at which the peaks appear may be relied upon. The images which make up the cross polarised result include some of those which went to make up the surface plot in chapter five, figure 5.22.

Figure 6.3 is considered now as it is known to results from an area of surface #83

from which correlation results have been obtained and it clearly shows the positions of the peaks. It should be stressed that the following will still apply to figure 5.23 in chapter five.

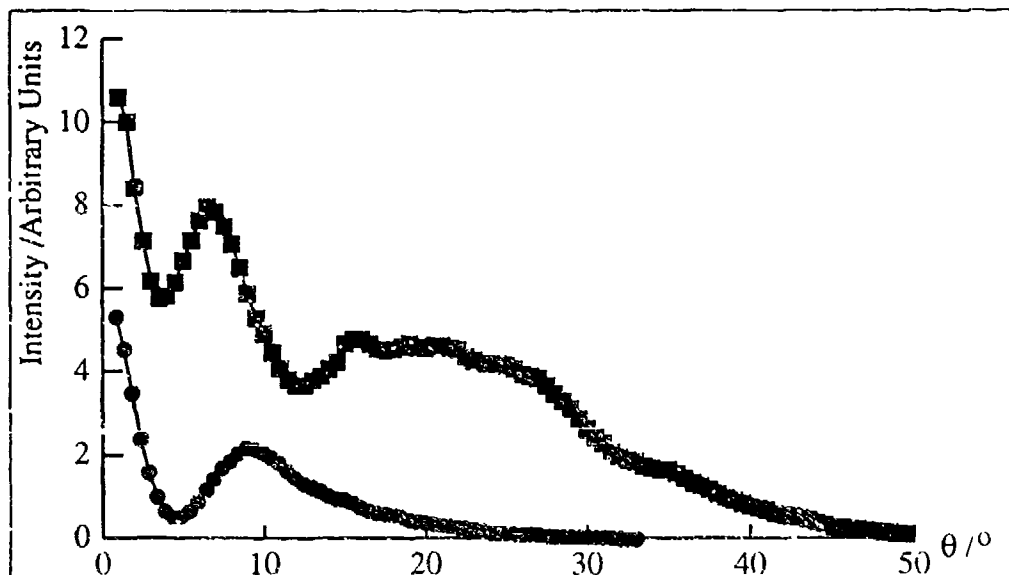


Figure 6.3: Intensity plots for s-polarised and p-polarised light detected from surface #83, showing the angles of the peaks observed for observation in the specular direction when s-polarised light is incident with wavelength $0.633\mu\text{m}$. Data points were taken every half degree.

It is now necessary to consider what is happening from a two dimensional point of view and introduce the concept of a mean well (i.e., the average dip in the surface). Consider one such well, which, upon double scattering, may give rise to both a co-polarised and cross-polarised component, as shown in figure 6.4. It is clearly evident in the diagram, that the mean well width from the point of view of the cross-polarised component is shorter than that for the co-polarised component, i.e., for s-polarised light incident,

$$\eta_{\Delta x}^p < \eta_{\Delta x}^s \quad (6.8)$$

where the superscripts represent the polarisation state of the observed scattered

light.

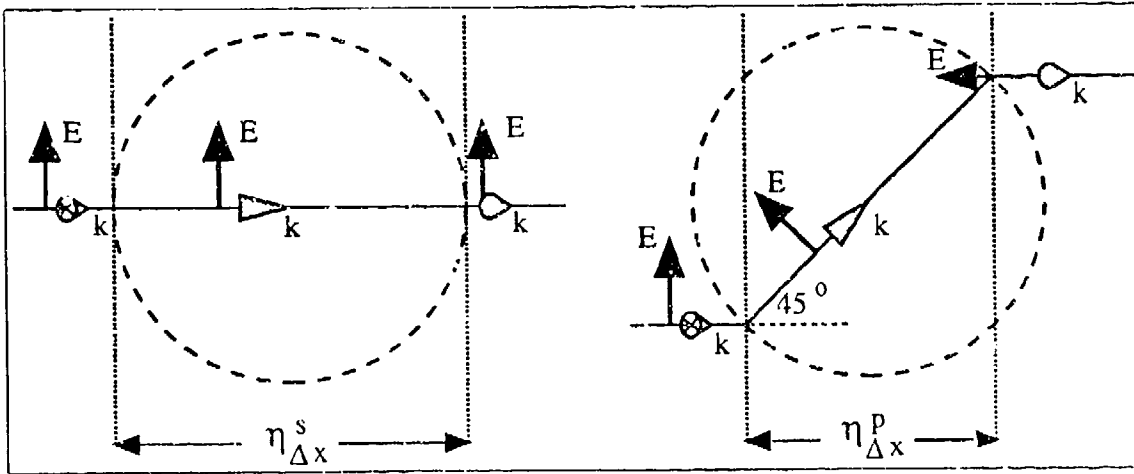


Figure 6.4: Schematic diagram showing how a well in a surface doubly scatters polarised light to give both a co-polarised and cross-polarised component.

Considering equation (6.6), it may be seen that for a particular n (greater than zero),

$$\theta_p > \theta_s \quad (6.9)$$

i.e., as observed, the angle at which a peak of a particular order appears, is larger for the cross-polarised component than for the co-polarised one.

Continuing with the model of a circular (the average shape) mean well, a more definite relationship between $\eta_{\Delta x}^p$ and $\eta_{\Delta x}^s$ may be established, purely due to the circular geometry. From figure 6.4,

$$\eta_{\Delta x}^p = \eta_{\Delta x}^s \cos 45 \quad (6.10)$$

This leads to a relation between the angles at which the peaks occur; for a particular n ,

$$\sin \theta_p = \sqrt{2} \sin \theta_s \quad (6.11)$$

Taking the angle at which the s-polarised side lobe appears in figure 6.3, $\theta_s = 6.5 \pm 0.25$ degrees, and applying equation (6.11), the angle the p-polarised side lobe should be evident is, $\theta_p = 9.2 \pm 0.4$ degrees. This compares well with the angle measured from figure 6.3 of 9.25 ± 0.25 , giving a great deal of weight to equation (6.11) and the simple mean well model.

6.2.2 Correlation Considerations

Following an argument similar to that given at the beginning of the previous section, a high degree of correlation may be said to exist when, on average, the difference in the phase differences between any two pairs of interfering paths is close to zero. Note that this is regardless of what those phase differences are. This is built on the basis that a high degree of correlation occurs when speckles appear in the same place, with respect to other speckles, that they do at another angle. The presumption is then made that individual wells in the surface must be making the same (or similar) contributions to the scattered field at both angles.

Although it may seem unlikely that the multiple contributions, from the various wells, should all maintain the same phase relationships with respect to each other, without keeping the same phase, there is no reason for imposing such a restriction and therefore the absolute phase change will be left undefined.

Starting with the phase difference between a pair of paths on the surface, equation (6.3), the difference between that introduced by one pair and that introduced by another may be obtained. In particular, the difference introduced by one angle of incidence compared to another may be determined.

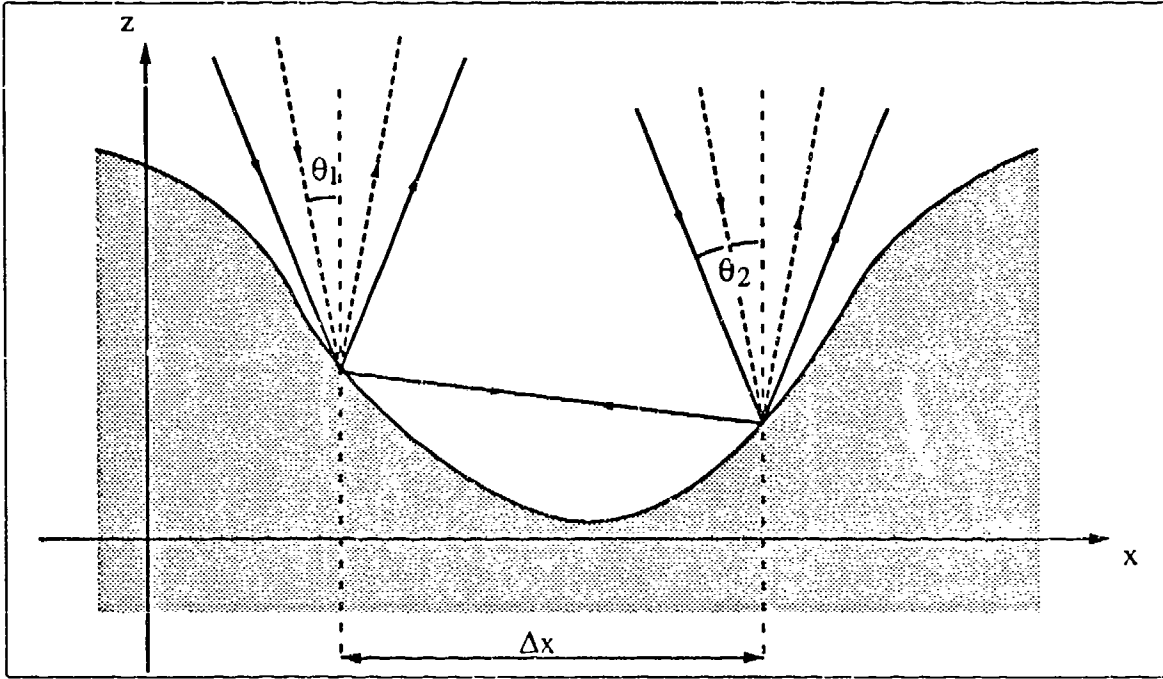


Figure 6.5: A pair of the many possible interfering paths within a valley of a rough surface shown at different angles of incidence.

Comparing figure 6.1 with figure 6.5, it may be seen that the latter consists of two of the interfering path pairs of the former, incident at different angles. For now, the path the light takes between scattering points on the surface is assumed the same for all angles for the purposes of comparison.

The phase differences within each pair are

$$\phi_1 = \frac{4\pi}{\lambda} \sin \theta_1 \Delta x \quad (6.12)$$

$$\phi_2 = \frac{4\pi}{\lambda} \sin \theta_2 \Delta x \quad (6.13)$$

where the subscripts 1 and 2 denote the two different pairs.

The difference in the phases between one angle of incidence and the other will

therefore be

$$\Delta\phi = \phi_2 - \phi_1 = \frac{4\pi}{\lambda}(\sin\theta_2 - \sin\theta_1)\Delta x \quad (6.14)$$

In equation (6.14) Δx may be replaced, following the same argument as made previously, by $\eta_{\Delta x}$ — a surface wide parameter.

As stated above, a high correlation will be expected when the difference in the two phases is zero or an integer multiple of 2π . Introducing this into equation (6.14) gives

$$\sin\theta_2 = \sin\theta_1 + \frac{n\lambda}{2\eta_{\Delta x}} \quad (6.15)$$

When $n = 0$, $\theta_1 = \theta_2$, a correlation between two of the same thing — obviously 1 — the main correlation peak in the experimental results in chapter five.

However, higher order interactions may still give a degree of correlation, albeit attenuated by the fluctuations in Δx , explaining the extra peaks observed in the correlation of speckle patterns from doubly scattering surfaces.

Unfortunately, experimental work conducted did not produce more than one extra correlation peak (the first order one), but the computational results, shown in figure 5.26 in chapter five, clearly show two extra peaks to the side of the main $n = 0$ peak. This evidence affords some confidence in the above argument.

6.2.3 Further Analysis of the Simple Model

The model, as it stands, is not perfect; for instance, it fails to predict the relative placement of any higher order intensity peaks and is likely to fail in the correlation

case as well. Given that the first order peak is at θ_1 , the second order peak should be expected, from equation (6.6), at

$$\sin \theta_2 = 2 \sin \theta_1 \quad (6.16)$$

In figure 6.3, with the first order peak at 6.5 ± 0.25 degrees for the co-polarised situation, the second order peak should be expected at 13.1 ± 0.5 degrees. There is clearly a dip around this region in the graph.

It is, however, possible to explain this failure. One of the main assumptions the model was based upon was that the mean well width is fixed, and that the interfering light traveled along equal but opposite paths between the two scattering points of surface.

It is now proposed that if light is incident on a well at a large angle, it will travel a different distance between points than that incident at a small angle. This can be seen in figure 6.6. Tracing the concept through, it is realised that if a larger angle of incidence decreases the width between scattering points, then the angle the peak appears at will correspondingly increase. Releasing the restriction of fixing $\eta_{\Delta x}$ explains why a second order peak is observed at around 15.5 degrees, in figure 6.3, instead of the predicted position of around 13 degrees.

The possible scattering paths that might exist higher up the well, traversing across larger distances, may be discounted by realising that, in a large proportion of these cases, the other side of the well is not likely to rise high enough to catch the light for the second scatter.

Note that now $\eta_{\Delta x}$ should be written either, $\eta_{\Delta x}(n)$, as a function of n , or more properly, $\eta_{\Delta x}(\theta)$, as a function of the angle of incidence. Some idea of the form of

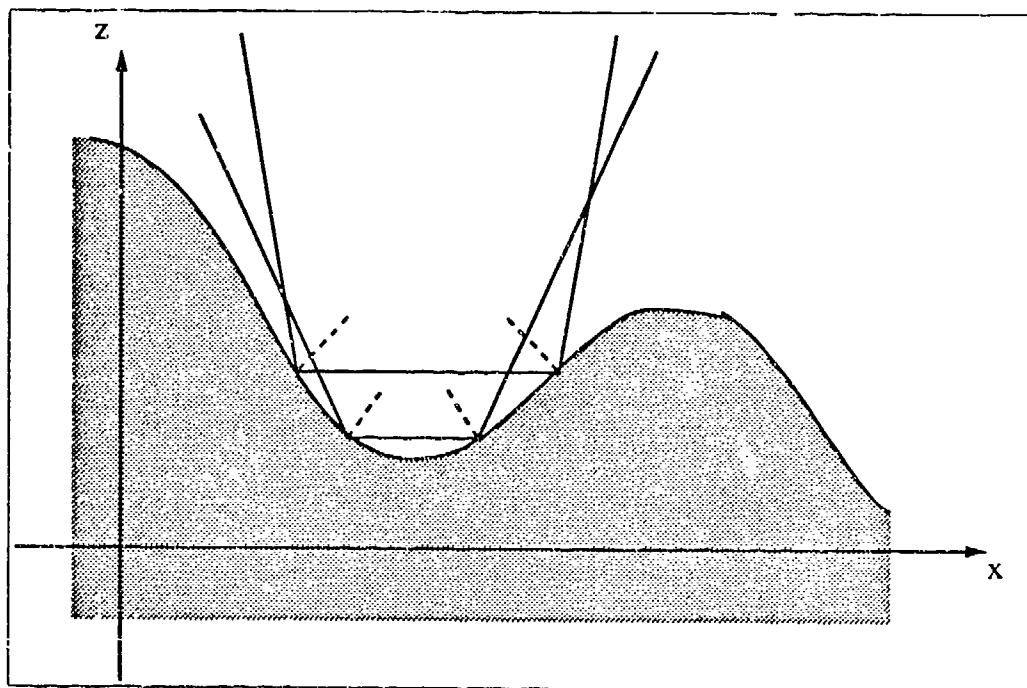


Figure 6.6: Diagram showing how an increase in the angle of incidence leads to a decrease in the distance traversed across the well.

this function may be gained by considering the gradients of the sides of a mean well.

It is first necessary to make an assumption that in double scattering, for scattering in the specular direction, the paths between scattering points are horizontal (by which it is meant that they are parallel to the mean surface plane). This may be justified by realising that if a mean well is being considered, this will be symmetrical and the light will therefore travel along a horizontal path. As discussed in chapter four, and shown in figure 4.3, this will lead to a gradient at the surface of

$$m = \tan \left(\frac{\pi}{2} - \frac{\theta}{2} \right) \quad (6.17)$$

where θ is constrained to be positive, and m is negative if θ is the angle of incidence, and positive if θ is the angle of observation (for incident light from the left in the above diagrams). The change in the gradient between the two scattering points is

therefore $2m$, the difference between $-m$ and m .

In chapter two, an expression was obtained for the rate of change of the gradient with respect to the distance across a Gaussian surface, namely its rms curvature, equation (2.33).

As the portion of the surface considered here is at the bottom of a well, i.e., in the region of a high point in the curvature, the approximation to the rms curvature may be on the low side. To allow for this a quantity ρ (which gives a result of less than 1) is introduced,

$$\frac{dm}{dx} = \frac{2\sqrt{3}\sigma}{\rho\tau^2} \quad (6.18)$$

σ and τ are, respectively, the rms height and correlation length of the surface. Strictly speaking, ρ will be a function of θ , decreasing as θ increases — for now it will be considered constant.

Dividing the change in the gradient by this rate of change will give an expression for, $\eta_{\Delta x}(\theta)$, the distance between the two scattering points,

$$\eta_{\Delta x}(\theta) = \frac{\rho\tau^2}{\sqrt{3}\sigma} \tan\left(\frac{\pi}{2} - \frac{\theta}{2}\right) \quad (6.19)$$

where θ is the angle of incidence. Obviously this expression will apply to the co-polarised case — it is related to the cross-polarised case by equation (6.10).

Substituting equation (6.19) into equation (6.6), an absolute expression for the angle, θ , at which the side lobes appear may be obtained,

$$\sin\theta \tan\left(\frac{\pi}{2} - \frac{\theta}{2}\right) = \frac{\sqrt{3}n\lambda\sigma}{2\rho\tau^2} \quad (6.20)$$

which may be transformed with suitable trigonometric identities to give (for terms

up to order $\tan^2(\theta/2)$),

$$\tan\left(\frac{\theta}{2}\right) \approx \frac{(2 - \zeta) - \sqrt{(2 - \zeta)^2 - 4\zeta(\zeta + 2)}}{2(\zeta + 2)} \quad (6.21)$$

where

$$\zeta = \frac{n\lambda\sqrt{3}\sigma}{2\rho\tau^2} \quad (6.22)$$

Applying this to surface #83, ρ may be determined by looking at the $n = 1$ peak in figure 6.3 where $\theta = 6.5 \pm 0.25$. It is found that $\rho = 0.66 \pm 0.14$ (the large error is due to the inclusion of the uncertainty in the measured surface parameters, σ and τ).

For $n = 2$, equation (6.20) predicts $\theta = 15 \pm 5$ degrees (which will be slightly on the low side due to the assumption that ρ is fixed). It may be seen that the second peak in figure 6.3 is near the centre of this range at 15.5 ± 0.25 degrees.

Incidentally, the mean well widths which give rise to these intensity peaks are approximately $4.3\mu\text{m}$ for $n = 1$ and $3.6\mu\text{m}$ for $n = 2$. That is just under 7 and 6 wavelengths respectively.

The calculated value of ρ for figure 6.2 is 0.94 ± 0.20 . The difference between this value and that found from figure 6.3 can be attributed to the different areas of the surface used in each case, which implies that the surface statistics are not uniform over the whole surface on such a small scale (and was found to be the case^[41]).

The relaxation of the constraint on $\eta_{\Delta x}$ also carries through to the correlation model. The assumption made at the start of this study, that the two scattering paths traverse the same line between identical scattering points, (refer back to figure 6.5

to see this), is no longer consistent with the understanding of the processes at this stage.

As previously mentioned, for a high degree of correlation, all that is required is for any two paths to give rise to the same phase change. It is not necessary for these paths to travel the same route.

Rewriting equation (6.14) to reflect this, one obtains

$$\Delta\phi = \phi_2 - \phi_1 = \frac{4\pi}{\lambda}(\sin\theta_2\Delta x_2 - \sin\theta_1\Delta x_1) \quad (6.23)$$

where Δx is not fixed, but depends upon the angle of incidence. The subscripts 1 and 2 denote the two different correlated arrangements.

Shifting again into using the mean width (which is now a function of angle) and confining the two phases to be integer numbers of 2π apart,

$$\sin\theta_2\eta_{\Delta x}(\theta_2) = \frac{2}{n\lambda} + \sin\theta_1\eta_{\Delta x}(\theta_1) \quad (6.24)$$

Substituting equation (6.19) (modified for the cross-polarised case) into this gives

$$\sin\theta_2 \tan\left(\frac{\pi}{2} - \frac{\theta_2}{2}\right) = \frac{\sqrt{6}n\lambda\sigma}{2\rho\tau^2} + \sin\theta_1 \tan\left(\frac{\pi}{2} - \frac{\theta_1}{2}\right) \quad (6.25)$$

which may be solved for θ_2 using equation (6.21), where

$$\zeta = \frac{\sqrt{6}n\lambda\sigma}{2\rho\tau^2} + \sin\theta_1 \tan\left(\frac{\pi}{2} - \frac{\theta_1}{2}\right) \quad (6.26)$$

Unfortunately, as discussed above, there is no reason to expect the phase differences in the correlation peaks to be related to the intensity envelope peaks. In fact, the paths which combine to give a high degree of correlation (i.e., speckles in similar

positions) are unlikely to be the same paths which produce the high points in the intensity envelopes. However, the differences introduced into the paths by illuminating at different angles are adequately covered by equation (6.25) if ρ is set to allow for the curvatures involved.

Examining figure 5.20, it may be seen that for the reference, θ_1 , at 2 degrees, a peak in the correlation curve appears when $\theta_2 = 8.5 \pm 0.25$ degrees. This gives a value for ρ in the correlation arrangement of 1.0 ± 0.3 (including all errors due to the uncertainty in measurement of the surface parameters). It has been assumed that the observed peak is the first order interference one, i.e., for $n = 1$.

With the reference at $\theta_1 = 10$ degrees, there is an observed peak at $n = -1$. Its predicted position, at $\theta_2 = 3 \pm 1.5$ degrees, compares favourably with the measured angle of 2.5 ± 0.25 degrees. However, note that the angular differences between the two peaks and their reference angles are too similar to pose a strenuous test for the theory. The fluctuations in Δx , coupled with the spatial averaging necessarily involved with the experimental technique used, prevent any higher order peaks, which could more rigorously test the predictions, from being observed in the correlation experiments.

It may be realised that the larger value of ρ for this situation, means that the curvature, averaged around the area of a well which contributes to a high degree of correlation, is less than that in the intensity case; i.e., the scattering processes which contribute to the correlation in surface #83 occur at higher positions in the well than do those which contribute to a side lobe in the intensity envelope.

As mentioned above, ρ was assumed to be constant. The assumption will have a

much larger effect on the correlation results, than it did in the intensity situation, as the curvature is likely to be varying more rapidly in the region of the surface contributing in the former case. This statement is based on the previous finding, that the portion of the surface contributing to the peaks, is further away from the bottom of a well for the correlation case as compared to the intensity case. As this is not allowed for, the predictions of the positions of any correlation peaks should not be expected to match exactly with the observed positions.

Further evidence of the change in ρ with the angle of incidence is seen in the correlation coefficients for scattering from surface #239. Considering figure 4.20, values for ρ are found to be about 0.6 around the 10 degree point, increasing to about 2.0 by the 30 degree mark. These movements may be explained if at higher angles of incidence, the areas of a particular well contributing to extra correlation peaks are higher up the sides of that well; i.e., the average curvature between the two points is reduced. The movement of the contributing paths to higher positions in the well also explains why the extra correlation peaks are lower at the higher angles -- the fluctuations in Δx will be greater at higher angles.

6.3 Concluding Remarks

The first three chapters of this thesis were concerned with building up the background and the concept of multiple scattering and correlation coefficients. An introduction was given into the statistical notions and electromagnetic theories used later in the work; and the methods and controls required to produce results presented in the following chapters were detailed.

Perhaps the only real surprise contained within these three chapters was at the end of chapter two, where a statistical study gave an analytical tool for determining whether a Gaussian random rough surface falls within the regime of the Kirchhoff approximation. A distinction was made between the validity of the Kirchhoff approximation, as applicable to a point on the surface, and the single scattering Beckmann theory. The three surfaces used throughout the work were all seen to fall within the bounds of the Kirchhoff approximation (at least at normal incidence).

The fourth chapter saw the start of more original work; it examined the angular correlation of speckle patterns produced by low slope surfaces. A study similar to that used to determine which surfaces fall within the Kirchhoff approximation was employed, to give some idea of whether a surface should be expected, based on its measured parameters σ and τ , purely to be a single scattering one or not. It is shown that of the three surfaces under examination, one was purely single scattering, one double scattering, and the third lay on the border between the two regions.

An analytical expression was derived, following the work of Beckmann^[14] and Léger and Perrin^[31], for the intensity correlation coefficients expected in a general two dimensional scenario. It was then tailored to suit in plane scattering and some of its possibilities were explored, these departed from the results one might have expected intuitively. The more general expression was averaged around the direction of observation, to represent more accurately the relatively wide view considered in the experimental case. Experimental results from a single scattering surface were found to be in good agreement, and reexamining the possibilities explored earlier with this new averaged technique gave results in line with the intuitive understanding. Finally, results were presented for a surface which departs slightly from the single

scattering regime.

In chapter five, the double scatter Kirchhoff theory was derived for two dimensional scattering. It had to be solved computationally and most of this chapter was concerned with explaining the methods used to make it possible. Polarisation was incorporated into the calculations, and surface self shadowing was allowed for. A technique capable of calculating which points were visible from another, over the whole surface in just one pass, was presented. Experimental results and the results from the computational model were shown.

In the previous sections of this final chapter, an accepted model used to explain intensity and correlation results, which succeeded in predicting the occurrence of certain features, was shown to be insufficient at a less superficial level. The model was advanced and shown to adequately explain and predict various features evident in intensity and correlation situations, when observing in the specular direction, more accurately.

It was shown that the positioning of the wells within the surface does not matter, only their widths have any effect upon the angular positioning of multiple scattering features. Also, it was suggested that it was a region near the bottom of a well which gave rise to the intensity envelope side lobes, and that less restriction is placed upon the region giving rise to the extra correlations.

This may be explained by considering that for an overall intensity gain, i.e., a side lobe, a vast majority of the wells on a surface must be introducing similar phase changes (so that their contributions to the scattered field will constructively combine). It seems reasonable to expect that any similarities in the various wells on

the surface, will be towards their bottoms -- every well has a bottom, but how far up its sides go is less definite.

For a high degree of correlation, it is only required that a single well should give the same phase contribution to the scattered field at one angle as it did at the other angle being considered. It should be expected that this will occur surface wide (on an average basis) at particular angles only, but not necessarily at those angles which give rise to intensity side lobes.

The main successes of this model were the relationships formed between peaks of different orders in both the intensity envelope and correlation curves, and between the co- and cross-polarised peaks (of a particular order) observed in the intensity results.

No attempt was made to reformulate the equations derived, such that they may be applied in a more general situation than in the specular direction. However, the basic principles are not affected by the geometry; it should be a relatively simple matter to extend the model beyond the presented specular scenario.

As a final point, it would be desirable to have the model rebuilt on a more rigorous basis, using, say, the moments of Δx or even finding a function for it. It should then be possible to exactly predict the angular position of every feature in the correlation and intensity plots, and maybe even gain some idea of their relative contrasts.

Bibliography

- [1] J. A. Ogilvy. *Theory of Wave Scattering from Random Rough Surfaces*. Adam Hilger, 1991.
- [2] M. Nieto-Vesperinas and J. M. Soto-Crespo. Monte carlo simulations for scattering of electromagnetic waves from perfectly conductive random rough surfaces. *Optics Letters*, 12(12):979-981, December 1987.
- [3] J. M. Soto-Crespo and M. Nieto-Vesperinas. Electromagnetic scattering from very rough random surfaces and deep reflection gratings. *Journal of the Optical Society of America A*, 6(3):367-384, 1989.
- [4] A. A. Maradudin, E. R. Mendez, and T. Michel. Backscattering effects in the elastic scattering of p-polarized light from a large-amplitude random metallic grating. *Optics Letters*, 14(3):151-153, February 1989.
- [5] J. M. Soto-Crespo, M. Nieto-Vesperinas, and A. T. Friberg. Scattering from slightly rough random surface: a detailed study on the validity of the small perturbation method. *Journal of the Optical Society of America A*, 7(7):1185-1201, July 1990.

- [6] N. C. Bruce and J. C. Dainty. Multiple scattering from random rough surfaces using the Kirchhoff approximation. *Journal of Modern Optics*, 38(3):579-590, 1991.
- [7] N. C. Bruce and J. C. Dainty. Multiple scattering from random rough dielectric and metal surfaces using the Kirchhoff approximation. *Journal of Modern Optics*, 38(8):1471-1481, 1991.
- [8] N. C. Bruce, A. J. Sant, and J. C. Dainty. The Mueller matrix for rough surface scattering using the Kirchhoff approximation. *Optics Communications*, 88(4,5,6):585-596, April 1992.
- [9] J. S. Chen and A. Ishimaru. Numerical simulation of the second-order kirchhoff approximation from very rough surfaces and a study of backscattering enhancement. *Journal of the Acoustic Society of America*, 88:1846-1850, 1990.
- [10] A. Ishimaru and J. S. Chen. Scattering from very rough surfaces based on the modified second-order kirchhoff approximation with angular and propagation shadowing. *Journal of the Acoustic Society of America*, 88:1877-1883, 1990.
- [11] A. Ishimaru and J. S. Chen. Scattering from very rough metallic and dielectric surfaces: a theory based on the modified kirchhoff approach. *Waves in Random Media*, 1:21-34, 1991.
- [12] A. A. Maradudin, T. Michel, A. R. McGurn, and E. R. Mendez. Enhanced backscattering of light from a random grating. *Annals of Physics*, 203:255-307, 1990.

- [13] T. R. Michel, M. E. Knotts, and K. A. O'Donnell. Stokes' matrix of a one-dimensional perfectly conducting rough surface. *Journal of the Optical Society of America A*, 9(4):585-596, April 1992.
- [14] E. R. Mendez and K. A. O'Donnell. Observation of depolarization and backscattering enhancement in light scattering from gaussian random surfaces. *Optics Communications*, 61(2):91-95, January 1987.
- [15] K. A. O'Donnell and E. R. Mendez. Experimental study of scattering from characterized random surfaces. *Journal of the Optical Society of America A*, 4(7):1194-1205, July 1987.
- [16] P. E. Wolf and G. Maret. Weak localisation and coherent backscattering of photons in disordered media. *Physics Review Letters*, 55, 1985.
- [17] W. W. Montgomery and R. H. Kohl. Opposition-effect experimentation. *Optics Letters*, 5(12):546-548, December 1980.
- [18] P. F. Gray. A method of forming optical diffusers of simple, known statistical properties. *Optica Acta*, 4:2289-2294, 1978.
- [19] P. Beckmann and A. Spizzichino. *The Scattering of Electromagnetic Waves From Rough Surfaces*. Artech House, Inc., 1987.
- [20] M. J. Kim, E. R. Mendez, and K. A. O'Donnell. Scattering from gamma-distributed surfaces. *Journal of Modern Optics*, 34(8):1107-1119, 1987.
- [21] A. J. Sant, J. C. Dainty, and M.-J. Kim. Comparison of surface scattering between identical, randomly rough metal and dielectric diffusers. *Optics Letters*, 14(21):1183-1185, November 1989.

- [22] J. C. Dainty, M.-J. Kim, and A. J. Sant. Measurement of angular scattering by randomly rough metal and dielectric surfaces. In M. Nieto-Vesperinas and J. C. Dainty, editors, *Scattering in Volumes and Surfaces*. Elsevier Science Publishers B. V. (North Holland), 1990.
- [23] M.-J. Kim, J. C. Dainty, A. T. Friberg, and A. J. Sant. Experimental study of enhanced backscattering from one- and two-dimensional random rough surfaces. *Journal of the Optical Society of America A*, 7(4):569-577, April 1990.
- [24] K. A. O'Donnell and M. E. Knotts. Polarisation dependence of scattering from one-dimensional rough surfaces. *Journal of the Optical Society of America A*, 8:1126-1131, 1991.
- [25] J. C. Dainty, N. C. Bruce, and A. J. Sant. Measurements of light scattering by a characterized random rough surface. *Waves in Random Media*, 3:S29-S39, 1991.
- [26] A. A. Maradudin, J. Q. Lu, T. Michel, Z.-H. Gu, J. C. Dainty, A. J. Sant, E. R. Mendez, and M. Nieto-Vesperinas. Enhanced backscattering and transmission of light from random random surfaces on semi-infinite substrates and thin films. *Waves in Random Media*, 1:S129-S141, 1991.
- [27] M. Nieto-Vesperinas, J. A. Sanchez-Gil, A. J. Sant, and J. C. Dainty. Light transmission from a randomly rough dielectric diffuser: Theoretical and experimental results. *Optics Letters*, 15:1261-1263, 1990.
- [28] T. Asakura and N. Takai, editors. *Properties and Applications of Speckle*. 1986.
- [29] J. Ohtsubo, H. Fujii, and T. Asakura. Surface roughness measurement by using speckle pattern. *Japan. J. appl. Phys.*, 14:Suppl. 14-1, 1975.

- [30] H. Fujii, T. Asakura, and Y. Shindo. Measurements of surface roughness properties by means of laser speckle techniques. *Optics Communications*, 16, 1976.
- [31] H. M. Pedersen. Second-order statistics of light diffracted from gaussian, rough surfaces with applications to the roughness dependence of speckles. *Optica Acta*, 22(6):523-535, 1975.
- [32] H. M. Pedersen. On the contrast of polychromatic speckle patterns and its dependence on surface roughness. *Optica Acta*, 22(1):15-24, 1975.
- [33] D. Léger, E. Mathieu, and J. C. Perrin. Optical surface roughness determination using speckle correlation technique. *Applied Optics*, 14(4):872-877, April 1975.
- [34] D. Léger and J. C. Perrin. Real-time measurement of surface roughness by correlation of speckle patterns. *Journal of the Optical Society of America*, 66(11):1210-1217, November 1976.
- [35] M. Ohlídal. Comparison of the two-dimensional fraunhofer and the two-dimensional fresnel approximations in the analysis of surface roughness by angle speckle correlation. *Journal of Modern Optics*, 38(11):2115-2135, 1991.
- [36] T. R. Michel and K. A. O'Donnell. Angular correlation functions of amplitudes scattered from a one-dimensional, perfectly conducting rough surface. *Journal of the Optical Society of America A*, 9(8):1374-1384, August 1992.
- [37] M. E. Knotts, T. R. Michel, and K. A. O'Donnell. Angular correlation functions of polarized intensities scattered from a one-dimensionally rough surface. *Journal of the Optical Society of America A*, 9(10):1822-1831, October 1992.

- [38] S. Feng, C. Kane, P. Lee, and A. Stone. Correlations and fluctuations of coherent wave transmission through disordered media. *Physics Review Letters*, 61(7):834-837, August 1988.
- [39] M. Nieto-Vesperinas and J. A. Sanchez-Gil. Intensity angular correlations of light multiply scattered from random rough surfaces. 1992.
- [40] A. Papoulis. *Probability, Random Variables, and Stochastic Processes*. McGraw-Hill, Inc., 1965.
- [41] J. Goodman. *Statistical Optics*. John Wiley & Sons, Inc., 1985.
- [42] M. Born and E. Wolf. *Principles of Optics*. Pergamon Press Ltd., 1980.
- [43] J. Goodman. Statistical properties of laser speckle patterns. In J. C. Dainty, editor, *Topics in Applied Physics, Volume 9: Laser Speckle and Related Phenomena*, chapter 2. Springer-Verlag, 1984.
- [44] M.-J. Kim. *Light Scattering from Characterised Random Rough Surfaces*. PhD thesis, Applied Optics Group, Blackett Laboratory, Imperial College, 1989.
- [45] *Handbook of Optical Constants of Solids*. Academic Press, 1985.
- [46] A. Sant. *Enhanced Backscattering of Light from Randomly Rough Diffusers*. PhD thesis, Applied Optics Group, Blackett Laboratory, Imperial College, 1991.
- [47] E. L. Church and P. Z. Takacs. Effects of non-vanishing tip size in mechanical profile measurements. *Surface Topography*, 1991.
- [48] J. C. Dainty. The statistics of speckle patterns. In E. Wolf, editor, *Progress in Optics*, volume 14. Elsevier Science Publishers (North Holland), 1976.

- [49] K. M. Mitzner. Change in polarization on reflection from a tilted plane. *Radio Science*, 1(1):27-29, 1965.
- [50] W. H. Press, B. P. Flannery, S. A. Teukolsky, and W. T. Vetterling. *Numerical Recipes in C*. Cambridge University Press, 1986.
- [51] R. W. Syrratt. First year progress report. April 1991.